Eradication of Multidrug-Resistant Bacteria using Biomolecule-encapsulated Two-dimensional Materials

by

Abhishek Debnath

A Dissertation Presented in Partial Fulfillment
of the Requirements for the Degree
Doctor of Philosophy

Approved May 2019 by the
Graduate Supervisory Committee:

Alexander A Green, Chair
Nicholas Stephanopoulos
Yan Liu

ARIZONA STATE UNIVERSITY

August 2019

ABSTRACT

The increasing pervasiveness of infections caused by multidrug-resistant bacteria (MDR) is a major global health issue that has been further exacerbated by the dearth of antibiotics developed over the past 40 years. Drug-resistant bacteria have led to significant morbidity and mortality, and ever-increasing antibiotic resistance threatens to reverse many of the medical advances enabled by antibiotics over the last 40 years. The traditional strategy for combating these superbugs involves the development of new antibiotics. Yet, only two new classes of antibiotics have been introduced to the clinic over the past two decades, and both failed to combat broad spectrum gram-negative bacteria. This situation demands alternative strategies to combat drug-resistant superbugs. Herein, these dissertation reports the development of potent antibacterials based on biomolecule-encapsulated two-dimensional inorganic materials, which combat multidrug-resistant bacteria using alternative mechanisms of strong physical interactions with bacterial cell membrane. These systems successfully eliminate all members of the 'Superbugs' set of pathogenic bacteria, which are known for developing antibiotic resistance, providing an alternative to the limited 'one bug-one drug' approach that is conventionally used. Furthermore, these systems demonstrate a multimodal antibacterial killing mechanism that induces outer membrane destabilization, unregulated ion movement across the membranes, induction of oxidative stress, and finally apoptotic-like cell death. In addition, a peptide-encapsulation of the two-dimensional material successfully eliminated biofilms and persisters at micromolar concentrations. Overall,

these novel systems have great potential as next-generation antimicrobial agents for eradication of broad spectrum multidrug-resistant bacteria.

DEDICATION

I dedicate this thesis to my parents for their support and love

ACKNOWLEDGEMENTS

I would like to thank the following people:

- First and foremost, I would like to thank my advisor Dr. Alexander A. Green for all his valuable guidance, patience and support throughout my journey in graduate school. He always motivated me to explore new research ideas, which reformed me as a researcher.
- Our collaborator Dr. Qing Hua Wang for all her guidance and helpful discussions.
- My committee member, Dr. Yan Liu and Dr. Nicholas Stephanopoulos, for their time and invaluable advice.
- My oral committee member Dr. Ian Gould and Dr. Garry Moore for all their support and advice.
- David Lowry for all his help in TEM.
- All the member of Green and Wang lab with whom I had the pleasure of working, particularly Ahmed Yousaf, Duo Ma and Soma Chaudhary.
- And finally, all my friends who have been a constant support system throughout all these years of my graduate school.

TABLE OF CONTENTS

Page

CHAPTER Page

CHAPTER Page

LIST OF FIGURES

Figure Page

Figure Page

CHAPTER 1

Introduction and motivation

Two-dimensional transition metal dichalcogenides (TMDCs) are a class of layered materials, with each planer layer are made up of hexagonal MX_2 units and where M represents transition metal atom and X represents chalcogen.[1-5] Structurally, each transition-metal layer (M) is sandwiched between two layers of chalcogen atom (X). Based on the arrangement of metal and chalcogen atom, TMDCs exhibits structural polymorphism which includes 1H, 2H and 3R crystal phases. TMDCs also exhibit extraordinary mechanical, electrical and optical properties, which has led to implementation of these materials in a wide range of material-based applications in nanoelectronics, photonics, sensing, energy storage and opto-electronics[2,3,6]. Apart from electronic applications, the high surface area, absence of dangling bonds and high stability in liquid and air of the TMDCs, have inspired researchers to use them for a wide range of biological applications such as drug delivery, biosensing and antibacterial systems.[7-16]

The design of TMDC-based systems for biological applications involves careful engineering of 2D material surfaces using a wide range of biological molecules, which will enhance between the material and biological species, without imposing significant toxicity to mammalian cell. Until now, most of work in this regard focused on chemical based solution-phase processing, followed by covalent or non-covalent functionalization of TMDCs using biological relevant molecules.[17,18] Chemical treatment-based solution-phase processing usually involves treatment of TMDCs with strong reducing intercalating agents such as n-BuLi, followed by ultrasonication in the presence of biomolecules,

which leads to generation of biological molecules functionalized nanosheets. Despite successes in the development of TMDC systems for biological applications, the harsh treatment and presence of highly toxic lithium ion, hinders its implementation for clinical applications. To overcome these problems, researchers have developed alternative ultrasonication-based solution-phase processing of TMDCs. In this approach, TMDCs are generally ultrasonicated in the presence of aqueous amphiphilic molecule to produce biologically molecule encapsulated TMDCs. In these techniques, the amphiphilic molecule undergoes intercalation within TMDCs interlayer, leading to weakening of interlayer forces, followed by ultrasonication in aqueous solution. The ultrasonication creates chaotic shear forces, which in turn lead to the weakening of interlayer force and exfoliation of TMDCs. Furthermore, amphiphilic molecules undergo hydrophobic interactions with TMDC surfaces and stabilize the nanosheets using electrostatic and steric repulsion. Although there are some reports on dispersing TMDCs in biological active molecules, such as BSA[19], double stranded DNA[20], there are still few reports on dispersing TMDCs using biological molecules such as peptides, single stranded DNA, proteins and aptamers[21].

In this thesis, we report solution-phase processing of TMDCs in the presence of short synthetic single-stranded DNA (ssDNA). Unlike previous reports, which focused on solution-phase processing of TMDCs using naturally occurring long genomic double stranded DNA (2000 bp), herein we report dispersion of TMDCs in the presence short 20-nucleotide (nt) ssDNA. Also, we characterized the ssDNA-dispersed TMDCs using spectroscopic and microscopic techniques, which showed the pristine nature of ssDNA-dispersed TMDCs. Furthermore, we screened the affinity of different DNA sequences

toward the TMDC surface using experimental and computational methods. We studied the biocompatibility of these system against human carcinoma cell, *HeLa* cells. After successful determination of biocompatibility, we further demonstrated successful eradication of multidrug-resistant bacteria. After successful determination of antibacterial activity, we further evaluated the antibacterial mechanism of ssDNA-dispersed TMDCs.

In another work, we functionalized the TMDC surface with the cationic peptide poly-L-lysine and the amphiphilic block copolymer Pluronic F77. The highly positively charged poly-L-lysine enables the TMDC system to selectively target bacterial cell walls, while Pluronic-F77 stabilizes the system in high salt buffer conditions. This hybrid system showed strong electrostatic interactions towards multidrug-resistant bacteria and eliminates them through membrane damage. Furthermore, it showed an overall multimodal antibacterial action towards bacteria, overcoming the traditional problem of antibiotic targeting intracellular targets. The designed systems also successfully eradicated hard-to-eliminate biofilms and persisters. Finally, the designed system overcame the traditional problem of bacteria undergoing mutation and developing resistance, as demonstrated by extended exposure of bacterial cultures to the nanomaterial preparation.

1.1) Structure of dissertations

The work presented in this thesis demonstrates versatile techniques for bionanotechnological interfacing of biologically relevant molecules on the surface TMDCs and its implementation for development of novel antibacterial systems.

In Chapter 2, I introduce background on two-dimensional materials, crystal structure and its mechanical and optical properties. I also describe the biological

applications of two-dimensional materials, followed by a detailed discussion on the antibacterial applications of two-dimensional materials.

In Chapter 3, I present generalizable techniques for dispersing TMDCs using short synthetic single-stranded DNA, followed by studies of DNA sequence dependence, characterization of DNA-dispersed TMDCs, *in vitro* antibacterial activity evaluations of these designed systems, and mechanistic evaluation of the system.

In chapter 4, I present a novel TMDC/poly-L-lysine system that targets the bacterial cell membrane of multidrug-resistant bacteria and eliminates them. Furthermore, these systems demonstrate a multimodal mechanism of action against bacteria. Also, this chapter presents a detailed mechanistic study of antibacterial action of these designed systems.

In chapter 5, I conclude my thesis summarizing the work and discussing the future applications of these designed systems.

Chapter 2

Background and literature review

2.1) Graphene and its analogue: Structure and applications

Graphene, the archetypal two-dimensional material, consist of a single-atom-thick layer of carbon atoms arranged in a hexagonal lattice structure[22,23]. Structurally, each carbon atom of graphene sheet is sp^2 hybridized, with each carbon atom in the planer sheet is held together by σ-bond whereas out of plane delocalized π-electron lead to the generation of weak van-der Waal forces between each layer of graphene in the bulk crystal structure, graphite[24]. Furthermore, electrons in graphene behave as Dirac fermions, enabling them to migrate in ambient conditions with little scattering[25-27]. The unique structural features of graphene leads to a wide range of extraordinary electronic properties, which includes room-temperature electron mobilities of ~10,000 $cm^{-2}s^{-1}$, charge carrier concentrations of 10^{13} cm^{-2}, zero-bandgap 2D semiconductor behavior, unusual Hall effect for both electron and hole carriers and high thermal conductivity[26,28-31]. Furthermore, graphene exhibits extraordinary mechanical strength, with breaking strength around 42 N m^{-1} and a Young's modulus around 1.0 TPa[32]. The remarkable properties of graphene were further implemented for electronic applications, including high speed electronic and optical devices[33-40], energy generation and storage[41-47], hybrid materials[48,49], chemical sensors[50], and DNA sequencing[51-53].

Apart from the impressive mechanical and electrical properties of graphene, the high surface area and unique physiochemical properties of graphene have been further explored for wide range of biomedical applications and translational research, which

includes tissue engineering[54], molecular imaging and gene therapy[55]. Despite of some successes in biological applications, the implementation of graphene for clinical applications is being hindered, due to its potential toxicity and biocompatibility towards mammalian cells[56]. The reason for graphene's toxicity towards mammalian cells is still not well known, but presence of free electron on surfaces of graphene is considered a key factor, which imparts significant toxicity towards mammalian cells. To overcome this problem, researchers have modified the surface of graphene using chemical treatment to produce graphene oxide (GO) and reduced graphene oxide. The biocompatibility studies of GO on a,wide range of mammalians cell line such as L929[57], HeLa[58], human fibroblast[59], human lung cancer cells A549[60] and human hepatoma HepG2[61] showed no to little cytotoxicity.

The biocompatibility and easy functionalization of GO inspired researchers to explore it further for biomedical applications. Furthermore, the high elasticity, flexibility and adaptability to flat or irregular shaped surfaces of graphene-based materials have been used for tissue engineering[30,62]. Studies have demonstrated graphene-based materials to promote growth, proliferation and adhesion of human mesenchymal stem cells and mouse induced pluripotent stem cells (iPSCs), with GO supporting better attachment and proliferation compared to graphene[63-65]. Also, the large surface area and versatile chemistry of graphene-based nanomaterial was further explored for development of probes for wide range of molecular imaging techniques such as magnetic resonance imaging (MRI), optical and positron emission tomography (PET). For example, *Peng et al.* designed a graphene based biocompatible intracellular imaging system by conjugating fluorescein on the surface of graphene using PEG linker[66]. In

another reports, *Gollavelli et al.* designed a graphene based multifunctional imaging systems using microwave assisted reduction of GO in the presence of ferrocene, which led to the formation of iron nanoparticles on the surface of graphene[67].

The ultrahigh surface area and large sp^2 hybridized carbon area was further explored for drug delivery and gene delivery[68]. The large hydrophobic surface of graphene nanosheets was used for loading hydrophobic anticancer drugs using π-π stacking interactions. The high solubility of GO was further used to load water-insoluble aromatic cancer drugs such as SN38, which in turn overcomes the aqueous the insolubility problem of anticancer drugs[69]. Performance-wise these drugs loaded GO platform performs better than FDA approved SN38 prodrug, irinotecan[69]. In another report, to further increase the performance of GO based delivery vector, MCF-7 cell overexpressed receptor molecule, folic acid was covalently conjugated on the surface of graphene oxide and two anticancer drugs, DOX and CPT was loaded on the nanosheets, which in turn showed better performance than drug alone[69]. Also, GO based platform was further used for development of safe gene delivery vector for gene-based therapeutics. The attachment of plasmid DNA on the surface of graphene, prevents degradation of oligonucleotides from enzymatic cleavage. For graphene-based gene delivery, the most well-known techniques mainly involve attachment of cationic charged polymer, PEI on the surface of GO followed by electrostatic attachment of plasmid DNA[70]. Also, previous reports have shown the delivery of short interfering RNA and DOX using PEI grafted GO, which in turn shown higher anticancer efficiency compared to other systems[71].

Although graphene-based systems have shown promise for biomedical applications, their non-biodegradable nature coupled with long-term toxicity of

nanomaterials hinders its implementation for clinical applications. The drawback imposed by the graphene-based materials inspired researchers to hunt for other classes of two-dimensional materials, which led to the discovery of many other materials such as semiconducting two-dimensional transition metal dichalcogenides (TMDCs), boron nitride, borophene, silicene, germane and MXene.

2.2) Transition metal dichalcogenides (TMDCs): Structure, Properties and Applications

TMDCs are a class of layered materials where each transition metal (M) is sandwiched between two chalcogen atom (X) atomic layers to form a monolayer of atomic units MX_2, with few exceptions such as 2:3 quintuple layers (M_2X_3) and 1:1 metal chalcogenides (MX)[3,72]. Based on the atomic arrangement, TMDCs can be further categorized into different geometric forms including trigonal prismatic (hexagonal, H), octahedral (tetragonal, T) and distorted phase (T'), Figure 1.2. In the single-layer 1H phase of TMDCs, each metal atom forms a tetrahedral geometry along +Z and -Z directions, and in multilayer structures, each tetrahedral layer is held together by weak van der Waals forces. In 1T phase, metal bonding with each chalcogen atom adopts a trigonal geometry with each phase are arranged in antiparallel orientations, to form an antiparallel trigonal prismatic geometry. In 1T' phase, the crystal structure undergoes further distortion along z direction to form a distorted trigonal prismatic geometry[73,74].

Unlike graphene, TMDCs exhibit a finite bandgap. In bulk form, most TMDCs have an indirect band gap, whereas monolayer forms show a direct band gap, with few exceptions such as GaSe and ReS_2[75,76]. For example, TMDCs such as MoS_2 (1.8 eV), $MoSe_2$ (1.5 eV), (2H)-$MoTe_2$ (1.1 eV), WS_2 (2.1 eV) and WSe_2 (1.7 eV) shows direct

band gap in monolayer form, whereas it shows indirect band gap in bulk form, Figure 1. 2. Geometrically, the 2H phase is the most stable form for MX_2 at room temperature, whereas MX_2 phase transforms to the unstable 1T phase following chemical treatments or electron beam irradiations[77]. Electronically, 1T MoS_2 phase is more conductive than the semiconducting 1H phase[78]. Contrary to MoS_2, both 1T and 1T' phase is stable for WSe_2 at room temperature, and lack of cohesive energy between each layer makes easy interconversion between two phases[79]. The d-block transition metal dichalcogenides such as titanium (Ti), chromium (Cr), nickel (Ni), vanadium (V), niobium (Nb) and tantalum (Ta) shows metallic behavior at room temperature[3].

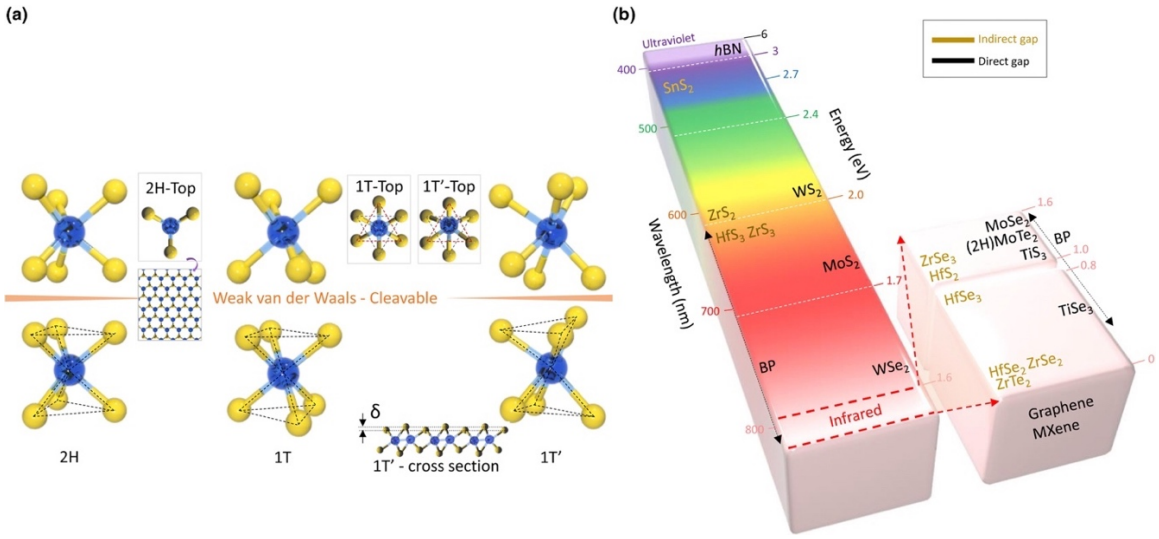

Figure 1.1: Crystal structure and electronic properties of TMDCS (a) Crystal structure of TMDCs. Cleavable planes for three different crystal structure of TMDCs 1H, 1T and 1T' is shown. (c) Band gap of 2D layered materials. The colors correspond to the wavelength of bandgap of layered materials. Figure adapted with permission from [80].

The TMDC exhibit intrinsic semiconducting properties, with band gap increasing with decreasing thickness. The semiconducting property and high carrier electron mobility of TMDCs, have been further used for field-effect transistors. Furthermore,

TMDCs also exhibit exceptional mechanical properties. For example, Young's modulus for few layers of suspended MoS_2 nanosheet is ~0.33 ± 0.07 TPa[80]. Further mechanical studies of MoS_2 have shown ~180 ± 60 N m^{-1} high in-plane stiffness and ~270 ± 100 Gpa Young's modulus for single layer MoS_2[80]. The high crystallinity and defect free nature of atomically thin TMDCs led to better Young's modulus, when compared to stainless steel and graphene oxide[81]. Furthermore, valence electrons of the metal atom undergo bonding with lone pair of electrons terminated from chalcogen plane, resulting in absence of dangling bonds on the basal plane of TMDCs which in turn makes it chemically inert, and making them a promising candidate for biomedical applications[21]. Also, TMDCs shows external environment dependent photoluminescence (PL), which is further exploited for designing of biosensors [16,82-85]. Also, the electronic band structure of TMDCs exhibit stronger optical absorption in the near-infrared region (NIR), compared to graphene oxide and gold nanorods[86]. The NIR absorption of TMDCs was further explored for designing of photothermal agents for therapeutics and drug delivery in tumor tissues [83]. For example, MoS_2 at a concentration as low as few 100s ppm can increase the temperature to >80 °C on exposure to NIR for few minutes.[83]

Depending on the application, there are two well-known approaches for synthesis of TMDCs, top-down and bottom-up. The bottom up approach refers to the synthesis of TMDCs starting from precursors. The most widely used bottom up approach is chemical vapor deposition (CVD), which refers to the techniques in which solid powder precursors are thermally evaporated and chemically made to react on a solid surface or substrate to form a desired TMDCs layer[87,88]. For example, MoS_2 is synthesized by heating MoO_3 and S powders in a glass tube to form vapors of Mo and S, which reacts on a substrate such as

SiO_2 and sapphire to form MoS_2 monolayer. The bottom up approach is highly efficient for formation of large area monolayer MoS_2 surfaces, which makes it a perfect candidate for fabrication of large-scale diagnostic devices. The top-down approach refers to exfoliation of bulk crystal of TMDCs to its constituent layers using mechanical or chemical treatments.

The most well-known top-down approach are, mechanical exfoliation and liquid exfoliation. The mechanical exfoliation of TMDCs involves the use of adhesive for breaking down interlayer force, followed by transferring of exfoliated flake on different surfaces or substrates[6]. The mechanical exfoliation of TMDCs generally yields high quality flakes, but less scope for thickness controllability, is the biggest drawback for these techniques. The high quality of flakes produced by mechanical exfoliation techniques makes it a perfect candidate for designing of chip-based sensors. The other technique, liquid phase exfoliation of bulk TMDCs crystal refers to ultrasound-assisted chemical exfoliation of TMDCs, and shear-force-assisted exfoliation of TMDCs in the presence of dispersing agents. The liquid phase exfoliation of TMDCs either involves the chemical treatment of TMDCs using intercalating reagents, n-BuLi, followed by ultrasonication to yield mono to few layers of TMDCs or *in-situ* ultrasonication of TMDCs in the presence of dispersing agents such as surfactants, biomolecules etc. to exfoliate and disperse TMDCs in solutions[89]. Although this technique leads to poorer quality nanosheets, the high concentrations and surface tunability with wide varieties of dispersing agents, make it one of most promising techniques for generation of nanomaterials for biomedical applications.

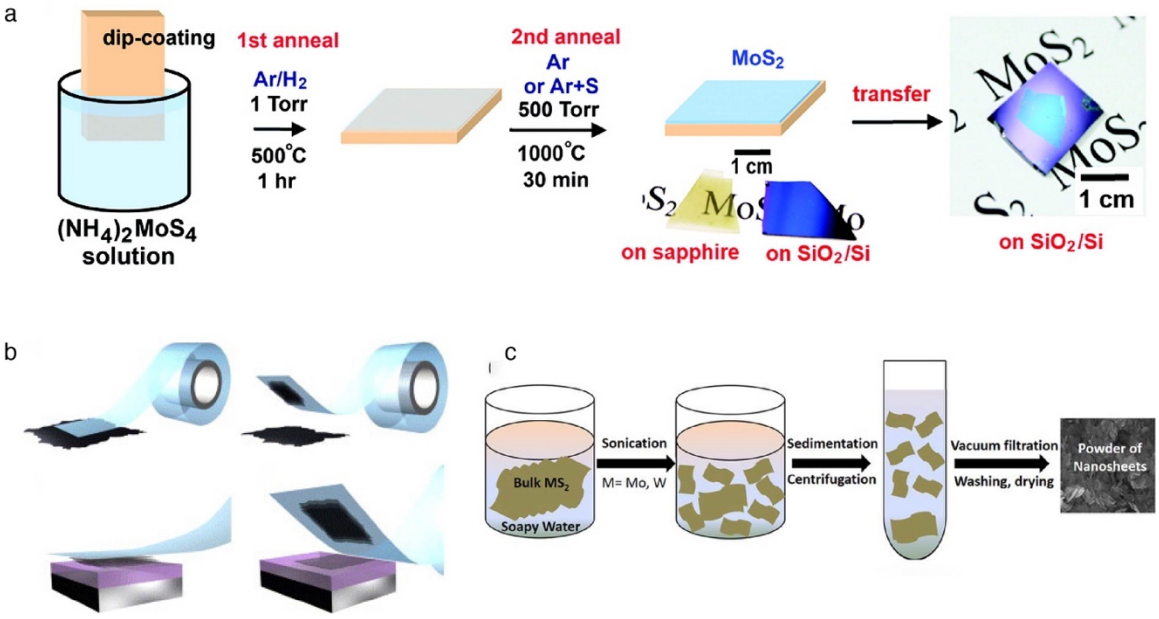

Figure 1.2: Techniques for synthesis and exfoliation of TMDCs (a) Chemical vapor deposition starting from precursor[90] (b) Mechanical exfoliation of TMDCs from bulk crystal using tape method.[91] (c) Liquid phase processing of TMDCs using sonication.[92] Figure adapted with permission from: (a) ref. [90] Copyright (2012), American Chemical Society. (b) ref [91] Copyright (2012), IOP Publishing (c) ref [92] Copyright (2015), Springer Nature.

2.3) Biological applications of two-dimensional transition metal dichalcogenides

For designing materials for use in biological systems, the first step involves careful engineering of the nanomaterial hybrid structure to enhance biological and nanomaterial interactions, without compromising the cellular viability towards human cells. The two well-known strategies in this regard are, functionalization and intercalation, Figure 1.4. Functionalization is a technique which involves covalent modification of basal plane or edges using well-known free radical and disulfide chemistry for attachment of biologically relevant functional moieties. For example, MoS_2 multi-functional drug carriers for cancer treatment were made using surface functionalization of MoS_2 with lipoic acid conjugated PEG using thiol chemistry.[93] In

intercalation strategies, TMDCs is dispersed either using chemical treatment or ultrasonication in the presence of biocompatible amphiphilic surfactant. In chemical exfoliation, TMDCs are treated using strong intercalating agents, n-BuLi, to intercalate small Li ions to weaken the interlayer forces, followed by ultrasonication in the presence of biologically functional moiety, which leads to exfoliation and functionalization of TMDCs[94]. The presence of toxic Li ion in chemical exfoliation hinders its biological applications. The other alternative strategy for exfoliation of TMDCs mainly involves *in-situ* ultrasonication of TMDCs in the presence of biologically active amphiphilic molecules to generate biologically active molecules encapsulated nanosheets[19]. The *in-situ* ultrasonication leads to generation of large chaotic forces in solution, which in turn lead to the breakdown of van der Waal forces between each layer, and amphiphilic molecules encapsulate nanosheets, which in turn provide stabilization to each nanosheets using electrostatic or steric repulsion. Despite its success in exfoliating the TMDCs, there are few reports for TMDCs exfoliation in the presence of biological active molecules such as peptides, proteins aptamers and DNA. According to Zadeh et al., the exfoliation of TMDCs in the presence of these molecules will require careful consideration of pH, temperature and energy consideration[21].

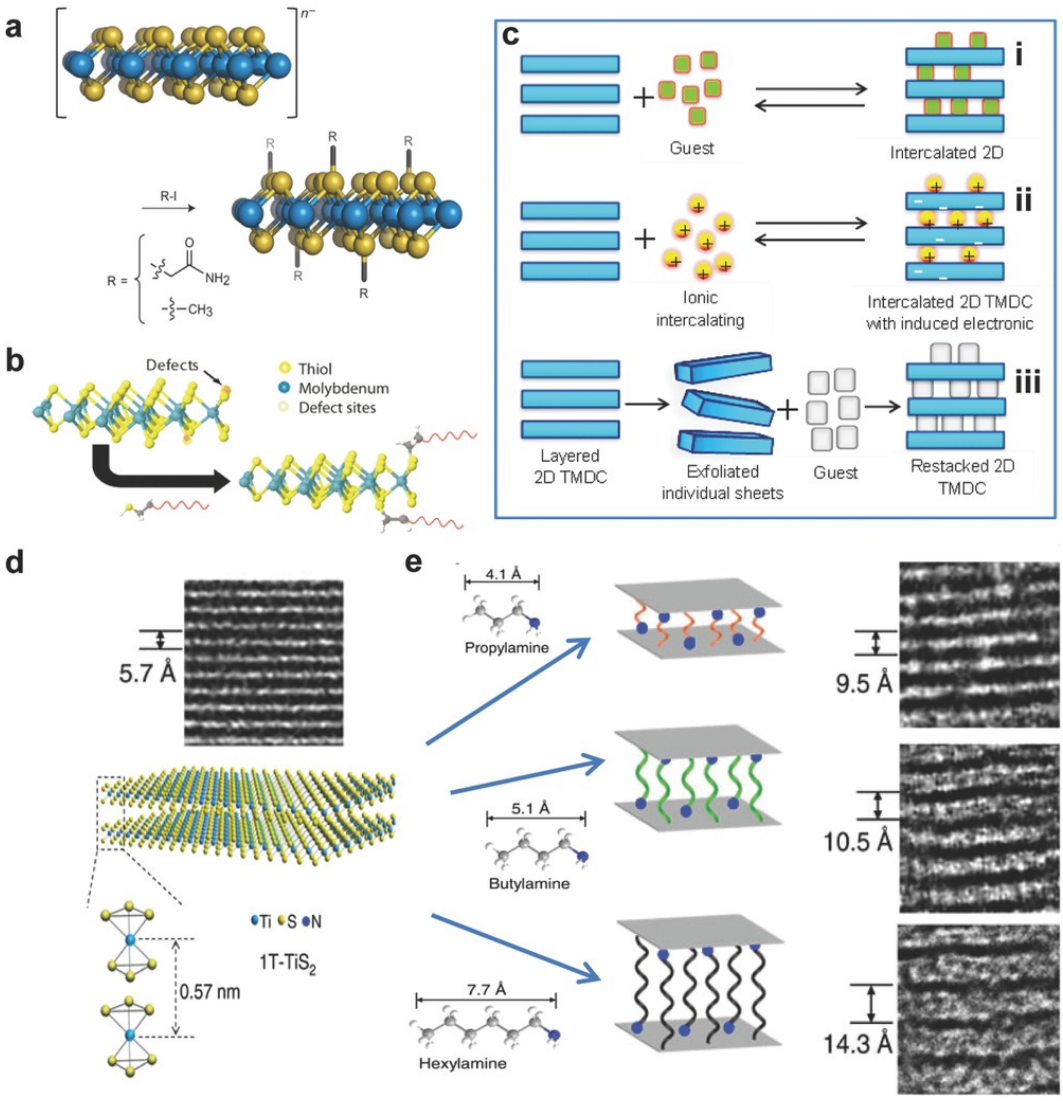

Figure 1.3: Solution-phase processing of TMDCs using functionalization and intercalation for biological applications. A) Covalent functionalization of 1T phase of TMDCs nanosheets using a 2-iodomethane.[95] (b) Disulfide functionalization of MoS_2 using thiol moieties. (c) Exfoliation of TMDCs using intercalation strategies: (i) general intercalation strategies, (ii) charged particle intercalation strategies, (iii) exfoliation and restacking processes. (d) HRTEM images showing exfoliated TiS_2 (e) Schematic showing the change in interlayer distance of TiS_2, with change in carbon length of amine.[96]. Figure adapted with permission from [21]. Copyright © 2015 WILEY-VCH Verlag GmBH & Co. KgaA, Weinheim.

Unlike graphene, the absence of dangling bonds on the basal plane of TMDCs has inspired researchers to explore the biological applications of TMDCs. Furthermore, high

surface area of TMDCs makes them promising candidates for designing systems for biological applications. Toxicity studies of TMDCs have shown them to be less toxic compared to graphene analogues.[97,98]Also, variations in the toxicity of TMDCs have also been observed for different TMDCs analogues. For example, MoS_2 and $MoSe_2$ did not impart any toxicity to lung cancer cells, whereas WSe_2 induced significant toxicity, but lower than graphene and graphene oxide[97]. Other studies have shown increased toxicity of TMDCs, with decreasing MoS_2 thickness, which can be attributed to the fact that defects and edges play a key role in toxicity of TMDCs[17]. Furthermore, *in-vivo* studies on PEG-functionalized MoS_2, have shown no evidence of toxicity towards mice[7]. Also, the same results were observed for the PEG-functionalized metallic TMDC TiS_2, with no significant toxicity was observed after 2 months of treatment.[99]

The biocompatibility of TMDCs and high hydrophobic surfaces has led to their use as drug-delivering nano-carriers. The loading of hydrophobic drugs on the 2D surface of TMDCs increases the solubility and life span of drugs with the highest reported loading around 240%, higher than graphene oxide[7,100]. Furthermore, 2D TMDCs such as MoS_2 also shown higher near infrared (NIR) absorbance compared to carbon-based material graphene. For example, NIR radiation of MoS_2 suspension can change the temperature of the medium to >80 °C, which were applied for cancer treatments[86]. Also, the high surface area coupled with the photothermal properties of TMDCs is being used for developments of drug-delivery carrier for multimodal cancer treatment. For example, Yin et al. designed a multimodal synergistic delivery vector containing folic acid functionalized PEG on MoS_2 surface and DOX on MoS_2 surface, which was further used for destroying and delaying tumor growth[93]. Similar studies with other TMDCs such as

TiS_2 and WS_2, also showed biocompatibility and drug delivery carrier properties[99,101]. The ability of TMDCs to attenuate X-rays has been used for designing contrast agents for X-ray computed tomographic (CT) imaging[7,10,101]. Also, 2D MoS_2 surfaces have been used for decorating with magnetic resonance imaging (MRI) contrast agents such as iron oxide and Cu^{64}, and further used for photoacoustic imaging[8]. The biocompatibility, mechanical strength and material stiffness of these materials was further explored for designing of 2D TMDCs based matrix for tissue engineering[102,103].

Lastly, the high surface-to-volume ratio, wide range of functionalization strategy and intercalation property of TMDCs was used for designing biosensors. For example, Wu et al. designed MoS_2 based redox sensor for detection of glucoses and dopamine[104]. The photoluminescence (PL) is another property which have been explored for designing of different sensor; the PL of 2D TMDCs can be changes based on intercalation with small molecule, which in turn can be used for detections of small molecules. For example, quenching of PL on intercalation with small molecules with TMDCs have been utilized for designing of blood glucose sensor.[11,102]

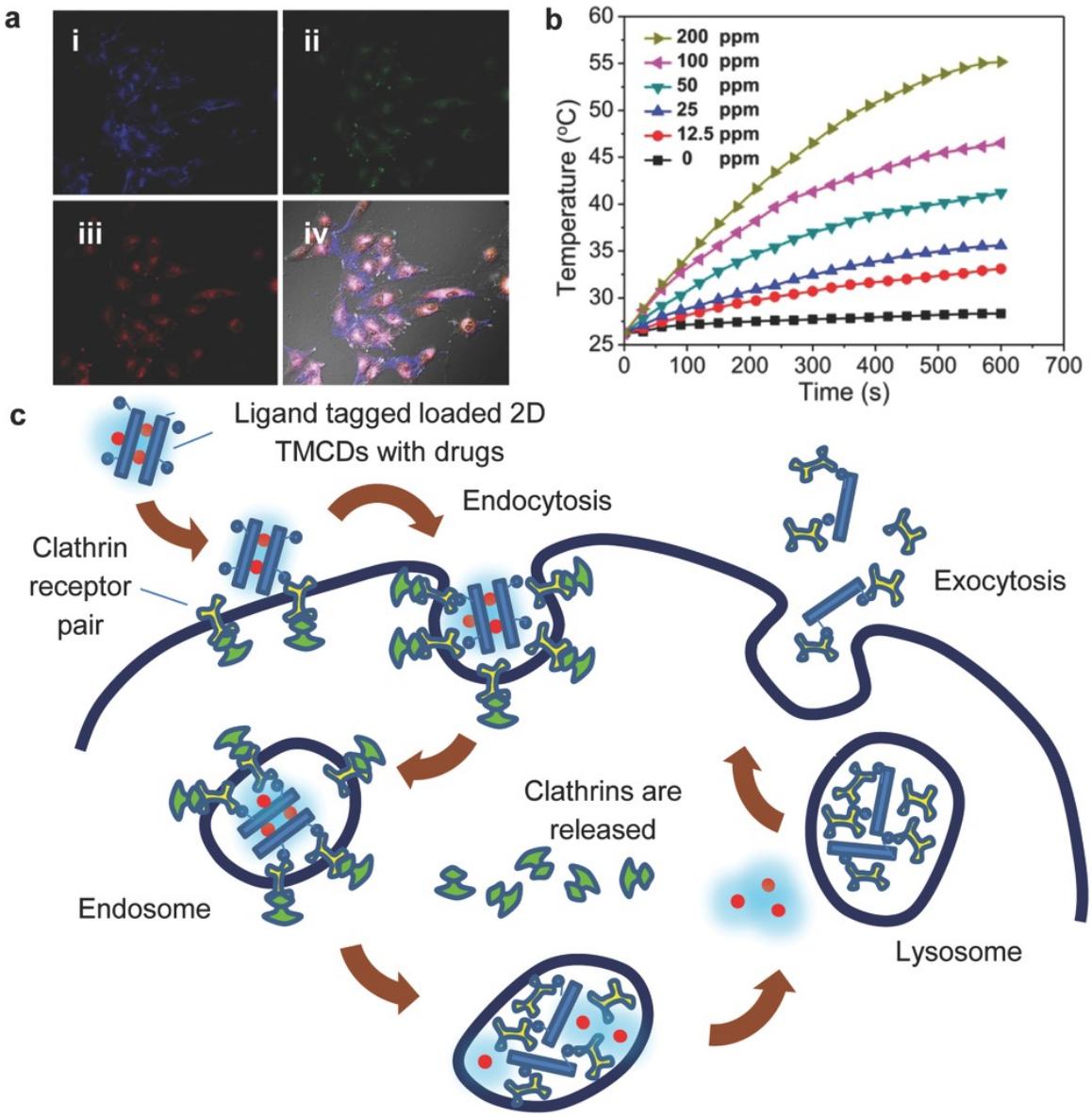

Figure 1.4: Cell imaging, photothermal effect and drug delivery applications of TMDCs (a) Fluorescence imaging of lung cancer cells using MoS_2 nanosheets [85](b) Photothermal profile of MoS_2 nanosheets with respect to concentrations. (c) Drug delivery pathway of 2D TMDCs using clathrin-mediated endocytosis[10]. Figure adapted with permission from [21]. Copyright © 2015 WILEY-VCH Verlag GmBH & Co. KgaA, Weinheim.

2.4) Antibacterial applications of two-dimensional materials

The interesting features of nanomaterials such as high surface area and physiochemical properties have been widely explored for designing of wide range of

material-based antibiotics. The antibacterial action of these nanomaterial holds advantage over traditional antibiotics. Firstly, most of antibacterial actions of these material-based antibiotics is based on physical interactions and chemical reactions, which in turn restrict bacteria from developing resistance to nanomaterial-based antibiotics. Secondly, high surface area of nanomaterials allows loading of antibiotics, which has been used synergistically with nanomaterials for eradicating multidrug resistant bacteria. Thirdly, optical properties of nanomaterials are being further explored for designing of photothermal and photocatalytic based antibacterial systems.

2.5) Antibacterial activity of graphene-based material and its analogue

The interesting physiochemical properties of graphene-based materials (GM) was explored for designing of wide range of antimicrobial systems. Based on previous study, antibacterial mechanisms of GMs occur through two well-known mechanisms, physical interactions and oxidative stress.[105-108]

The physical interactions refer to interactions of bacteria with the sharp edges of nanomaterials, which in turn led to breakdown of cell membrane and finally cell death. This antibacterial action of nanomaterials has been referred to as the 'nano-knife' effect. Hu et al. explored these features and demonstrated antibacterial activity of graphene oxide (GO) and reduced graphene oxide (rGO) against gram-negative *E. coli*, with graphene oxide having better antibacterial performance compared to rGO[109]. In another report, Akhavan and Ghaderi et al., compared the antibacterial activity of GO and rGO nanowalls, and established the fact the rGO showed stronger antibacterial activity compared to GO in solid phase.[110]

Apart from nano-knife effect of GMs, the basal edge of GMs also plays a key role towards antibacterial actions. For example, GMs encapsulate bacteria and cut off nutrients supply from the external environment, which in turn lead to cell death due to nutrient deprivations[111,112]. In another report by Liu and co-workers, they studied effect of lateral dimensions of GO towards antibacterial performance, with larger GO sheets showed higher activity compared to smaller ones[113]. Based on these studies, they postulated that larger graphene sheets are a better encapsulating agent compared to smaller ones, which in turn provide better shielding to bacteria from the external nutrient environment and contribute to different antibacterial activity. Also, the hydrophobic surface of GMs interacts with lipids of bacteria, which in turn causes membrane disruption and finally cell death.[114,115] Furthermore, Tu and co-worker carried out an experimental and molecular simulations of the antibacterial action of GMs and revealed two mechanisms, one involving insertion and cutting, and other one involves destructive lipid extraction of bacterial cell membranes with the assistance of TMDCs hydrophobic surface. [115]

The other well-known antibacterial mechanism of GM based material involves generation and induction of oxidative stress. The oxidative stress generated by GMs is classified into two categories, reactive oxygen species (ROS) dependent and ROS independent. The ROS-dependent antibacterial mechanism refers to the generation and accumulation of ROS, which includes, singlet oxygen, superoxide oxygen, hydrogen peroxide and hydroxyl radical. The ROS independent refers to the interactions of nanomaterials with bacterial surfaces, followed by chemical reaction, which in turn led to induction of oxidative stress within the cell. The oxidative stress generated by GM based

material leads to lipid peroxidation and dysfunction of bacterial cellular machinery, followed by cell death.[116] In this regard, Krishnamoorthy et al. incubated GO with free radical trapper, 5,5-dimethyl-1-pyrroline-N-oxide and used EPR to detect the free radical ion in the medium.[117] Their study revealed hydroxyl radical as the key radical towards ROS dependent oxidative stress. Also, some studies showed GO dispersion generates higher ROS compared to rGO, which can be further co-related with the fact that GO have stronger antibacterial activity compared to rGO[118,119]. Contrary to these studies, others have shown that ROS-independent oxidative stress is a key mechanism towards antibacterial action of GM based material. For example, Liu et al. compared the antibacterial activity of four different GMs (GO, rGO, Graphene and Graphite oxide) and showed the antibacterial performance and found it follows the order, GO > rGO > Graphite > Graphite oxide.[120] Further mechanistic study revealed membrane damage and GSH as a key in antibacterial action, with no observed superoxide ion generation. In another study, Panda et al. coated graphene on four different conducting metal surfaces, Zn, Sn, Ni and steel, and glass as an insulating surface. The antibacterial activity study on these surfaces revealed GO-Zn being the most effective one, followed by GO-Ni, GO-Sn, GO-steel, with no antibacterial activity observed for GO-glass.[121] From these studies, it can be concluded that antibacterial action is directly dependent on conductivity of surfaces with highest antibacterial action observed for highest conductive surfaces. Despite of all these studies, the exact antibacterial mechanism for graphene-based material is still unknown and needs further investigation.

Furthermore, photothermal and photocatalytic property of GMs, was further explored for designing of antibacterial materials. The photothermal method refers to the

generation of local heat on incident of light, whereas photocatalytic property refers to production of free radical such as superoxide and peroxide ion, which in turn lead to generation of oxidative stress in bacterial cell. Interestingly, one atomic thick layer graphene is nearly transparent to NIR absorption with no photothermal activity, whereas rGO exhibits extraordinary photothermal activity. Khan et al. demonstrated GO based photothermal therapy for antibacterial activity, antifungal activity and accelerated wound-healing[122]. In another report, Wang et al. specifically modified the surface of rGO with anti- *S. aureus* antibody and specifically made it to target and eradicate *S. aureus* using photothermal therapy[123]. In another report, Qian et al. designed a pH-dependent photothermal antibacterial system by specifically conjugating glycol chitosan with the carboxy group of graphene.[124] The pH dependent systems are negatively charged in healthy tissues, whereas it undergoes transition to positive charge in acidic environment of wounds and becomes more active in infected areas.

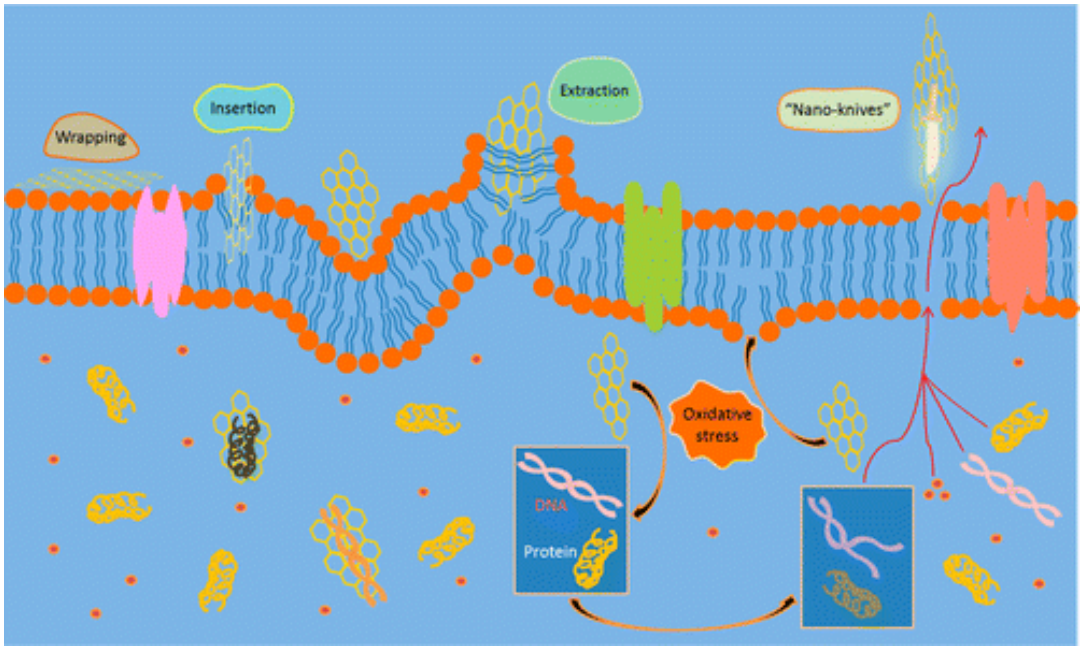

Figure 1.5: Antibacterial actions of graphene-based materials.[125] Figure adapted with permission from: ref. [125] Copyright (2016), American Chemical Society.

2.6) Antibacterial activity of non-graphene two-dimensional materials

The antibacterial activity of GMs inspired researcher to study the antibacterial activity of other classes of materials, in particular TMDCs. Previous studies on antibacterial action of TMDCs, showed oxidative stress, membrane rupture and release of MoO_4^{2-} as two key antibacterial mechanism.[126,127] Previous studies on antibacterial action of MoS_2, have shown chemically exfoliated ce-MoS_2 have stronger antibacterial activity compared to raw MoS_2.[126] These antibacterial actions can be attributed to the fact that ce-MoS_2 has stronger interactions with bacteria compared to raw MoS_2, which in turn induces higher oxidative stress and membrane rupture to bacterial cell. In another study, Wu et al. studied the effect of MoS_2 nanosheets on metabolic pathways of *E. coli* and revealed that there is no change of metabolites expression in *E. coli* at low concentrations of MoS_2 nanosheets, whereas it suppressed the expression of metabolites at high concentrations of MoS_2 nanosheets[127]. In another study, Tang et al. vertically aligned MoS_2 was generated on Ti substrates and the antibacterial activity tested on both gram-negative *E. coli* and gram-positive *S. aureus*.[128] Based on their studies, MoS_2-coated Ti substrates inhibited both strains of bacteria, but two different antibacterial mechanisms were reported for these strains. The *S. aureus* elimination occured through both ROS and MoO_4^{2-} ion release, whereas *E. coli* elimination occured only through ROS, with no effect from MoO_4^{2-} ion.

To further increase the antibacterial efficiency of TMDCs, researchers have modified the antibacterial systems using functionalization, loading and catalytic

properties. In one report, Kim et al. modified MoS_2 using GO and studied the antibacterial activity against bacteria using label-free holotomographic microscopic techniques[129]. Their study revealed that an ROS-independent pathway is responsible for antibacterial activity. In another study, Pal et al. anchored titanium nanoparticles on the surface of MoS_2 and showed membrane damage and oxidative stress as a key mechanism towards antibacterial action.[130] Researchers explored the high surface area and functionalization chemistry of MoS_2 and anchored different cationic analogues on the surface of MoS_2. In another report, Pandit et al. functionalized MoS_2 with cationic ammonium derivatives of different length and studied the antibacterial activity against superbugs.[131] According to their study, the cationic analogues successfully eradicated both planktonic cells and biofilms, using oxidative stress and membrane depolarization. The high surface area of MoS_2 was further explored for designing of synergistic systems containing antibiotics and bactericidal silver nanoparticles. Using thiol functionalization chemistry, Cao et al. attached silver ions on cysteine-modified MoS_2 nanosheets and further coated them with positively charged cationic polyelectrolyte polydiallyldimethylammonium chloride (PDDA).[132] The system successfully eradicated planktonic from both *in-vitro* and *in-vivo* systems. Also, these systems showed better efficiency compared to silver ion generated from equivalent concentrations of silver nanoparticles. In another report, Zhang et al. functionalized MoS_2 using chitosan and loaded the surface with the antibiotic tetracycline hydrochloride, which synergistically eliminated bacteria and biofilms.[133]

The photothermal and photocatalytic properties of MoS_2 were also explored for designing antibacterial systems. In one report, Fan et al. studied the antibacterial activity

of two classes of MoS_2, chemically exfoliated MoS_2 (ce-MoS_2) and annealed chemically exfoliated MoS_2 (Ae-MoS_2) in the presence of the sacrificial electron donor ethylenediaminetetraacetic acid (EDTA).[5] The ce-MoS_2 showed higher photocatalytic antibacterial activity compared to Ae-MoS_2, which is attributed to the fact that ce- MoS_2 has a higher concentration of 1T-phase compared to 1H phase. The 1T-phase has a favorable band gap for generation of ROS under visible-light illumination compared to 1H-phase. In another report, Liu et al. designed few-layer vertically aligned MoS_2 (FLV-MoS_2), which was further implemented for water disinfection under incident visible light. The FLV-MoS_2 has a higher band gap compared to bulk MoS_2, which in turn favors the generation of more ROS in water and higher disinfection efficiency. Furthermore, Cu-deposited FLV-MoS_2 showed accelerated disinfection efficiency compared to pristine FLV-MoS_2. The disinfection mechanism of FLV-MoS_2 is due to photoinduced production of ROS, with H_2O_2 as the key ROS species involve in elimination of bacteria.[134]

TMDCs also show peroxidase-like catalytic activity, which have been further used for designing peroxidase-based antibacterial systems. Yin et al. designed a PEG functionalized MoS_2 based nanoflower and used it in synergy with low concentrations of H_2O_2 to generate hydroxyl radical. The hydroxyl radical induced oxidative stress in bacterial cells, which in turn led to elimination of bacteria.[135] In another report, Huang et al. exfoliated TMDCs in the presence of carboxyl modified silk fibroin (CMSF), studied the peroxidase activity of TMDCs and used it for *in-vivo* wound dressing. According to their study, $MoSe_2$-CMSF showed the best peroxidase performance among all other TMDCs, catalyzed H_2O_2 to generate hydroxyl radical, which in turn eliminated bacteria.

The $MoSe_2$-CMSF was used with disinfectant H_2O_2 in wound dressing, which accelerated the healing rate compared to H_2O_2.[136] Furthermore, there is some reports using WS_2 for antibacterial activity. For example, Liu et al. coated WS_2 with SDS and used it for antibacterial activity against *E. coli* using membrane damage and oxidative stress.[137] Bang et al. coated WS_2 and WSe_2 with long single-stranded DNA and demonstrated antibacterial activity of DNA-coated WS_2 and WSe_2 against *E. coli*. According to their study, WSe_2-ssDNA demonstrated stronger antibacterial activity compared to WS_2-ssDNA, which has been attributed to the fact that p-type semiconducting behavior of WSe_2 promotes stronger antibacterial activity compared to WS_2.[20]

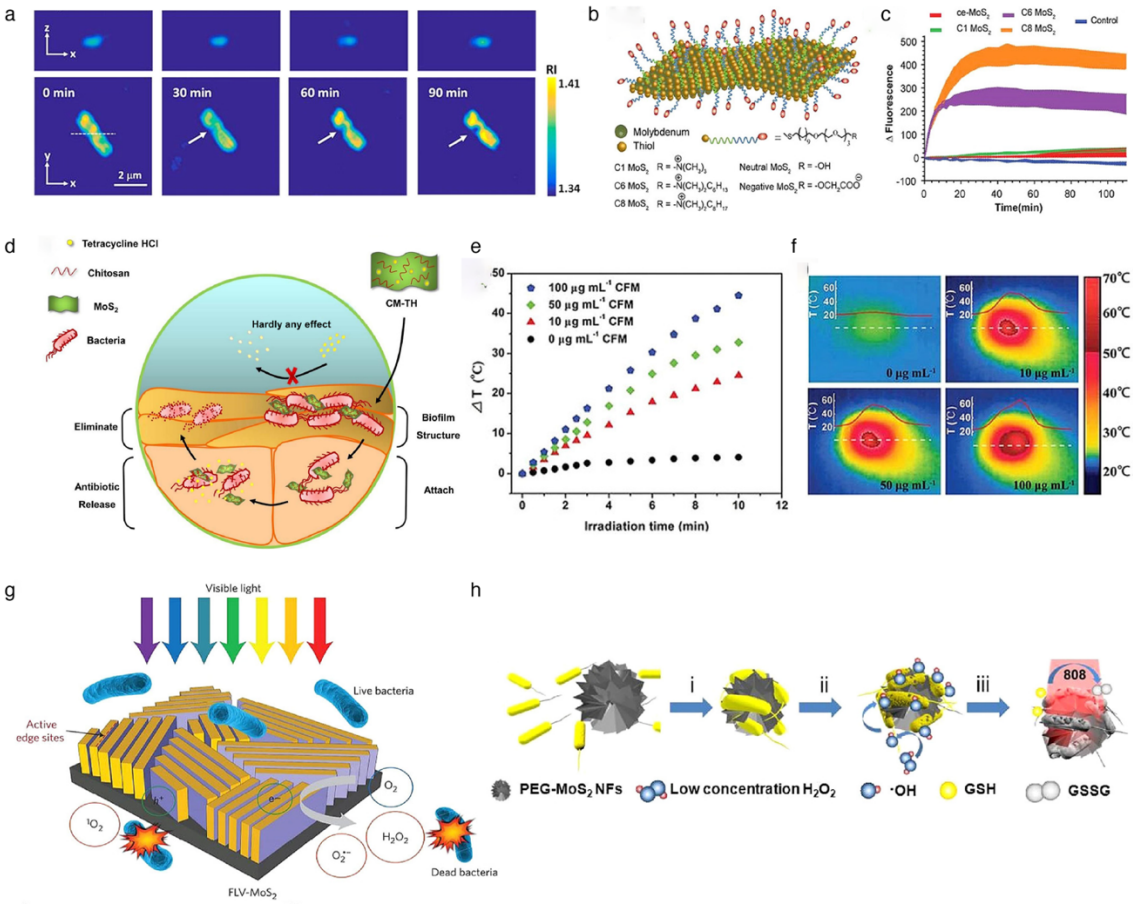

Figure 1.6: Antibacterial action of TMDCs using photothermal, photocatalytic, membrane-induced damage and peroxidase catalysis. (a) 3D tomogram images of the

bacterial membrane after contacting GO-MoS_2 surfaces. The image demonstrated disrupted bacterial membrane.[129] (b) Covalently functionalized MoS_2 with positively charged cationic polymer having varying carbon chain length. (c) Change in membrane polarization after interactions with covalently functionalized MoS_2 with cationic charged polymer[131]. (d) Schematic images demonstrating the synergistic effect of antibiotic loaded MoS_2 for disruption of biofilms. The chitosan charged MoS_2 nanosheets disrupt biofilms extracellular matrix and deliver antibiotics inside biofilms to eliminate bacteria. Photothermal heating curve of chitosan functionalized MoS_2 after irradiation with a laser.[138] (f) Thermal mapping of corresponding chitosan modified MoS_2 (figure e) after irradiation with laser. (g) Photocatalytic effect of vertically aligned MoS_2 to generate reactive oxygen species after irradiation with visible light. Incident of visible light on vertically aligned MoS_2 led to generation of reactive oxygen species which led to generation of oxidative stress in bacteria and finally cell death.[134] (h) Schematic demonstrating peroxidase catalytic like activity of MoS_2 nanoflower in the presence of H_2O_2 to generate reactive oxygen species for elimination of bacteria. Figures adapted with permission from: (a) ref [129]. Copyright (2017), American Chemical Society. (b, c) ref [131] Copyright (2016), American Chemical Society (d, e, f) ref [138] Copyright © 2016 WILEY-VCH Verlag GmbH & Co. KgaA, Weinheim. (g) ref [134] Copyright (2016) Springer Nature (h) ref [135] Copyright (2016), American Chemical Society

Researchers have also explored the antibacterial activity of another class of two-dimensional materials called Mxenes. There are only few reports on the antibacterial activity of Mxene. The first report on antibacterial activity of Mxene was done by Rasool et al., who studied $Ti_3C_2T_x$. According to their study, $Ti_3C_2T_x$ eliminates both gram-positive *B. subtillis* and gram-negative *E. coli* using sharp edge induced membrane rupture and oxidative stress.[139] Extending these studies, Rasool et al. coated hydrophilic $Ti_3C_2T_x$ on polyvinylidene fluoride membranes and demonstrated the anti-biofouling property of the membrane[140]. In another study, Pandey et al. demonstrated rapid water purification using $Ti_3C_2T_x$ coated membrane.[141] Despite of these reports on antibacterial activity of Mxene, there is still lot unknown about the probable antibacterial mechanism of Mxene.

Chapter 3

Elimination of Multidrug Resistant Bacteria by Transition Metal Dichalcogenides Encapsulated by Synthetic Single-Stranded DNA

3.1) Introduction

Antibiotic drug resistance is recognized as one of the most pressing threats to global health. Spurred by the misuse and overuse of commonly prescribed antibiotics, drug-resistant bacteria are becoming increasingly common and infections that were once easily treated can now force patients into extended hospital stays. In the United States alone, infections by drug-resistant bacteria have been estimated to cause 2 million cases of serious illness and 23,000 deaths each year, leading to billions of dollars in economic and societal costs[142]. Despite this alarming threat, the number of antibiotics under development remains low, raising the possibility of rampant drug resistance reversing many of the advances of modern medicine. This global health challenge thus demands new approaches to combatting and eradicating bacterial infections.

Two-dimensional (2D) materials have emerged as promising antibacterial materials owing to their high surface areas and atomically thin edges, which can promote strong interactions with bacterial cell walls, and in some cases the ability to generate redox species to trigger cell death. Furthermore, the multifaceted antibacterial killing action of 2D materials compared to traditional antibiotics, makes the development of resistance less likely. Out of these materials, graphene and its close relative graphene oxide (GO) have been most extensively studied and have provided varying levels of antibacterial activity depending on the preparation and treatment method.[139] In one

particularly effective preparation, graphene oxide paper showed 98.5% *Escherichia coli* inhibition at 85 μg ml^{-1}, whereas 100% elimination was observed for *Pseudomonas aeruginosa* at 100 μg ml^{-1}.[143] Electrochemically produced graphene quantum dots induced oxidative stress in bacteria and eliminated 80% of *E. coli* and 92% of *Staphylococcus aureus.*[144] Furthermore, Tu et al. studied the antibacterial action of GO using molecular dynamic simulations and experimental studies. They showed that insertion and cutting of the bacterial cell membrane using the sharp edges of GO, followed by destructive extraction of lipid molecules of bacterial membrane as key mechanism for elimination of bacteria.[114] Transition metal dichalcogenides (TMDCs), which have been shown to have better biocompatibility than graphene and can be enzymatically degraded, have also been studied for antibacterial activity [145]. Chemically exfoliated MoS_2, for instance, successfully killed 93.4% of *E. coli* cells upon exposure at 80 μg mL^{-1} [146] while the same concentration of WSe_2 coated by long strands of salmon-derived DNA eliminated only 82.3% of the same bacteria[147]. Hydrothermally synthesized WS_2 was shown to kill 98.67% and 99.98% of *E. coli* and *Bacillus subtilis* cells, respectively, but only at very high concentrations of 250 μg mL^{-1}.

Despite their clear antibacterial activity, these 2D TMDCs failed to match the activity of common antibiotics, which can eliminate >99.999% of cells at similar or lower concentrations. To obtain comparable levels of activity, 2D TMDCs have required more aggressive conditions and light-driven reactions. WS_2 dispersed in the surfactant solutions completely eliminated cultures of *E. coli* and *S. aureus,* but it exhibited significant toxicity toward human cell lines.[137] Liu et al. demonstrated a water disinfection system that employed vertically aligned MoS_2 layers visible light to

eliminate >99.999% of *E. coli* and *Enterococcus faecalis* cells; however, this light-driven mechanism would be challenging to apply to wound bacterial infections[148]. In another report, Pandit et al. covalently conjugated hydrophobic variants of quaternary ammonium salts to chemically exfoliated and ultrasonicated MoS_2 using disulfide chemistry and demonstrated elimination of planktonic gram-positive *S. aureus*, gram-negative *P. aeruginosa* and biofilms, using membrane polarization and oxidative stress.[18,131] In another report, peroxidase-like catalytic activity of MoS_2 nanoflowers was explored for generating hydroxyl radical from H_2O_2, which in turn led to generation of oxidative stress and cell death.[135] Despite of these successes, the harsh treatment conditions, difficult synthetic routes, light-driven mechanism and toxicity towards mammalian cells of previously developed systems hinders their implementation in clinical applications.

Herein, we describe a novel preparation of 2D TMDCs, in particular of $MoSe_2$, that provides remarkable antibacterial activity against multidrug resistant (MDR) strains bacteria. These antibacterial materials consist of 2D TMDCs coated by short sequences of single-stranded ssDNA. By using appropriate sequences of ssDNA, we successfully prepared stable dispersions of MoS_2, $MoSe_2$, WS_2, and WSe_2 in aqueous solution and confirmed their two-dimensional character using TEM and AFM. We find that $MoSe_2$ nanosheets encapsulated by the T_{20} DNA sequence do not exhibit toxicity against human cells yet are capable of complete elimination of 'ESKAPE' strains at concentrations as low as 75 μg mL^{-1} and provide substantially higher antibacterial activity than widely studied graphene oxide and other preparations of 2D TDMCs. Further mechanistic analysis of $MoSe_2/T_{20}$ showed that the sharp edges of the nanomaterials leads to insertion into the bacterial cell membrane causing membrane damage, followed by change in

membrane potential and generation of oxidative stress, which in turn triggers programmed cell death.

3.2) Results and Discussion

3.2.1) Exfoliation and encapsulation of 2D TMDCs using short ssDNAs

Inspired by previous work exploiting single-stranded DNAs for wrapping single-walled carbon nanotubes[149-156], we attempted to use short synthetic ssDNA sequences for exfoliation and stabilization of four TMDC compounds: MoS_2, $MoSe_2$, WS_2, and WSe_2. Based on the amphiphilic structure of ssDNA, we anticipated that the hydrophobic DNA bases would undergo strong π-stacking interactions with the hydrophobic surfaces of the TMDCs, enabling the hydrophilic sugar-phosphate ssDNA backbone to interface with surrounding water molecules. The negatively charged phosphate groups in the backbone would also provide strong electrostatic repulsion to suspend each flake in solution and prevent nanosheet restacking (Figure 1a). Given the sequence dependence of ssDNA dispersions of carbon nanotubes[157], we investigated the ability of seven 20-nucleotide (nt) ssDNAs containing different sequences of the four canonical DNA bases adenine (A), cytosine (C), guanine (G), and thymine (T) to disperse the TMDCs. These sequences contained 20-mer repeats of the bases (A_{20}, C_{20}, and T_{20}); or they consisted of repeated pairs of non-complementary bases ($(GT)_{10}$, $(CA)_{10}$). Since long guanine repeats are challenging to synthesize, we instead studied the guanine-rich ssDNAs $(GGGGA)_4$ and $(GGGGT)_4$.

Bulk TMDC powders were probe ultrasonicated in aqueous solutions containing 0.2 mg mL^{-1} of synthetic ssDNA. The ultrasonicated solutions were then centrifuged and

the resulting supernatants harvested. Figure 1b provides a photograph of the strongly colored and stable 2D TMDCs dispersions prepared using the common sequence T_{20}, which was an effective sequence for dispersing all four of the TMDCs. Optical absorbance spectroscopy of the dispersions confirmed successful exfoliation of the TMDCs revealing the characteristic excitonic transition peaks for the four compounds (Figure 1c).

The concentrations of the TMDCs dispersed in the synthetic ssDNAs were determined using inductively coupled plasma mass spectrometry (ICP-MS). $MoSe_2$ and WSe_2 yielded the highest concentration dispersions with loadings above 250 μg mL^{-1} obtained for optimal ssDNA sequences. The sulfur-containing MoS_2 and WS_2 displayed lower loadings, in general, with typical concentrations of 50 μg mL^{-1}. We further evaluated the stability of DNA wrapped TMDCs using zeta potential, with $MoSe_2$ and WSe_2 being the most stable with zeta potentials of -42.13 and -40.13 mV, respectively, whereas MoS_2 and WS_2 were the least stable with zeta potentials of -21.13 and -20.07, respectively (Figure A 3). We observed significant variations in the concentration of dispersed TMDCs depending on the sequence of ssDNA used and the composition of the TMDC. In general, the highest concentration dispersions were obtained for the T_{20} sequence whereas $(CA)_{10}$ was the weakest out of all sequences studied. Our study also revealed thymine and guanine showed better affinity towards all TMDCs compared to cytosine and adenosine. After determining that T_{20} and $MoSe_2$ provided the highest concentrations overall, we further evaluated the DNA coverage of $MoSe_2/T_{20}$ using Thermogravimetric analysis. These measurements indicated ~8% DNA coverage on the surface of the TMDCs. (Figure A2). The repeating dinucleotide sequence GT was also

tested with ssDNAs of different lengths, in particular 10-nt, 20-nt, and 40-nt lengths. We found that $(GT)_{10}$ provided the highest concentrations out of the three, and that MoS_2 ssDNA with $(GT)_5$ was unstable and aggregated within a few hours.

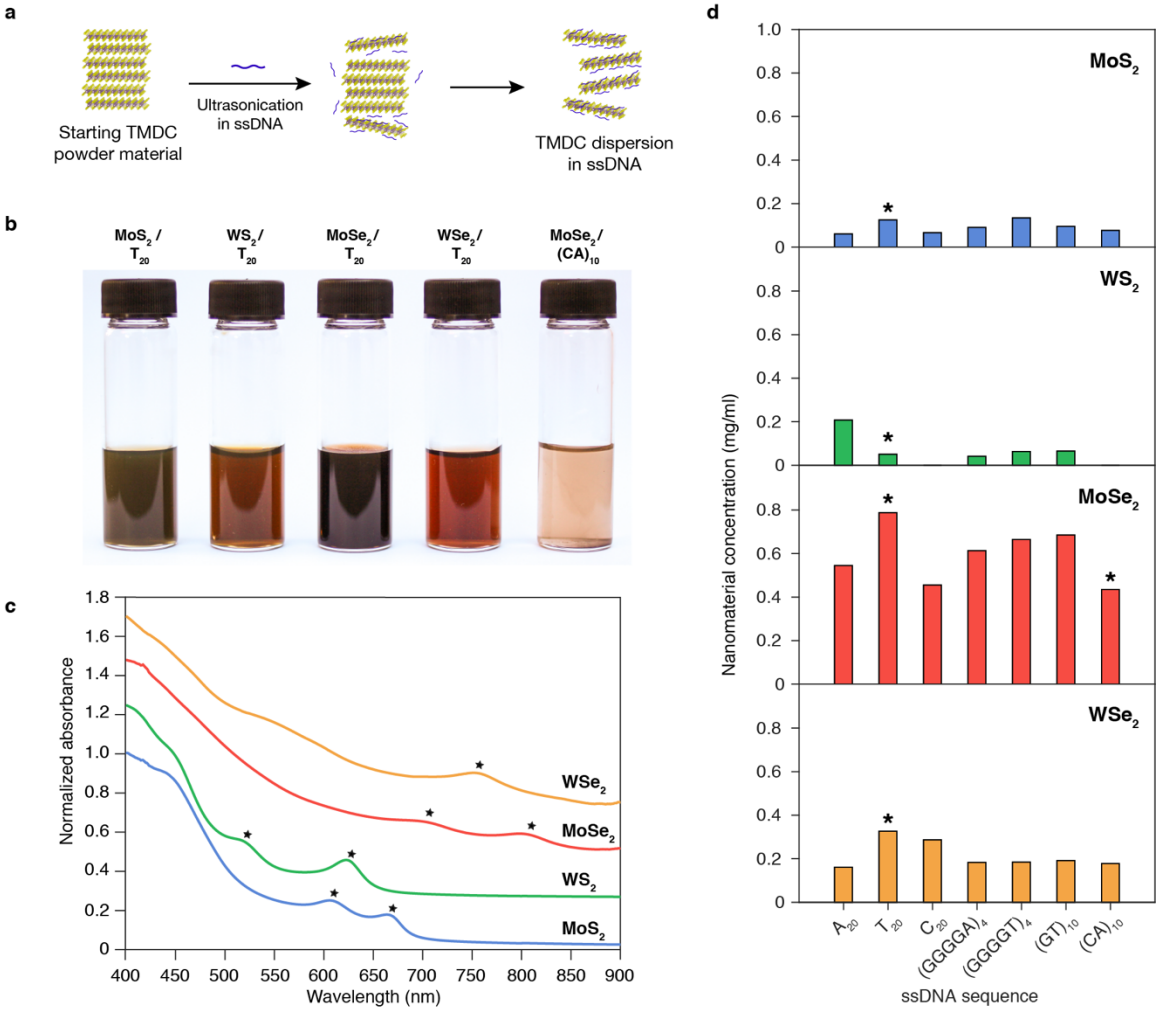

Figure 2.1: Exfoliation and encapsulation of 2D TMDCs using short ssDNAs. (a) Schematic illustrating exfoliation and coating of TMDCs in ssDNA (b) Picture of sample vials demonstrating stable dispersion of TMDCs in T_{20} DNA sequence. (c) UV-Vis-NIR spectroscopy of ssDNA-dispersed TMDCs demonstrating the 2H phase of the TMDCs after exfoliation. (d) Sequence dependence of ssDNAs used for dispersing TMDCs determined using ICP-MS.

The successful exfoliation of 2D TMDCs using low molecular weight ssDNA was further characterized using low and high-resolution transmission electron microscopy

(TEM and HRTEM) and atomic force microscopy (AFM) as shown in Figure 2. TEM imaging of the exfoliated TMDCs revealed their geometries as 2D nanosheets. The average lateral size of nanoflakes decreased in order from MoS_2, WS_2, $MoSe_2$, and WSe_2 (Figure 2a-d). MoS_2 yielded nanoflakes with lateral dimensions of approximately 80-100 nm, WS_2 and $MoSe_2$ from 60-70 nm, and WSe_2 less than 50 nm. AFM images of MoS_2 confirmed the presence of flakes with extended lateral dimensions with thicknesses of around 10 nm (Figure 2e). The WS_2 dispersion showed the second largest flakes with thicknesses less than 8 nm (Figure 2f), whereas $MoSe_2$ and WSe_2 exhibited the smallest flakes with thicknesses around 8 nm (Figure 2g) and 4 nm (Figure 2h). The measured thicknesses of TMDC flakes also include a uniform layer of ssDNA, which covers both sides of the TMDC flakes. The AFM and TEM data obtained correlate well with each other and both showed successful ssDNA-based exfoliation of TMDCs to produce few-layer TMDCs. We further studied the crystal structure of DNA dispersed TMDCs using HRTEM (Figure 2 a, b, c, d). These images showed that the TMDCs retains the expected hexagonal lattice structure of the pristine 2H phase of TMDCs following encapsulation by ssDNAs.

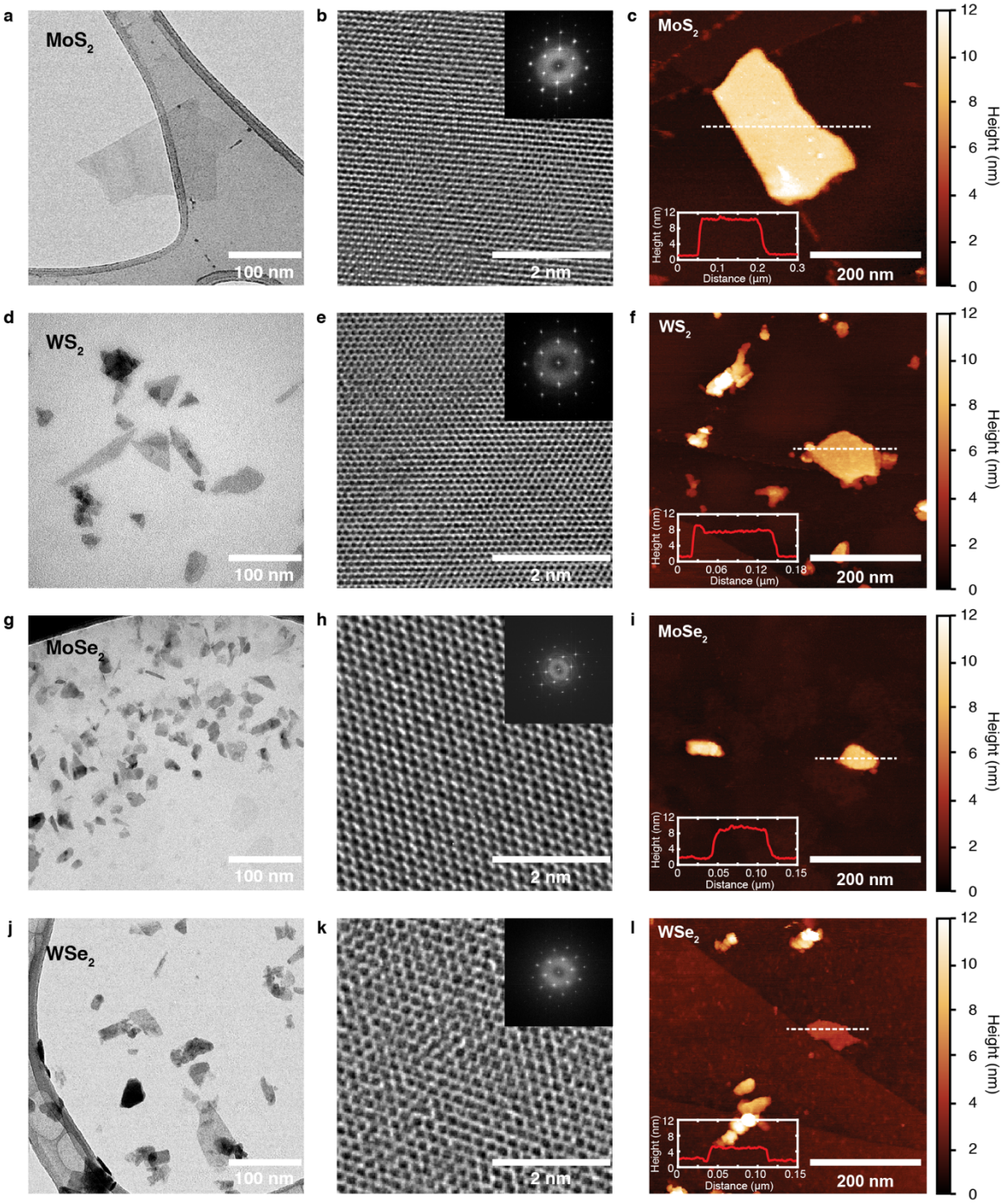

Figure 2.2: Microscopic characterization of ssDNA-dispersed TMDCs (a, d, g, i) Transmission electron microscopy (TEM) of ssDNA-dispersed TMDCs. TEM images demonstrate the nanosheet morphology of exfoliated TMDCs. (b, e, h, k) High resolution transmission electron microscopy (HRTEM) of ssDNA-dispersed TMDCs demonstrated hexagonal crystal structure of nanosheets. (c, f, i, l) Atomic force microscopy (AFM) demonstrates thin nanosheets with thickness around 6 to 8 nm, which further proves

successful DNA based exfoliation of TMDCs. AFM was done by Duo Li. HRTEM images were taken by Matt Gilliam.

3.2.2) Molecular dynamics simulations for representative ssDNA/2D-TMDC surface structures

We collaborated with the Ulissi group at Carnegie Mellon to perform molecular dynamics simulations to better understand the observed sequence-dependent encapsulation effects and the coating formed by ssDNA around the 2D TMDC's. Literature efforts had previously characterized the interaction energy and representative ssDNA conformations for single base pairs and short uniform sequences (G_6, T_6, A_6, C_6). For three of the sequences, $(GT)_{10}$, $(AC)_{10}$, and T_{20}, and two 50 nm X 50 nm 2d TMDC sheets (MoS_2 and $MoSe_2$), we performed long timescale molecular dynamics relaxations of approximately 100ns per system using the NAMD software and VMD for visualization. The force field, parameters, and explicit water model were chosen for consistency with previous studies, with final structures shown in Figure 3. We found that the T_{20} sequences consistently had the strongest interaction energy with the 2D TMDCs and formed extended flat sequences along the surface such that every base pair was in contact with the 2D TMDCs. The $(GT)_{10}$ sequences for both 2D TMDCs had similar structures for base pairs adsorbed to the surface driven by T base adsorption but had extended sequences off of the surface that could possible leader to thicker adsorption layers than the tightly bound T20 strands. The $(AC)_{10}$ strands tended to form stacked structures with A bases adsorbed to the surface, and C bases adsorbed on top of those. These results qualitatively explain the observed trends in ssDNA dispersion efficiency shown in Figure 1. We also calculated the interaction energy solely between the ssDNA

and the 2D TMDC sheets (i.e. ignoring water energetics), with T_{20} have uniformly the strongest interactions, as expected since every base pair was adsorbed. For all three base pairs the interaction energy was less strong for the $MoSe_2$ surfaces than for the MoS_2 surfaces, suggesting that interaction energy was inversely correlated with experimental solubility. Thermodynamic free energy adsorption energy calculations could describe these interactions more accurately, but the timescales associated with adsorption and desorption of such large molecules was prohibitively expensive.

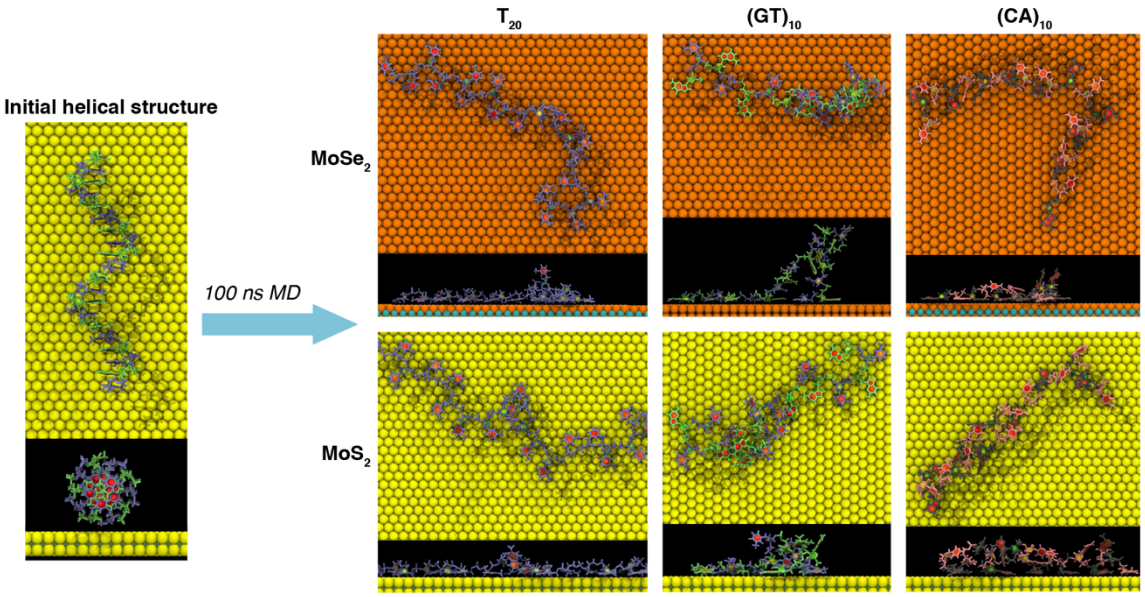

Figure 2.3: Molecular dynamics simulation demonstrating interactions of three different DNA sequences T_{20}, $(GT)_{10}$ and $(CA)_{10}$. Simulations were done by Dr. Zack Ulissi.

3.2.3) Antibacterial activity of $MoSe_2$/ssDNA

Since $MoSe_2$ dispersions provided the highest concentrations of 2D TMDCs overall and were coated with a biocompatible polymer, we chose to study the effect of $MoSe_2/T_{20}$ dispersions on human and bacterial cells. To assess their toxicity, $MoSe_2/T_{20}$ nanosheets were first added to cultures of the model HeLa human epithelial carcinoma

cell line. Concentrations of $MoSe_2/T_{20}$ ranging from 25 μg mL^{-1} to 250 μg mL^{-1} were applied to cultures for 24 hours and cell viability was determined using the colorimetric MTT assay. No significant toxicity was observed for $MoSe_2/T_{20}$, with 100% cell viability at all concentrations tested as shown in the Figure A 1.

Having confirmed the biocompatibility of $MoSe_2/T_{20}$ nanosheets, we next evaluated their effect on two representative strains of gram-negative and gram-positive bacteria, *E. coli* MG1655 and *Staphylococcus aureus subsp. Aureus* (ATCC 29213), respectively. For determination of antibacterial activity, logarithmic-phase bacteria at a concentration of 10^7 cell-forming units per mL (CFU mL^{-1}) were treated with $MoSe_2/T_{20}$ dispersions at different concentrations for 4 hours. Microdilutions of the treated bacteria were then applied to agar and incubated overnight for colony counting the next day. The $MoSe_2/T_{20}$ dispersions displayed exceptional antibacterial activity against both species of bacteria. We observed 100% elimination of *E. coli* at a concentration of 150 μg mL^{-1} $MoSe_2/T_{20}$ (Figure 4a). For *S. aureus*, $MoSe_2/T_{20}$ displayed more potent activity, completely eliminating the gram-positive strain at a concentration of only 75 μg mL^{-1} (Figure 4b).

Recently, the antibacterial activity of carbon-based 2D materials has drawn wide attention.[110,158-161] In a recent report, Liu et al. carried out a comparative study of antibacterial activities of four different graphene-based materials (graphite, graphite oxide, graphene oxide and reduced graphene oxide), with graphene oxide (GO) showing the strongest bactericidal effect.[160] Thus, we compared the antibacterial activity GO, double stranded DNA encapsulated Graphene (Graphene/dsDNA) with respect to $MoSe_2/T_{20}$ on wild-type gram-negative *E. coli* MG1655 and gram-positive *S. aureus*

strain under the same experimental conditions. GO and $MoSe_2/T_{20}$ were incubated with *E. coli* MG1655 and *S. aureus* for 4 hours, plated on agar, and cell viability was determined by colony counting. For *S. aureus*, 75 μg ml^{-1} of $MoSe_2/T_{20}$ showed 3-log higher killing compared to GO, whereas 6-log higher activity was observed compared to graphene/dsDNA. For *E. coli*, at 150 μg ml^{-1} of $MoSe_2/T_{20}$ showed 3-log higher antibacterial killing compared to graphene oxide and 3-log higher killing compared to graphene/dsDNA (Figure 2.4 a and b). Furthermore, $MoSe_2/T_{20}$ exhibits higher antibacterial killing at all the tested concentrations compared to GO and graphene/dsDNA. The higher antibacterial efficiency of $MoSe_2/T_{20}$ compared to GO and Graphene/dsDNA, can be attributed to the bulkiness of systems as a key factor towards difference in antibacterial activity. The higher size of dsDNA on graphene inhibits its interactions with negatively charged bacteria. In case of GO, the presence of negatively charged oxygen group and higher size nanosheets compared to $MoSe_2/T_{20}$, led to lower antibacterial activity of GO compared to $MoSe_2/T_{20}$.

To determine if the short synthetic DNA coating contributed to the enhanced antibacterial activity of the $MoSe_2$ nanosheets, we then carried out comparative studies with $MoSe_2$ encapsulated by three biocompatible polymers: T_{20} ssDNA, long genomic DNA purified from salmon testes, and the block copolymer Pluronic F77. A recent report by Bang et al. demonstrated that WSe_2 suspended using long genomic DNA had two-fold higher antibacterial activity than GO[147]. Pluronic F77 has been widely used for preparing biocompatible dispersions of 2D nanosheets[162] and consists of a hydrophobic polypropylene oxide block flanked by two hydrophilic polyethylene oxide regions. In our experiments, we found that $MoSe_2/T_{20}$ showed significantly stronger bactericidal

properties compared to $MoSe_2$/long genomic DNA and $MoSe_2$/F77 for nearly all the concentrations tested and provided stronger enhancements as the concentration increased (Figure 2.4 c and d). At 150 μg mL^{-1} concentrations, $MoSe_2/T_{20}$ completely eradicated *E. coli*, which corresponded to the elimination of all 10^7 cells treated, while the activity of $MoSe_2$/long genomic DNA and $MoSe_2$/F77 was 2.2 and 3.2 logs weaker, respectively. Also, $MoSe_2/T_{20}$ showed 4 and 3 logs higher killing towards *S. aureus* when compared with $MoSe_2$/long genomic DNA and $MoSe_2$/F77.The variation in antibacterial activity with changes in polymer coating on $MoSe_2$ can be attributed to the fact that, with increases in the bulkiness of polymer coating on the nanomaterial surface, there is reduction in the interactions of nanosheet edges with the bacterial cell membrane. The Pluronic F77 employs bulky polyethylene oxide blocks to suspend the $MoSe_2$ in the aqueous environment; however, these polymer blocks discourage strong interactions with the bacterial cell wall. For the long genomic DNA, the use of long DNA sequences prevents the formation of a conformal ssDNA coating around the $MoSe_2$ and thereby increases the effective thickness of the nanosheets. In contrast, the short length of the T_{20} sequence enables the ssDNA to effectively coat and spread out along the $MoSe_2$ surface and yields an ultrathin material to promote piercing of the bacterial cell wall. Furthermore, simple thermodynamic arguments suggest that molecules with proportionally larger length and adsorption energies will, at the same base pair concentration in solution, result in higher surface packing densities than for shorter molecules with smaller adsorption energies since the free energy is an exponential function, and should thus yield thicker nanosheets for longer DNA lengths.

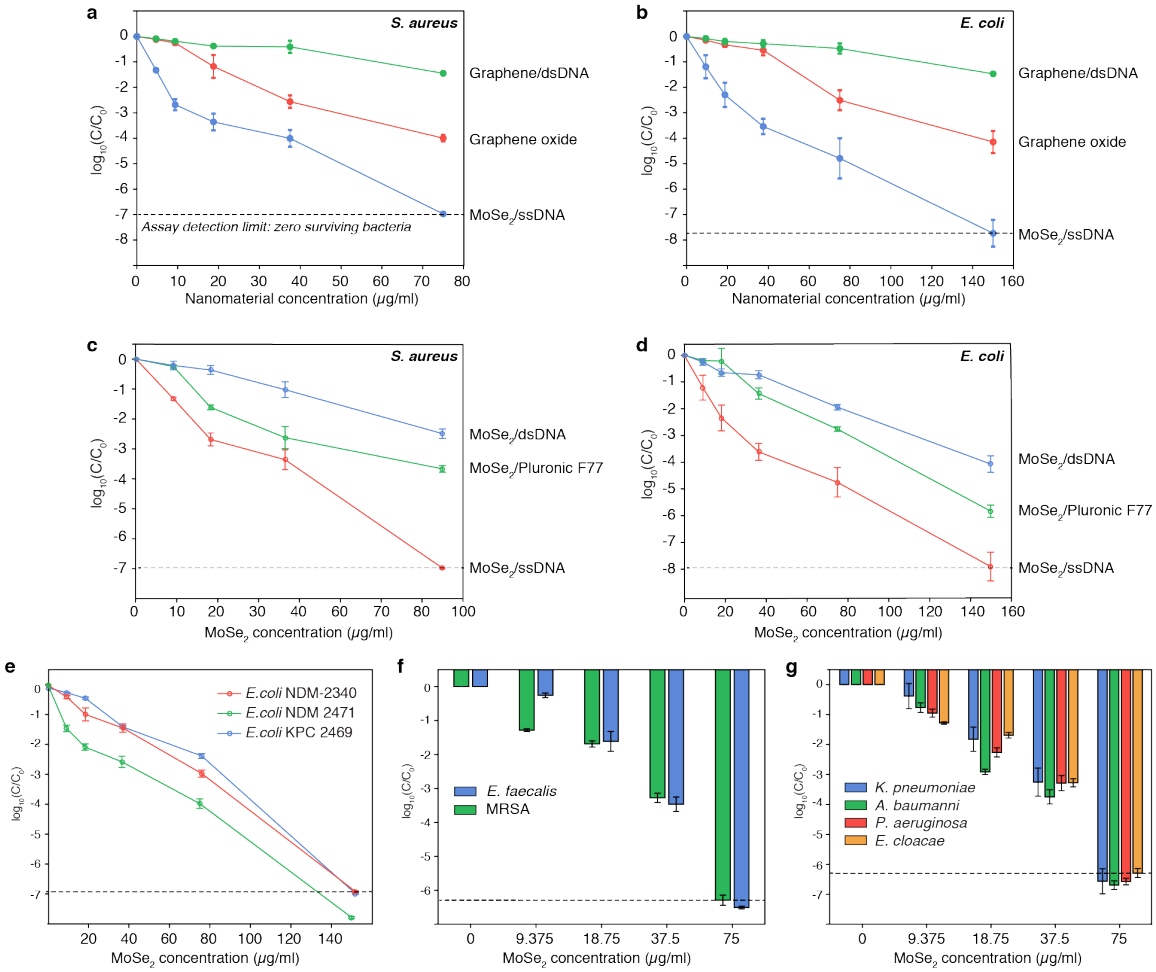

Figure 2.4: Antibacterial activity of ssDNA-dispersed TMDCs (a, b) Comparison of antibacterial activity of $MoSe_2/T_{20}$ with respect to carbon-based materials, graphene oxide and double stranded DNA dispersed graphene on two gram-positive *S. aureus* and gram-negative *E. coli*. (c, d) Comparison of antibacterial activity of $MoSe_2/T_{20}$ with respect to two different dispersing agents, double stranded DNA and Pluronic- F77. (e) Antibacterial activity of $MoSe_2/T_{20}$ on multidrug resistant gram-negative *E. coli* strains NDM 2340, NDM 2471 and KPC 2469. (f) Antibacterial activity of $MoSe_2/T_{20}$ against gram-positive 'ESKAPE' strains. (g) Antibacterial activity of $MoSe_2/T_{20}$ against gram-negative 'ESKAPE' strains.

3.2.4) Antibacterial Studies Against MDR Bacteria

The continuing emergence of nosocomial infections by bacteria with broad-spectrum resistance to antibiotics in hospitals and clinics requires novel antibacterial strategies. We sought to determine if the $MoSe_2/T_{20}$ dispersions retained their exceptional

bactericidal activity against several multidrug resistant strains. We first evaluated three strains of multi-drug resistant (MDR) *E. coli* carrying resistance to carbapenems, a class of antibiotic agents often used to combat drug-resistant infections. *E. coli* NDM 2469 and *E. coli* NDM 2471 strains both carry the New Delhi metallo-β-lactamase (NDM), a recently identified carbapanemase, while *E. coli* KPC 2340 carries the *Klebsiella pneumoniae* carbapenemase (KPC). All three strains exhibited broad-spectrum resistance to multiple families of antibiotics. Antibiotic resistance tests conducted by ATCC on the NDM 2469 and NDM 2471 strains indicated that these strains were resistant to 33 and 32 out of 35 antibiotics tested. Studies by ATCC on *E. coli* KPC 2340 indicated that it was resistant to 30 out of the 34 antibiotics evaluated. The three MDR *E. coli* strains were exposed to different concentrations of $MoSe_2/T_{20}$ over 4 hours and surviving cells counted after plating microdiluted samples. No viable *E. coli* bacteria were observed after treatment with 150 μg ml^{-1} of $MoSe_2/T_{20}$, and the killing efficiency increased with increasing concentration (Figure 2.4e). At lower concentrations of $MoSe_2/T_{20}$, higher killing efficiency was observed for NDM *E. coli* strains compared to KPC *E. coli* strains, as shown in Figure 4. At 100 μg ml^{-1}, $MoSe_2/T_{20}$ showed 99.98% and 99.8% cell killing for NDM strains, whereas 99.5% cell killing was observed for KPC strains.

After successful eradication of MDR *E. coli*, we further evaluated antibacterial efficiency of $MoSe_2/T_{20}$ on nosocomial-based MDR and clinical isolate 'ESKAPE' strains. We first evaluated efficiency of $MoSe_2/T_{20}$ on two well-known gram-positive clinical strains, Methicillin- resistant Staphylococcus aureus (MRSA) and vancomycin resistant *Enterococcus faecium* (VRE). MRSA, which is responsible for 25 to 50% of nosocomial infections expresses the mecA gene, which provides resistance to a broad

spectrum of ß-lactam antibiotics, whereas VRE, which causes nosocomial urinary tract infections, is resistant to all ß-lactam antibiotics and last resort antibiotics, vancomycin. After 4 hours of treatment, 75 μg ml^{-1} $MoSe_2/T_{20}$ successfully eliminated VRE and MRSA by 7 logs (Figure 2.4 f and g). We further extended our study, and checked the efficiency on gram-negative ESKAPE' strains, which includes *Klebsiella pneumoniae*, Acinetobacter baumannii, *Pseudomonas aeruginosa* and *Enterobacter*. Antibiotic resistance conducted by ATCC on *Pseudomonas aeruginosa* and *Acinetobacter baumanii* strains, demonstrated resistance to 15 and 31 different classes of antibiotics whereas *Enterobacter* and *Klebsiella pneumoniae* demonstrated resistance to all tested 36 different classes of antibiotics. After 4 hours of treatment, 75 μg ml^{-1} of $MoSe_2/T_{20}$ successfully eradicated all the four gram-negative MDR strains. We successfully eliminated all the 'ESKAPE' bacterial strains at concentration as low as 75 μg ml^{-1}. The species-independent antibacterial mechanism of $MoSe_2/T_{20}$ eliminates the traditional problems of one bug-one drug approach and showed broad spectrum nature of designed systems.

3.2.5) Mechanistic study of antibacterial activity of $MoSe_2$/ssDNA

We carried out SEM and TEM studies to investigate the effect of $MoSe_2/T_{20}$ interactions on the cell morphology of gram-positive MRSA and gram-negative *A. baumannii* cells. SEM images of untreated MRSA and *A. baumannii* samples showed no significant morphological changes (Figure 5a and Figure 5g), and TEM images of untreated MRSA and *A. baumannii* showed an intact cytoplasm (Figure 5d-and 5g-). SEM images of MRSA and *A. baumannii* treated at 0.5x MBC (37.5 μg ml^{-1}) of

$MoSe_2/T_{20}$ showed formation of small blob-like structures (Figure 5b), which further increased in numbers at 1x MBC (75μg ml^{-1}) (Figure 5c) The formation of small blobs on cell membrane can be attributed to interactions with the nanomaterial sharp edges, which cause breakdown of the cell membrane. TEM images of MRSA and *A. baumannii* further showed TMDC flakes encapsulating and penetrating the cell membranes of bacteria (Figure 5e, 5f and 5k, 5i). For both *A. baumannii* and MRSA, TEM images demonstrated the presence of void spaces in cytoplasm after treatment with 0.5x MBC, which further increased with increasing nanomaterials concentrations to 1x MBC. The formation of small groove-like structures in the cell membrane, leads to disturbance in the cytoplasm and finally leakage of protein and other cell components out. With increasing nanomaterial concentration, the density of void spaces increases, indicating stronger interactions with cell surfaces. The nature of damage to cellular membrane and cytoplasm is identical for both gram-positive and gram-negative bacteria, which further supports the broad-spectrum antibacterial nature of nanomaterials.

The microscopic analysis of TMDC-treated bacteria showed void spaces inside the cytoplasm of bacteria, which can be attributed to the fact that the TMDC flakes caused severe damage to the peptidoglycan of the plasma membranes. The damaged membrane in turn fails to hold the turgor pressure of the cytoplasm and leads to leakage of the cytoplasm. The observed effect is consistent with other reports of the antibacterial mechanism of carbon-based nanomaterials, which act as “nanoknives” that can interfere with membrane integrity as a result of their atomically sharp graphene edges.[143,163,164] The theoretical and experimental studies of antibacterial mechanisms of graphene-based nanomaterials have shown that they act like blades penetrating through bacterial cell

membranes, causing physical damage, and leading to leakage of cytoplasm. Based on previous studies, we hypothesize that the presence of DNA on TMDC surfaces increases their hydrophilicity, which encourages them to make contact interaction with the outer surfaces of the bacteria.[147] Once in close proximity, the sharp edges of the $MoSe_2/T_{20}$, which are more readily exposed as a result of the conformal ssDNA coating, are better able to interfere with the membrane to trigger cell death.

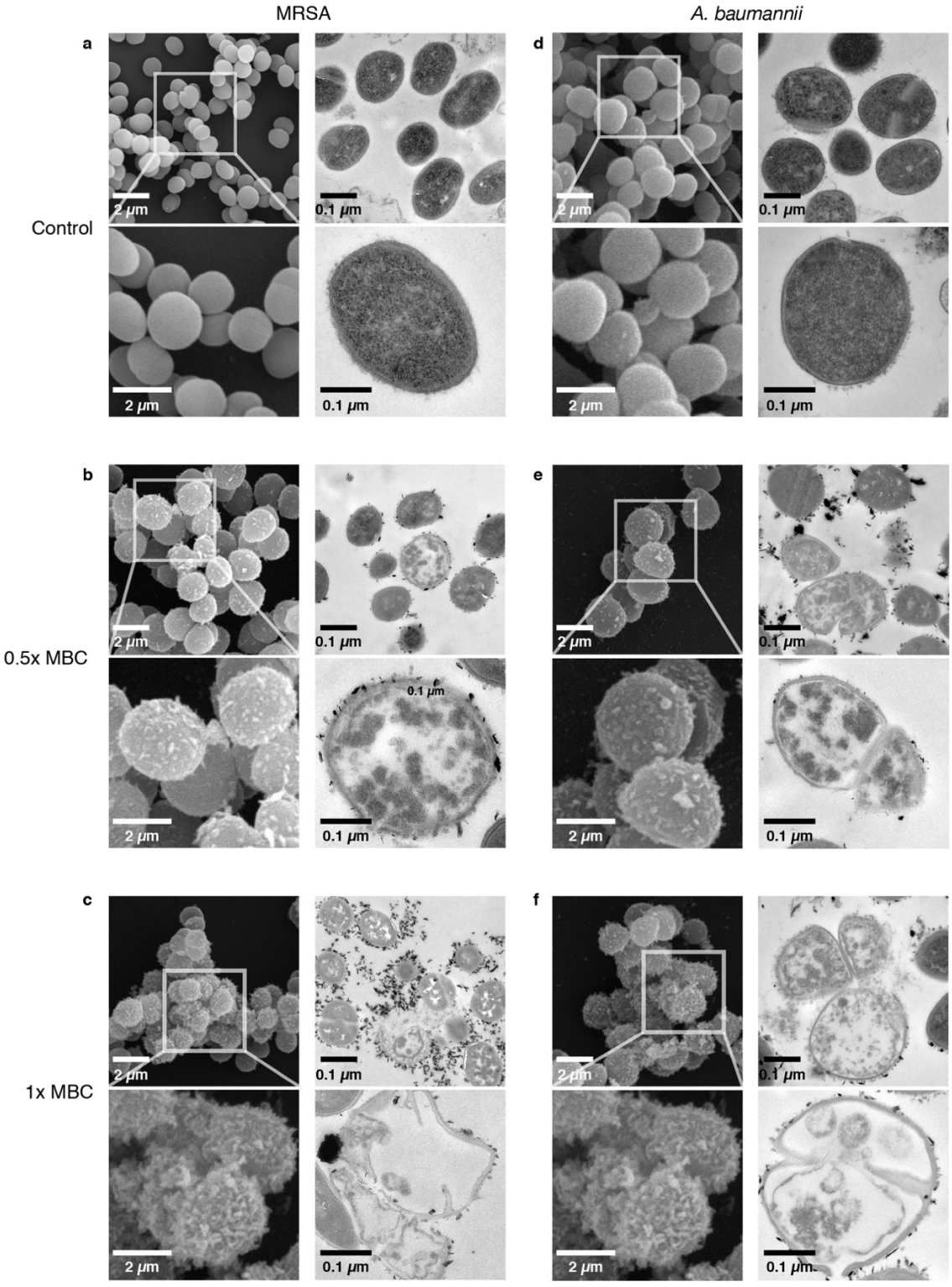

Figure 2.5: Microscopic evaluation of morphology of bacteria before and after treatment with $MoSe_2/T_{20}$ (a, d) SEM and TEM imaging of MRSA and *A. baumannii* before treatment with nanomaterials. SEM images of MRSA and *A. baumannii* demonstrate

intact morphology of bacterial cell. Also, TEM reveals intact cytoplasm inside bacterial cell membrane. (b, e) SEM and TEM images of bacteria after treatment with 0.5 x MBC $MoSe_2/T_{20.}$ The SEM images demonstrate the appearance of small vacuole-like structure on the bacterial membrane due to interactions with sharp edges of bacteria. TEM demonstrates disturbance in cytoplasm and small empty void spaces inside bacteria after interactions with sharp edges of nanomaterials. (c, f) SEM images demonstrate damaged bacterial membrane. TEM images demonstrates creation of void spaces in bacterial cytoplasm's after interactions with $MoSe_2/T_{20.}$

We further evaluated the antibacterial killing mechanism $MoSe_2/T_{20}$ using the well-known probe 3,3'-Diethyloxacarbocyanine Iodide ($DiOC_2$). $DiOC_2$ is a cyanine dye, which permeates the cell membrane exhibiting green fluorescence, and undergoes aggregation in the polarized cell leading to fluorescence shifting from green to red. We evaluated the change in membrane potential after nanomaterial interactions on two different strains of bacteria, gram-positive *S. aureus* and gram-negative *E. coli.* For the membrane potential assay, we treated the bacteria at four different concentrations, 1x MBC, 0.5x MBC, 0.25x MBC and 0.125x MBC. The carbonyl cyanide 3-chlorophenylhydrazone, a well-known membrane ionophore was used as a positive control. With increasing nanomaterial concentration, the fluorescence shifts towards the green channel, which is further evident from lowering of the red/green fluorescence intensity ratio. The change in fluorescence intensity ratio indicates that interaction of the bacterial cell with nanomaterials triggers depolarization of cell.

After measuring membrane potentials, we further studied the induction of oxidative stress, using the fluorogenic probe CellROX. The oxidative stress induced after nanomaterial interactions was studied for both gram-positive *S. aureus* and gram-negative *E. coli* at three different concentrations, 1x MBC, 0.5x MBC and 0.25x MBC. At 1xMBC, $MoSe_2/T_{20}$ induces 42-fold and 16-fold higher oxidative stress for *S. aureus*

and *E. coli* with respect to untreated samples (Figure 4.6 c and 4.6 d). Furthermore, oxidative stress of bacterial cell decreases with nanomaterial concentration. The addition of antioxidant N-acetylcysteine at 1x MBC of nanomaterial concentrations reduces the oxidative stress by 19-fold and 6-fold respectively, which further demonstrates the generation of cellular oxidative stress after interactions with nanomaterials.

After determination of membrane potential and oxidative stress generation in bacterial cell, we further evaluated the impact of this stress on DNA damage. Damage to DNA generally triggers programmed cell death. There are two well-known pathways for programmed cell death, RecA and mazEF pathways. The mazEF pathways refers to toxin-antitoxin module of bacteria. mazF genes generally encode for a toxic endoribonuclease protein MazF, which quickly degrades mRNA whereas mazE genes lead to secretion of the antitoxin mazE, which neutralizes the effect of MazF. Under stressful conditions, MazE is quickly degraded by ClpPA serine protease, which leads to the presence of higher toxic protein and in turn cell death. The SOS response pathway refers to inducible pathways that are responsible for DNA repair.[165] There are two key proteins which is responsible for this SOS response pathways, repressor LexA and inducer RecA. In absence of DNA damage, LexA dimer binds to palindromic sequence of the DNA SOS box, inhibiting expression of RecA genes. Under DNA damage, RecA pathway is activated leading to self-cleavage of LexA and activation of RecA pathways, which lead to cell death.[166]

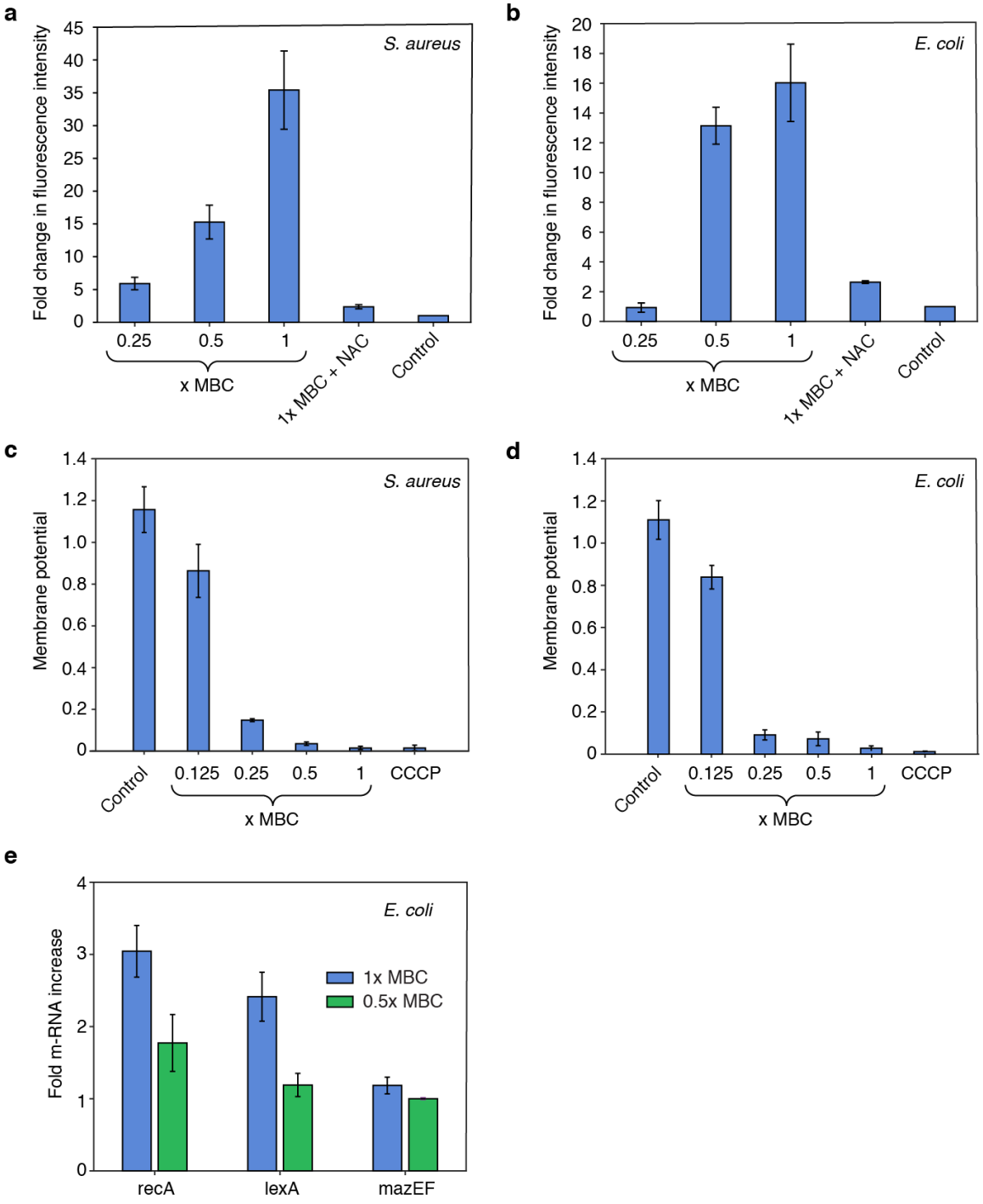

Figure 2.6: Mechanistic analysis of antibacterial action of $MoSe_2/T_{20}$ (a, b) Generation of oxidative stress after interactions with $MoSe_2/T_{20}$. (c, d) Change in membrane potential after interactions with $MoSe_2/T_{20}$ (e) Fold change in mRNA expression after interactions with $MoSe_2/T_{20}$

We studied the programmed cell death pathways of *E. coli* after interaction with 0.5x MBC and 1x MBC of $MoSe_2/T_{20}$. After interactions of nanomaterials with *E. coli*, 0.5x MBC and 1x MBC showed 2-fold and 3-fold increase in mRNA expression of RecA levels, whereas there is 1-fold increase in mazEF levels for both the tested concentrations. These studies clearly demonstrate involvement of two pathways towards the cell death after interaction with $MoSe_2/T_{20}$.

3.2.6) Proposed antibacterial action of $MoSe_2$/T20

The antibacterial activity of $MoSe_2$-ssDNA can be summarized as a three-step process. First, negatively charged DNA on the surface of 2D $MoSe_2$ selectively increases the tendency of the bacterial cells to undergo interactions with hydrophobic sharp edges of nanomaterials. The sharp edge of nanomaterials undergoes insertion inside bacterial cell membrane, leading to rupture of the cell membrane. The rupture to cellular membrane in turn induces polarization of cell membrane potential. The alteration of membrane potential, in turn induces generation of cellular oxidative stress, causing damage to DNA, and finally programmed cell death. Thus, damage to cell membranes is a key factor to initiating the process.

Our study showed $MoSe_2$/ssDNA demonstrated stronger bactericidal activity towards gram-positive strains than gram-negative strains at all the concentrations we tested. This trend correlates with previously obtained antibacterial activity for carbon-based nanomaterials.[34–39] The difference in killing efficiency between gram-negative and gram-positive bacterial strains can be explained by their different outer structures. Gram-

negative bacteria have outer membranes, which are made up of a lipid bilayer and thin peptidoglycan layer, whereas gram-positive bacteria are made up of a thick peptidoglycan layer and no outer membrane.[167] The outer membrane of gram negative bacteria is made up of negatively charged glucosamine disaccharides called lipopolysaccharides, whereas gram positive bacteria contain thicker peptidoglycan layer with long anionic polymer called teichoic acids threading out from the peptidoglycan layer. The presence of more negatively charged surfaces on gram-negative bacteria provides higher resistance to negatively charged nanomaterials. Furthermore, the absence of outer membrane on gram-positive bacteria makes it more susceptible to membrane damage by direct interaction with the sharp edges of nanomaterial flakes. The absence of lipopolysaccharides coupled with the lack of outer membrane on the surfaces of gram-positive bacteria makes them more susceptible to membrane damage by sharp edges of negatively charged nanomaterials.

3.3) Conclusion

Using short synthetic ssDNA sequences, we have successfully prepared stable dispersions of 2D TMDCs in aqueous solutions and demonstrated their remarkable antibacterial performance. Exfoliation of few-layer TMDC nanosheets was confirmed using optical absorbance and TEM and AFM imaging. Concentration measurements using ICP-MS identified $MoSe_2$ as the TMDC most effectively dispersed using synthetic ssDNA. Also, our experimental and computational study showed DNA sequence dependence towards dispersing TMDCs, with T_{20} have the strongest affinity towards dispersing TMDCs. Owing to the biocompatibility of the ssDNA coating, we studied the effect of the $MoSe_2$ nanosheets encapsulated by T_{20} ssDNA against human and bacterial

cells. While no toxicity was observed against a human cell line, we observed potent bactericidal activity for the $MoSe_2/T_{20}$ nanosheets against multiple strains of gram-negative and gram-positive bacteria. In side by side comparisons, the bactericidal efficiency of $MoSe_2/T_{20}$ nanosheets exceeded that of the most widely studied two-dimensional antibacterial material graphene oxide by more than 1000-fold. Furthermore, it exceeded the reported activity of $Ti_3C_2T_x$, a recently developed two-dimensional antibacterial[139], by more than 100-fold and 10-fold against gram-positive and gram-negative bacteria, respectively. $MoSe_2$ prepared using long single-stranded DNAs or with Pluronic F77 coating were much less effective at eliminating the bacteria demonstrating the critical importance of an optimized, conformal ssDNA coating for enhanced antibacterial activity. Studies of both *E. coli* and MRSA cells treated with the $MoSe_2/T_{20}$ revealed that the nanosheets aggressively interact with the cell walls of the bacteria, acting as nanoknives that create holes and folds in the membrane to induce cell death. Furthermore, it successfully eradicated all the clinical isolates of 'ESKAPE' strains, which opened up new windows for the development of next generation broad-spectrum antibacterial material replacing the tradition strategy of combating these 'Superbugs'

These results not only demonstrate that 2D $MoSe_2$/ssDNA can exhibit antibiotic-like activity against multidrug resistant bacteria, but also emphasize the importance of employing optimized encapsulation agents to enhance the effectiveness of two-dimensional nanoknives. In particular, the use of a conformal ssDNA coating suggests that an array of other biocompatible biomolecules can be interfaced with intrinsically antimicrobial 2D nanomaterials to generate effective new tools to combat the growing threat of antimicrobial drug resistance.

3.4) Methods

3.4.1) DNA dispersion of nanomaterial

In a typical experiment, TMDC powder was added to a 5-mL aqueous solution containing 1 mg of single-stranded DNA (Integrated DNA Technologies). $MoSe_2$ and WSe_2 bulk powder (Sigma Aldrich) at a mass of 200 mg was used for each dispersion, while a lower mass of 100 mg of MoS_2 and WS_2 (Sigma Aldrich) led to higher concentration dispersions for these compounds. The resulting mixture was ultrasonicated with a 13-mm tip f at a power level of 12 W for 2 hours. (Branson Digital Sonifier 450D) After ultrasonication, sample was centrifuged at 5000 g for 5 minutes followed by 21000 g for 1 minute to remove the unexfoliated material. The supernatant of ssDNA-encapsulated TMDC nanosheets was then carefully decanted for study.

3.4.2) TEM analysis of DNA dispersed solution

The sample was prepared using drop casting method. Briefly, 6 µl of dispersed solution was drop casted onto holey carbon copper grids and imaged using a Phillips CM-12 TEM.

3.4.3) AFM analysis of DNA dispersed solution

The substrate (SiO_2/Si) were cleaned in sequential ultrasonic baths of acetone and IPA for 5 minutes, respectively. Then the dispersions of nanomaterials were spin-coated onto the substrate at 2500 rpm. The spin coated samples were annealed in vacuum with 200 sccm of ultrahigh pure argon gas flow at 300 °C for 3 hours to remove the solvent

residue. AFM images were taken using a Multimode V system (Bruker inc.) in ScanAsyst mode with ScanAsyst-Air tips and flattening was processed using Gwyddion

3.4.4) Antibacterial studies

The antibacterial activity of $MoSe_2$-ssDNA was studied using wild type *E. coli* strain MG1655 (ATCC -700926), three *E. coli* MDR strains (ATCC- BAA-2340, ATCC-BAA-2469 and ATCC-BAA-2471), *Staphylococcus aureus* (ATCC-29213), *Methicillin resistant Staphylococcus aureus* (ATCC-BAA 1720), *Pseudomonas aeruginosa* (ATCC-BAA 2113), *Klebsiella pneumoniae* (ATCC- BAA 2342), *Vancomycin resistant Enterococcus faecium* (ATCC-51299), *Acinetobacter baumannii* (ATCC- BAA 1797) and Enterobacter cloacae (ATCC- BAA 2468). LB medium (Sigma Aldrich) and LB agar (Sigma Aldrich) were used to grow *E. coli* strain MG1655. TSB broth (Sigma Aldrich) and TSB agar (Sigma Aldrich) were used to grow *Staphylococcus aureus*, *Methicillin resistant Staphylococcus aureus*, *Pseudomonas aeruginosa* and *Acinetobacter baumannii* whereas *Vancomycin-resistant Enterococcus faecium* were grown in BHB broth (Sigma Aldrich) and BHB agar (Sigma Aldrich) in the presence of 4 μg/ml of vancomycin. MHB broth (Sigma Aldrich) and MHB agar (Sigma Aldrich) was used to grow *Klebsiella pneumoniae*. Single colonies were picked up from the agar plates and allowed to grow overnight in 5 ml of culture medium. Then, the sample was diluted 100 times in medium and allowed to grow until it reached 0.3 OD. Cultures were centrifuged at 2000 rpm for 10 minutes, and pellets were washed three times in phosphate buffer saline (PBS, Sigma Aldrich) to remove medium constituents. Finally, cell pellets were redispersed in autoclaved water and diluted to a cell concentration of 10^7 CFU/ml. Bacteria at

concentrations of 10^7 CFU/ml were incubated with different concentrations of nanomaterials (40-150 μg/ml) for 4 hours. After incubation, bacteria were plated in agar plates using serial dilution method and allowed to grow overnight.

3.4.5) SEM and TEM analysis of bacteria

For TEM, samples were initially fixed with 2.5% glutaraldehyde overnight at 4 °C and pelleted into 0.8% aggregate to form dense cell aggregates. The cell pellet was treated for 2 hours with 1% Osmium tetraoxide in DPBS, followed by washing with deionized water and en-block stained overnight at 4 °C with aqueous 0.5% uranyl acetate. The cell pellet was dehydrated in series in a graded acetone series. The sample was sectioned and post stained using 2% uranyl acetate in 50% ethanol solution and Sato's lead citrate for 3-4 minutes. Images were acquired using Phillips CM-12 TEM operated at 80 kV using a Gatan model 791 side-mount CCD camera

For SEM, samples were initially fixed using 2.5% glutaraldehyde at 4 °C, followed by washing with DPBS. The samples were postfixed with 1% osmium tetraoxide in DPBS, followed by washing with deionized water and dehydration in graded ethanol series. The samples were critically dried, sputtered coated with gold-palladium and images was captured using JEOL JSM6300 SEM operated at 15 kV

3.4.6) Membrane potential assay

The membrane potential of bacteria was determined following the manufacturer's protocol, Baclight membrane potential kit (Invitrogen). Briefly, bacteria were inoculated to mid-log phase and diluted to the order of 10^6 CFU/ml in autoclaved water. The bacteria were treated with different concentrations of $MoSe_2$-ssDNA (1x MBC, 0.5x

MBC, 0.25 x MBC and 0.125 x MBC) for 4 hours. A fully depolarized sample was prepared on addition of 5 mM proton ionophore, carbonyl cyanide 3-chlorophenylhydrazone (CCCP). After treatment, samples were incubated with 30 mM $DiOC_2$ for 1 hour. Membrane potential was determined using Stratedigm S1300Exi cell analyzer equipped with A600 high-throughput autosampler, as ratio of cell exhibiting red fluorescence to cell exhibiting green fluorescence. Cell populations were gated based on untreated (polarized) and CCCP treated (depolarized) one**.**

3.4.7) ROS production assay

E. coli and *S. aureus* was inoculated in LB and TSB medium to mid-log phase and diluted to the order of 10^6 in autoclaved water. The samples were treated with different concentration of $MoSe_2$-ssDNA (1x MBC, 0.5x MBC, 0.25x MBC) for 4 hours. After incubations, cells were stained using CellROX orange reagent (Invitrogen) following manufacturer's protocol. Briefly, samples were stained with 750 mM of CellROX orange reagent, and samples was analyzed using Stratedigm S1300Exi cell analyzer equipped with A600 high-throughput autosampler and mCherry fluorescence output was used to determine the oxidative stress of the cells.

3.4.8) RNA extraction and reverse transcription polymerase chain reaction (RT-PCR) for determination of programmed cell death

The programmed cell death pathway of bacteria was determined using m-RNA expression level following the reported protocol. [168] Briefly, bacteria were treated with three different concentrations of nanomaterials, 1x MBC, 0.5x MBC and 0.25 x MBC. After incubation, the bacteria were centrifuged, and RNA was extracted using

manufactures protocol (Qiagen). After extraction of RNA, reverse transcription was performed following manufactures protocol (Qiagen Reverse Transcription kit). After extraction of cDNA, RT-PCR was performed using manufactures protocol iTaq Universal SYBR Green Supermix (Bio-Rad). The primer used for the RT-PCR: recA (*fwd*) AGATCCTCTACGGCGAAGGT, (*rev*) CCTGCTTTCTCGATCAGCTT; lexA (*fwd)* GACTTGCTGGCAGTGCATAA, (*rev*) TCAGGCGCTTAACGGTAACT; MazEF-1 (*fwd*) CTTCGTTGCTCCTCTTGC, (*rev*) CGTTGGGGAAATTCACCG; 16SrRNA (*fwd*) TGTAGCGGTGAAATGCGTAGA, (*rev*) CACCTGAGCGTCAGTCTTCGT. A positive control of genomic DNA and no-reverse transcription were included as controls. Cycling was performed in Applied Biosystems ViiA 7 Real-Time PCR systems.

Chapter 4

Eradication of multidrug-resistant bacteria using two-dimensional material based nanohybrid structures.

4.1) Introduction

The increasing pervasiveness of infections caused by multidrug-resistant (MDR) bacteria is a major global health issue, which has been further exacerbated by the lack of effective new antibiotics introduced in last 40 years[169,170]. Drug-resistant bacteria lead to significant morbidity and mortality, with 1.7 million people acquiring MDR infections in United States alone and almost 98,987 deaths each year, which is more than the deaths annually from prostate cancer, breast cancer, heart failure and diabetes.[152,171-173] The increasing prevalence of infections from drug-resistant bacteria in hospital settings and decreasing effectiveness of antibiotic treatments, severely affect multiple fields of medicine, including surgery, premature infant care, cancer chemotherapy and transplantation medicine[174]. The traditional strategy for combating these superbugs involves the development of new antibiotics, but only two classes of antibiotics have been introduced into the clinics over the past two decades and neither of these were effective against a broad spectrum of bacteria.[175] Furthermore, the mutation-prone replication machinery of bacteria lead to significant development of resistance to any introduced therapy that solely relies on bacteriostatic/bactericidal mechanisms, and clinically significant resistance can appear within few months of the introduction of a new antibiotics[176-178]. For example, Ceftaroline was introduced in clinics in 2010 and, less than a year later, the emergence of resistance was observed in patients with *Neisseria*

gonorrhoeae, *Enterobacter* and *Staphylococcus aureus* infections[179]. The dearth of proper antibiotics discovery and rapid resistance development demands the development of alternative strategies for combatting bacterial infections.

Unlike traditional antibiotics which target bacterial intracellular targets[180], next generations strategies for combating bacteria will involve the development of antibiotics which hold the ability to circumvent the resistance-developing machinery of bacteria, interfere with alternative antimicrobial target, and demonstrate the ability to eliminate multiple strains of bacteria[181]. Promising candidates in this regards are antimicrobial peptides (AMPs)[182], AMP cationic analogues[183] and nanoantibiotics[184]. AMPs are short cationic peptides of used as a natural defense mechanism[185], which hold the ability to specifically target bacterial cell membranes using electrostatic interactions, leading to disruptions of cell membranes and finally cell death.[182,186]. Despite successes in eliminating a broad spectrum of drug resistant bacteria, the implementations of AMPs and AMPs cationic analogues in healthcare settings is significantly hindered by their tendency to undergo non-specific interactions with mammalian cells, which in turn imparts significant toxicity[186-188]. Furthermore, high production cost and tendency to undergo degradation in the presence of proteases, further hinder implementation of AMPs as next-generation antibiotics.[189] The other strategy, nanoantibiotics, refers to the use of nanotechnology for development of antibacterial materials that include nanoparticles, metal and metal oxides, carbon-based materials, and surfactant-based emulsions for eradication of superbugs[168,183,184,190,191]. The high surface-to-volume ratio and unique chemico-physical properties of nanomaterials are the two key factors that contribute to eradication of multidrug-resistant bacteria.[192-194] Furthermore, multiple antibacterial

mechanisms of nanoantibiotics, such as the disruption of bacterial cell membranes, generation of oxidative stress, make them highly effective against multiple strains of bacteria and inhibits the resistance development machinery.[191,193-195] Despite of its success as an antibacterial candidate, the high toxicity and lack of effective formulation strategies hinder the application of nanoantibiotics.[196] Also, most of the reported antimicrobial systems are highly efficient against planktonic bacteria, but fail to function against biofilms. To the best of our knowledge, antibacterial materials systems which is highly effective against both planktonic bacteria and biofilms, easy to construct, and biocompatible towards mammalian and red blood cells cell have not been reported.

To overcome these challenges, we integrated two antimicrobial components, AMPs and nanoantibiotics in a single nanotechnology platform and applied them synergistically to combat multidrug-resistant bacteria. In this chapter, we report the engineering of a new class of antimicrobial agents, consisting of cationic polypeptides, poly-L-lysine (PLL) encapsulating the two-dimensional transition metal dichalcogenide $MoSe_2$. Incorporation of the polypeptide PLL on the nanomaterial surface reduces non-specific peptide interactions with mammalian cells while facilitating specific interactions with the negatively charged, bacterial cell membrane. We hypothesize the presence of cationic peptides on the hydrophobic two-dimensional surface increases the local concentrations of cationic moieties, which imparts stronger force on bacterial cell membrane making it more efficient than individual components alone. For further stabilization in high salt concentrations of biological systems, we incorporated the block copolymer Pluronic F77 along with PLL on the surface of $MoSe_2$, which provided steric stabilization to these systems.

The designed $MoSe_2$/PLL/F77 systems were highly efficient in eradicating both gram-positive and gram-negative, 'ESKAPE' strains, with minimum bactericidal concentrations lower than 50 μg/ml. Furthermore, $MoSe_2$/PLL/F77 systems showed minimal to no toxicity towards both red blood and mammalian cells. Our studies also revealed $MoSe_2$/PLL/F77 can successfully penetrate and eradicate biofilms, while maintaining biocompatibility towards mammalian cells. Also, when tested in co-culture systems, $MoSe_2$/PLL/F77 showed 100% eradication of planktonic bacteria and 3-log reductions in biofilms while posing no toxicity towards mammalian cells. Unlike conventional antibiotics, $MoSe_2$/PLL/F77 did not show any significant generation of resistance towards gram-positive *S. aureus* and gram-negative *P. aeruginosa* after 20 serial passages. Furthermore, mechanistic evaluation of antibacterial actions of $MoSe_2$/PLL/F77 demonstrated multimodal antibacterial mechanism which includes electrostatic interactions with bacterial cell membrane, followed by disturbance to membrane potential, oxidative stress and finally cell death. Overall, we have developed a new nanoengineered polypeptide/2D inorganic material antibacterial that can eradicate planktonic bacteria and biofilms without posing significant toxicity to mammalian and red blood cells.

4.2) Results and discussion

4.2.1) Designing of antibacterial systems

Inspired by previous antibacterial mechanism of naturally occurring cationic peptide[197-199], we selected the commercially available cationic polypeptide poly-L-lysine (PLL) and peptide to interface with 2D $MoSe_2$ nanosheets. We hypothesized that the dual

amphipathic and cationic nature of PLL would perform two function: first, its cationic nature would assist in interactions with negatively charged bacterial cell membrane, and second, its amphiphilic nature would enable to stably encapsulate the two-dimensional transition metal dichalcogenide $MoSe_2$. $MoSe_2$ was ultrasonicated in the presence of PLL in the weight ratio of 20:1 for 2 hours. During this process, the cationic polypeptides undergo intercalation between layers of $MoSe_2$, weakening the van der Waals interactions, and assisting the exfoliation of $MoSe_2$; whereas the presence of polycationic peptides on the surface of $MoSe_2$ further stabilizes the nanomaterials in solution phase via electrostatic repulsion. The zeta potential of PLL dispersed $MoSe_2$ was +41 mV, which indicated presence of electrostatic repulsion as a key factor towards stabilization of flakes in colloidal dispersion.

Despite of high stability of PLL-dispersed $MoSe_2$ in colloidal dispersion, PLL-dispersed $MoSe_2$ underwent deleterious electrostatic interactions in high salt concentrations of buffer medium, which in turn led to aggregation of the nanosheets. To further stabilize this system in buffer media, we supplemented PLL on the surface of the nanosheets with the block copolymer Pluronic F77, which in turn provided additional stabilization to nanosheets using steric repulsion. To further confirm the replacement of PLL, the zeta potential of the colloidal dispersion was measured and showed reduction of zeta potential from + 41 mV to +21 mV (Figure S1). Furthermore, the $MoSe_2$/PLL/F77 hybrid structure was found to be stable in wide range of buffers, including M9, MEM and 1x PBS. After successful stabilization of $MoSe_2$ nanosheets using PLL and Pluronic-F77, excess polymer was removed from the solutions using dialysis. After purification, $MoSe_2$/PLL/F77 dispersion was characterized using UV-Vis spectroscopy, which showed

presence of two excitonic peaks. The presence of the excitonic peaks indicated that the $MoSe_2$ remained in its pristine 2H phase after exfoliation. We further evaluated the morphology of nanomaterial using transmission electron microscopy (TEM) and atomic force microscopy (AFM). The morphological analysis of $MoSe_2$/PLL/F77 using TEM, demonstrated successful exfoliation and thin-flake like structure of dispersed nanomaterial with lateral dimension in the range of 50-100 nm. The polymer content on the surface of $MoSe_2$ was further determined using Thermogravimetric analysis (TGA). The TGA analysis of $MoSe_2$/PLL/F77 demonstrated presence of 22% polymer on the surface of $MoSe_2$. (Figure S2)

4.2.2) *In vitro* antibacterial activity of $MoSe_2$/PLL/F77

After successful preparation and characterization of $MoSe_2$/PLL/F77, we evaluated the antibacterial efficiency of $MoSe_2$/PLL/F77 against two model bacterial strains, gram-positive *S. aureus* and gram-negative *E. coli* K12 MG1655, by determining minimum bactericidal concentrations (MBC). The MBC refers to the lowest concentrations of an antibacterial required to achieve 100% elimination of bacteria. Antimicrobial assays for determination of MBC were conducted in minimal essential medium (MEM). For MBC determination, bacteria were initially treated with $MoSe_2$/PLL/F77 for 4 hours, [200] followed by plating in agar and incubation for 24 hours at 37 °C. The MBC for $MoSe_2$/PLL/F77 was 25 μg/ml for gram-negative *E. coli* and 50 μg/ml for gram-positive *S. aureus*. For comparison, we also tested the antibacterial efficiency of $MoSe_2$/PLL and PLL under the same conditions. The $MoSe_2$/PLL underwent aggregations in MEM medium within few minutes of additions and no antibacterial action was observed. For

comparison to PLL, we used TGA studies to determine that PLL and Pluronic F77 comprised overall 22% of the $MoSe_2$/PLL/F77 mass. Since both polymers, PLL and Pluronic-F77 showed same TGA signature, it was not possible to isolate the concentrations of the individual polymers. For our comparison studies, we eliminated the contribution from Pluronic-F77 and used 22% as PLL concentrations for further studies. On treatment with same concentrations of PLL as present on the surface of $MoSe_2$/PLL/F77, we observed PLL delayed the growth of bacteria on agar plates but did not show any significant killing under the same treatment conditions.

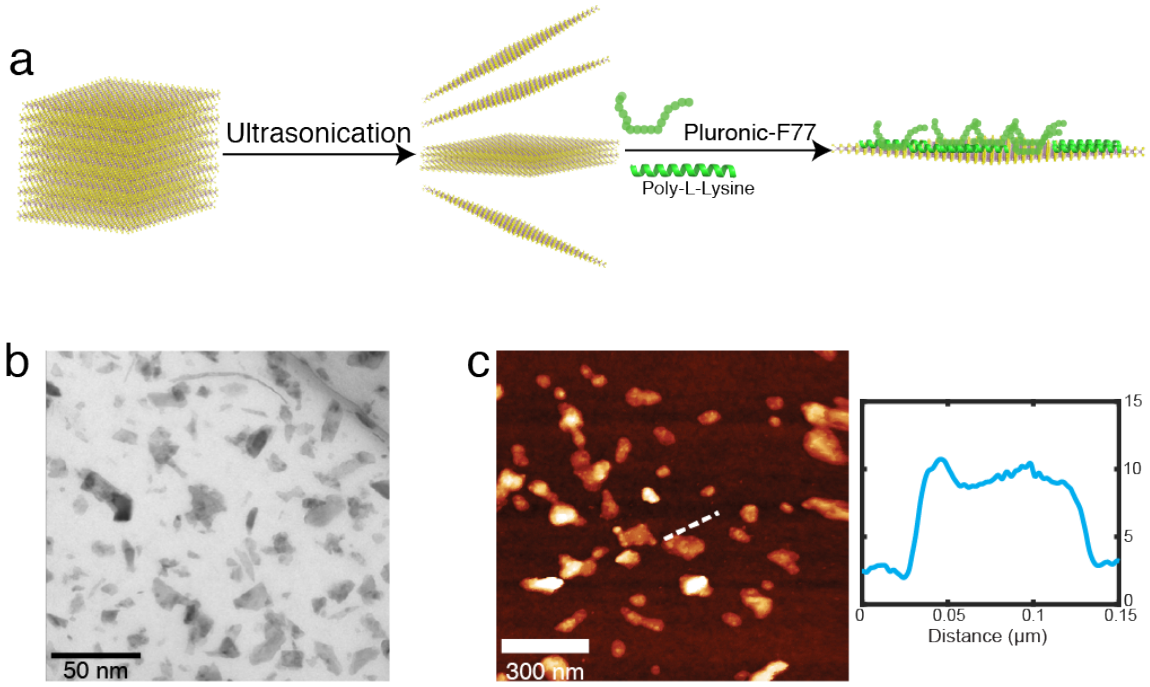

Figure 1: Schematic and characterization of $MoSe_2$/PL/F77 (a) Schematic demonstrating the exfoliation and dispersing $MoSe_2$ in the presence of poly-L-lysine and Pluronic-F77 (b) TEM image demonstrating the nanosheet like morphology of $MoSe_2$/PL/F77 (c) AFM images demonstrating the thin nanosheet like morphology.

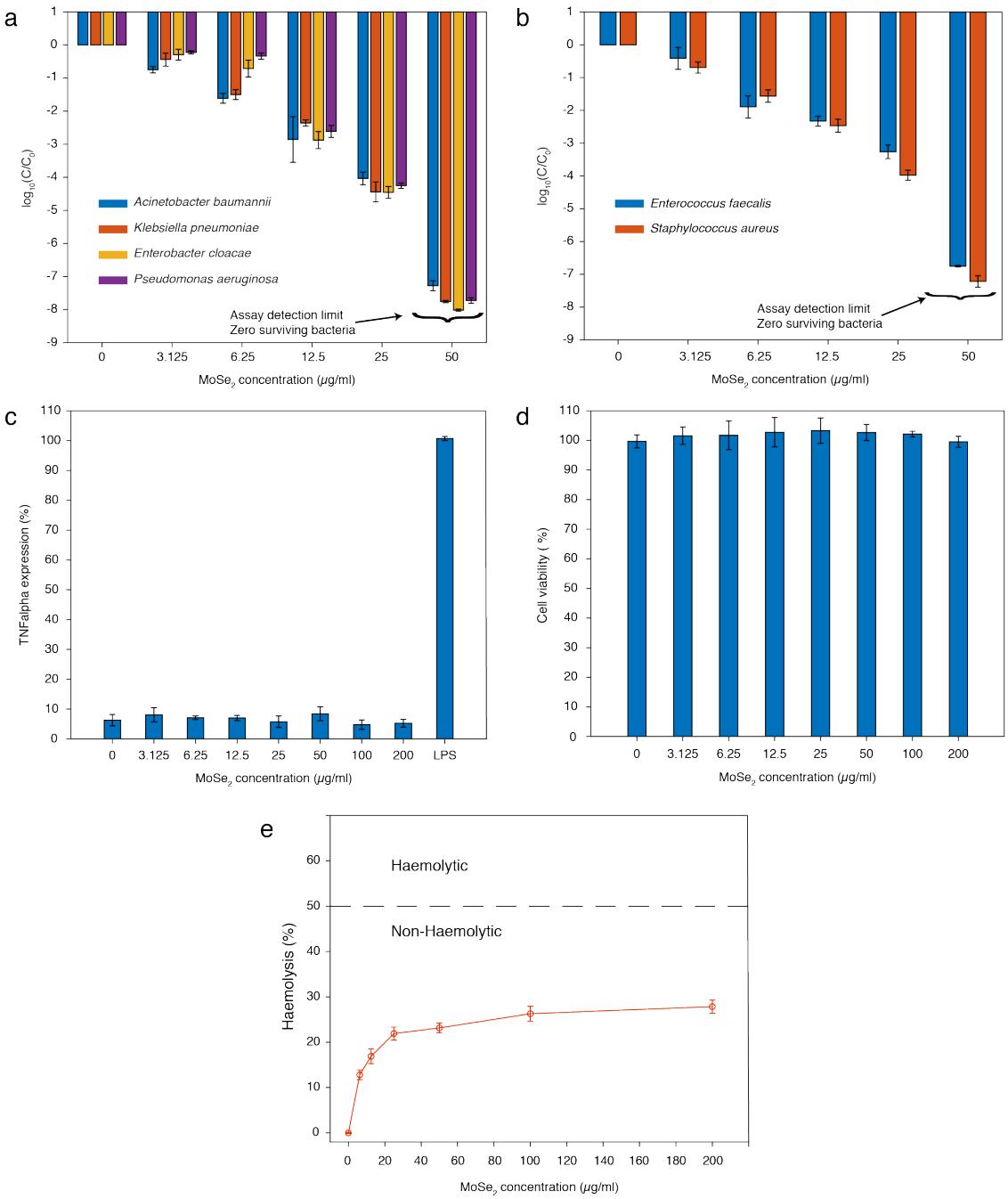

Figure 3.2: Antibacterial activity, immunogenicity and biocompatibility determination of $MoSe_2$/PLL/F77 (a) Minimum bactericidal concentrations of $MoSe_2$/PLL/F77 on gram-negative 'ESKAPE' bacteria (b) Minimum bactericidal concentrations of $MoSe_2$/PLL/F77 on gram-positive 'ESKAPE' bacteria (c) Determination of TNFα expression of RAW 264.7 cells in the presence of $MoSe_2$/PLL/F77. Lipopolysaccharides (LPS) was used as a positive control (d) Haemolysis of human red blood cell on treatments with $MoSe_2$/PLL/F77.

After successful demonstration of the antibacterial activity of $MoSe_2$/PLL/F77 on model systems, we further extended our antibacterial studies towards multidrug-resistant (MDR) pathogenic 'ESKAPE' bacterial strains. The 'ESKAPE' strains represent a multidrug-resistant group of bacteria family that are prone to develop resistance to commonly used antibiotics[201]. The lack of proper antibiotics for treating 'ESKAPE' strains makes them one of the biggest threats to hospitals and clinics. The challenges posed by these MDR strains in clinical settings inspired us to test the antibacterial efficiency of our designed systems on these bacterial strains. The MBC of $MoSe_2$/PLL/F77 was determined for the 'ESKAPE' strains using the same strategy as the model systems. $MoSe_2$/PLL/F77 successfully eliminated both gram-positive and gram-negative strains at 50 μg/ml, Figure 2 (a) and Figure 2 (b). The same MBC values for all the bacterial strains implied that antibacterial action of $MoSe_2$/PLL/F77 is independent of bacterial species. Furthermore, same MBC value for *P. aeruginosa* and *K. pneumoniae* was surprising as both the species possess a thick extracellular capsule[202,203], which contributes towards low permeability of antibiotics and makes treatment difficult. The species-independent antibacterial action of $MoSe_2$/PLL/F77 eliminates the traditional problem of one drug-one bug approach of traditional therapy. [200]

4.2.3) Biocompatibility of $MoSe_2$/PLL/F77

After successful *in vitro* antibacterial evaluation of $MoSe_2$/PLL/F77, we tested the biocompatibility of $MoSe_2$/PLL/F77 in two different cell lines, human red blood cells (RBC) and rat macrophage RAW 264.7 cells. We tested the compatibility of $MoSe_2$/PLL/F77 on human red blood cell using haemolysis assays. The haemolysis assay

measures the toxicity of different compounds against red blood cells by determining the extent of cell lysis upon interaction with different molecules. We investigated the hemolytic activities of $MoSe_2$/PLL/F77 on human RBC by incubating cells at different concentrations of $MoSe_2$/PLL/F77 for 2 hours. After incubation with $MoSe_2$/PLL/F77, no significant haemolysis was observed, with only 30% hemolysis of red blood cells observed at concentrations as high as 200 μg/ml (4x MBC), Figure 2(e). Concentrations which cause less than 50% haemolysis of red blood cells are considered haemocompatible.[183] After successful determination of hemocompatibility, we further determined the biocompatibility of $MoSe_2$/PLL/F77 on rat macrophage cell, RAW 264.7. The cytotoxicity of $MoSe_2$/PLL/F77 was determined using an alamerBlue cell proliferation assay. This fluorometric assay measures the metabolic activity of cells based on oxidation-reduction chemistry and it undergoes oxidation from non-fluorescent form to fluorescent form[204]. On treatment with $MoSe_2$/PLL/F77 at a concentration as high as 200 μg/ml (4x MBC), no significant toxicity was observed for the RAW-264.7 cells.

We further tested the chronic toxicity of $MoSe_2$/PLL/F77 using inflammatory cytokine responses from macrophage RAW 264.7, Figure 2 (c). The macrophage RAW 264.7 cells were incubated with $MoSe_2$/PLL/F77 and the immune response was measured using tumor necrosis factor alpha (TNF-α) cytokine expression[205]. After incubations at 200 μg/ml (4x MBC) with $MoSe_2$/PLL/F77, no TNF-α expression was observed. The absence of TNF-α expression at 200 μg/ml, clearly demonstrates *in vitro* immune compatibility with mammalian immune cells. The $MoSe_2$/PLL/F77 studies on red blood cells and RAW-264.7 cells clearly demonstrated hemocompatibility, biocompatibility and

immune compatibility of our designed systems.

4.2.4) In vitro biofilms and persister eradication using $MoSe_2$/PLL/F77

After successful *in vitro* antibacterial and biocompatibility evaluations, we further extended our studies and evaluated the antibacterial efficiency of $MoSe_2$/PLL/F77 on biofilms of both gram-negative *A. baumannii* and gram-positive *S. aureus*. Bacterial biofilms develop an extracellular matrix, which in turn inhibits the penetration of antibiotics[206]. Furthermore, bacteria in biofilms also employ multiple defense mechanisms, including limited nutrient use, slow growth and adaptive stress response, which all make them harder to treat using traditional strategies[207,208]. To investigate the effect of these defenses on the nanosheet system, we evaluated the antibiofilm efficiency of $MoSe_2$/PLL/F77 on gram-negative *A. baumannii* and gram-positive *S. aureus*. $MoSe_2$/PLL/F77 completely eradicated biofilms of both gram-positive *S. aureus* and gram-negative *A. baumannii* bacteria at 200 µg/ml concentrations. Unlike traditional therapy, the strong cationic and hydrophobic nature of $MoSe_2$/PLL/F77 favors the adhesion and breakdown of extracellular matrix, which in turn led to the elimination of bacteria from the biofilms. After successful elimination of biofilms, we further evaluated the activity of $MoSe_2$/PLL/F77 against biofilms of persisters. Persisters represent the dormant subpopulation of microbial populations, with higher tolerance towards antibiotics than regular cells[209]. For deriving persister cells from biofilms, the biofilms were exposed to rifampicin (100x MIC). After exposure to rifampicin for 24 hours, the biofilms were washed with 1x PBS to remove the planktonic dead bacteria, and persisters were treated with different concentrations of $MoSe_2$/PLL/F77 for 4 hours and cell

viability was determined on TSB agar plates. 200 µg/ml of $MoSe_2$/PLL/F77 showed 100% elimination of biofilm persisters, Figure 3 (b).

After successful eradication of biofilms, we further evaluated the antibiofilm efficiency of $MoSe_2$/PLL/F77 in the presence of HEK 293 human embryonic cells. The eradication of biofilms from human tissues and organs is greatly hampered by the toxicity imposed by the antibacterial systems towards human cells.[210] Before testing the $MoSe_2$/PLL/F77 efficiency in co-culture systems, we first tested the cytotoxicity of $MoSe_2$/PLL/F77 towards mammalian HEK 293 cells. No significant cytotoxicity was observed for HEK 293 at all the tested concentrations of $MoSe_2$/PLL/F77, Figure 4 (c). To test the antibiofilm efficiency of $MoSe_2$/PLL/F77 in the presence of human cell, we designed an *in vitro* biofilm co-culture system of gram-negative MDR *P. aeruginosa* bacteria and HEK 293 mammalian cells. For designing of *in-vitro* co-culture systems, *P. aeruginosa* was seeded on confluent HEK 293 cells and allowed to grow overnight to form a biofilm layer. After biofilm formation with HEK 293, the co-culture system was treated with range of $MoSe_2$/PLL/F77 concentrations for 6 hours and the cell viability of both bacteria and mammalian cells was determined. The $MoSe_2$/PLL/F77 showed reduction of biofilm viability at all the treated concentrations with a maximum 4-log reduction at 200 µg/ml, without causing any significant toxicity to mammalian cells, Figure 4 (d).

After successful removal of biofilms from co-culture systems, we further evaluated the antibacterial actions of $MoSe_2$/PLL/F77 towards planktonic gram-positive *S. aureus* and gram-negative *A. baumannii* in the presence of HEK 293 cells. The confluent HEK 293 cells were seeded with 10^6 bacteria, and then *in vitro* co-culture

systems were treated with range of $MoSe_2$/PLL/F77 concentrations for 4 hours and cell viability of both mammalian cells and bacteria was evaluated. $MoSe_2$/PLL/F77 showed reductions of both bacteria with 100% eradications at 200 µg/ml. The ability of $MoSe_2$/PLL/F77 to eradicate planktonic bacteria and biofilms in the presence of mammalian cells makes them promise next generation antibacterial systems for inhibiting the MDR infections caused by surgical instruments and implants.

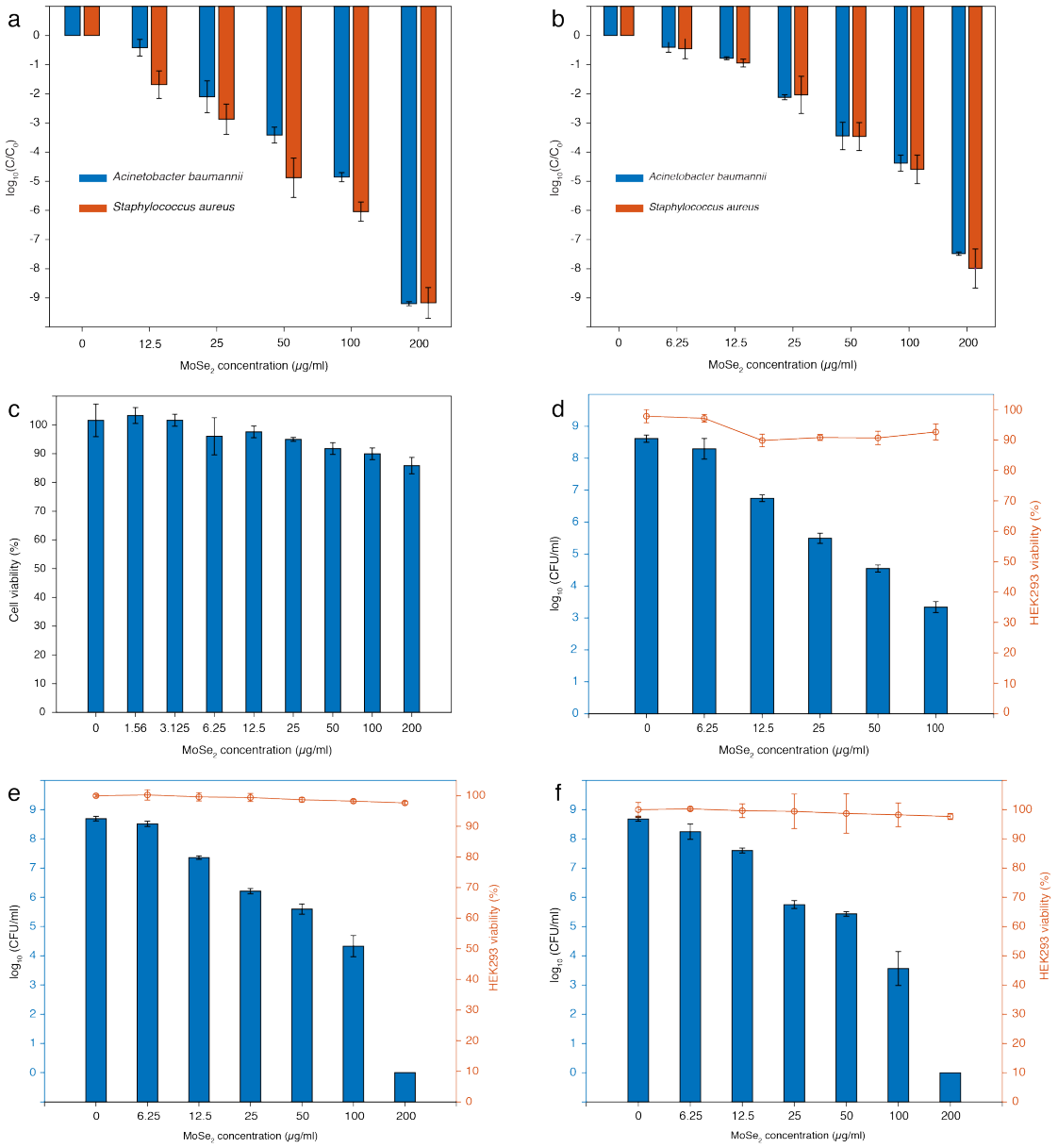

Figure 3. 3: Biofilm eradication efficiency of $MoSe_2$/PLL/F77 towards biofilms gram-positive and gram-negative bacteria and in co-culture systems of bacteria and mammalian cells. (a) Minimum biofilm eradication concentrations of gram-positive *S. aureus* and gram-negative *A. baumannii* (b) Minimum bactericidal concentrations for persisters from biofilms. (c) Cell viability assay of $MoSe_2$/PLL/F77 towards HEK 293. (d) Biofilm eradication concentrations of $MoSe_2$/PLL/F77 for *P. aeruginosa* in the presence of HEK 293 (e) Eradication of gram-negative *A. baumanni* using $MoSe_2$/PLL/F77 in a co-culture of HEK 293 and bacteria. (f) Eradication of gram-positive *S. aureus* using $MoSe_2$/PLL/F77 in co-culture model of HEK293 and bacteria.

4.2.5) Antibacterial mechanistic analysis of $MoSe_2$/PLL/F77

After successful evaluation of antibacterial efficiency, we analyzed the antibacterial mechanism of $MoSe_2$/PLL/F77 using scanning electron microscopy (SEM) and TEM. We analyzed morphology of gram-negative bacteria, *A. baumannii* and gram-positive *S. aureus* before and after treatment with 1x MBC of $MoSe_2$/PLL/F77. Both the bacterial strains showed intact morphology before treatment, Figure 4 (a, e). After treatment with 1x MBC of $MoSe_2$/PLL/F77, the bacterial cell membrane demonstrated the formation of small blob-like structure on the surface of bacterial membrane, Figure 4 (b, f). This effect can be attributed strong electrostatic interactions of the positively charged $MoSe_2$/PLL/F77 with negatively charged phospholipids of the bacterial outer membrane, which led to the generation of physical stress on the membrane. After analysis of bacterial morphology using SEM, we further analyzed the bacterial cytoplasm before and after treatment with $MoSe_2$/PLL/F77. Prior to treatment, TEM showed intact cytoplasm Figure 4 (c, g), whereas bacteria after treatment showed leakage of cytoplasm from cell (Figure 4 (d, h)), further evidence of strong interactions between the $MoSe_2$/PLL/F77 and the bacterial cell membrane.

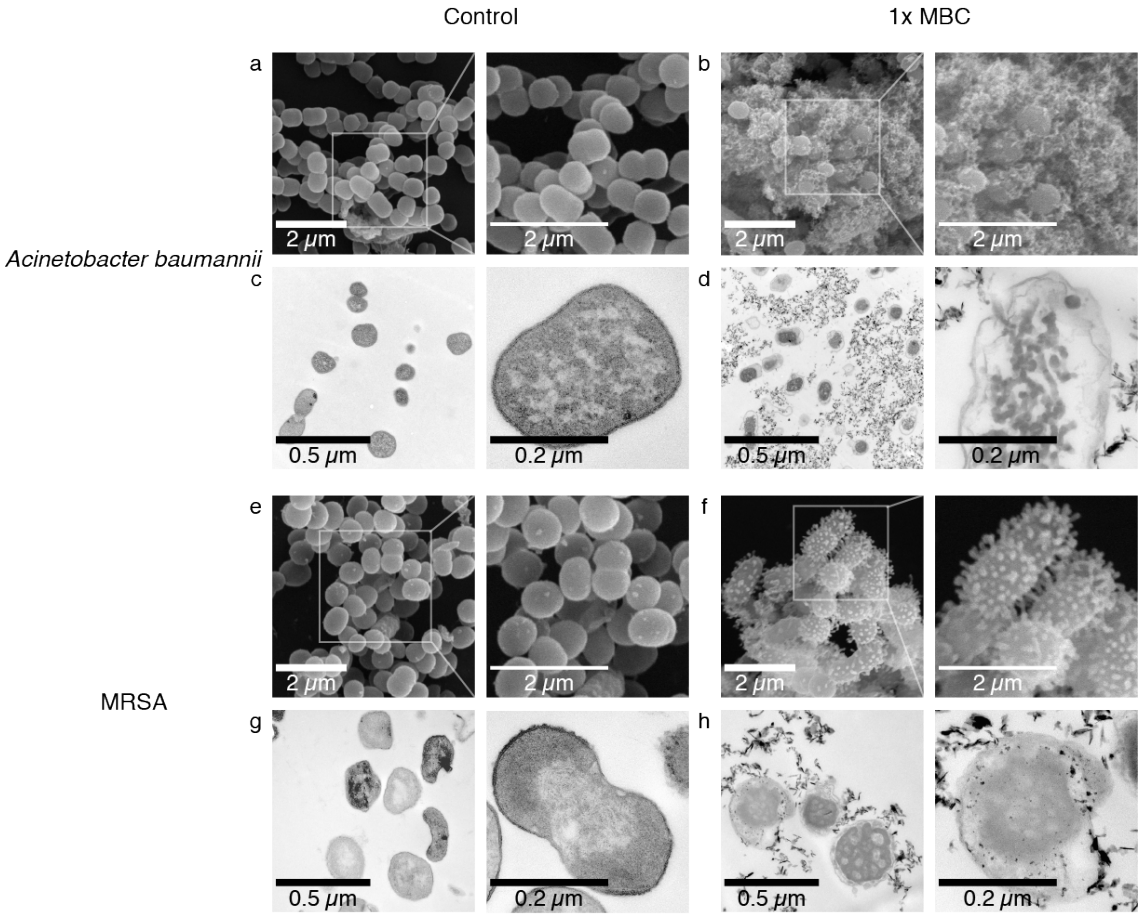

Figure 3.4: Microscopic evaluation of antibacterial mechanism of $MoSe_2$/PL/F77 (a,e) Scanning electron microscopy (SEM) image of gram-negative Acinetobacter baumannii and gram-positive MRSA before treatment, demonstrating intact cell membrane of bacteria (b,f) SEM image of gram-negative Acinetobacter baumannii and gram-positive MRSA after treatment with MoSe2/PL/F77, demonstrating damage to cell membrane after interactions with MoSe2/PL/F77 (c,g) Transmission electron microscopy (TEM) image of gram-negative Acinetobacter baumannii and gram-positive MRSA before treatment, demonstrating intact cytoplasm. (d,h) Transmission electron microscopy (TEM) image of gram-negative Acinetobacter baumannii and gram-positive MRSA after treatment, demonstrating disturbed cytoplasm and protein leakage

After microscopic evaluations of antibacterial mechanism, we further studied the extent of cell permeabilization induced by $MoSe_2$/PLL/F77 using the propidium iodide (PI) assay. Bacteria were incubated with propidium iodide (PI) after treatment with $MoSe_2$/PLL/F77 and analyzed using flow cytometry. PI is a red-fluorescent stain, which

is impermeable to living cells, whereas it permeates the membrane of damaged cells and intercalates with DNA, giving red fluorescence. After treatment with $MoSe_2$/PLL/F77, bacteria showed membrane damage at all treated concentrations, with highest membrane damage at 50 μg/ml (1x MBC). The $MoSe_2$/PLL/F77 showed 92.2% membrane damage for *A. baumannii* whereas 82.71% damage for *S. aureus*, Figure 5 (a, b). Less than 100% membrane damage at 1x MBC for both strains, can be attributed to the fact that some of the bacteria underwent complete lysis, and this subpopulation of bacteria cannot be detected using our assay conditions.

After determination of membrane damage, we further evaluated the impact of membrane damage on the transmembrane potential of bacteria. The potential across the bacterial membrane potential of bacterial membrane facilitates the transport of ions, nutrients and biological molecules through the membrane. We incubated both gram-positive *S. aureus* and gram-negative *A. baumannii* with $MoSe_2$/PLL/F77, and the membrane potential was determined using the probe DiOC2. DiOC2 exhibits green fluorescence for depolarized cells whereas it undergoes self-association in hyperpolarized cells causing fluorescence shifts from green to red[211]. The treatment of both strains of bacteria with $MoSe_2$/PLL/F77, induces polarization to bacterial cell with membrane potential shifting from hyperpolarized to depolarized with increasing concentrations, Figure 5 (c, d). From these studies, we hypothesized that cationic $MoSe_2$/PLL/F77 undergoes strong electrostatic interactions with negatively charged bacterial cell membranes, which result in membrane damage followed by polarization of bacterial cell membrane and in turn led to unregulated ion movement and membrane potential dissipation. To further prove the hypothesis of electrostatic interactions as a key

antimicrobial mechanism, we carried out a competitive inhibition assay with *E. coli* lipopolysaccharides (LPS). For the competitive inhibition assay, $MoSe_2$/PLL/F77 was first incubated with varying concentrations of LPS, and a co-mixture of 0.5 x MBC of $MoSe_2$/PLL/F77 and LPS was further used for treating *E. coli*. With increasing concentrations of LPS, the antibacterial efficiency of $MoSe_2$/PLL/F77 decreased, and this can be attributed to the fact that that cationic nature of $MoSe_2$/PLL/F77 is being neutralized with negatively charged LPS, which in turn led to decreases in the antibacterial efficiency of $MoSe_2$/PLL/F77, Figure 5 (f).

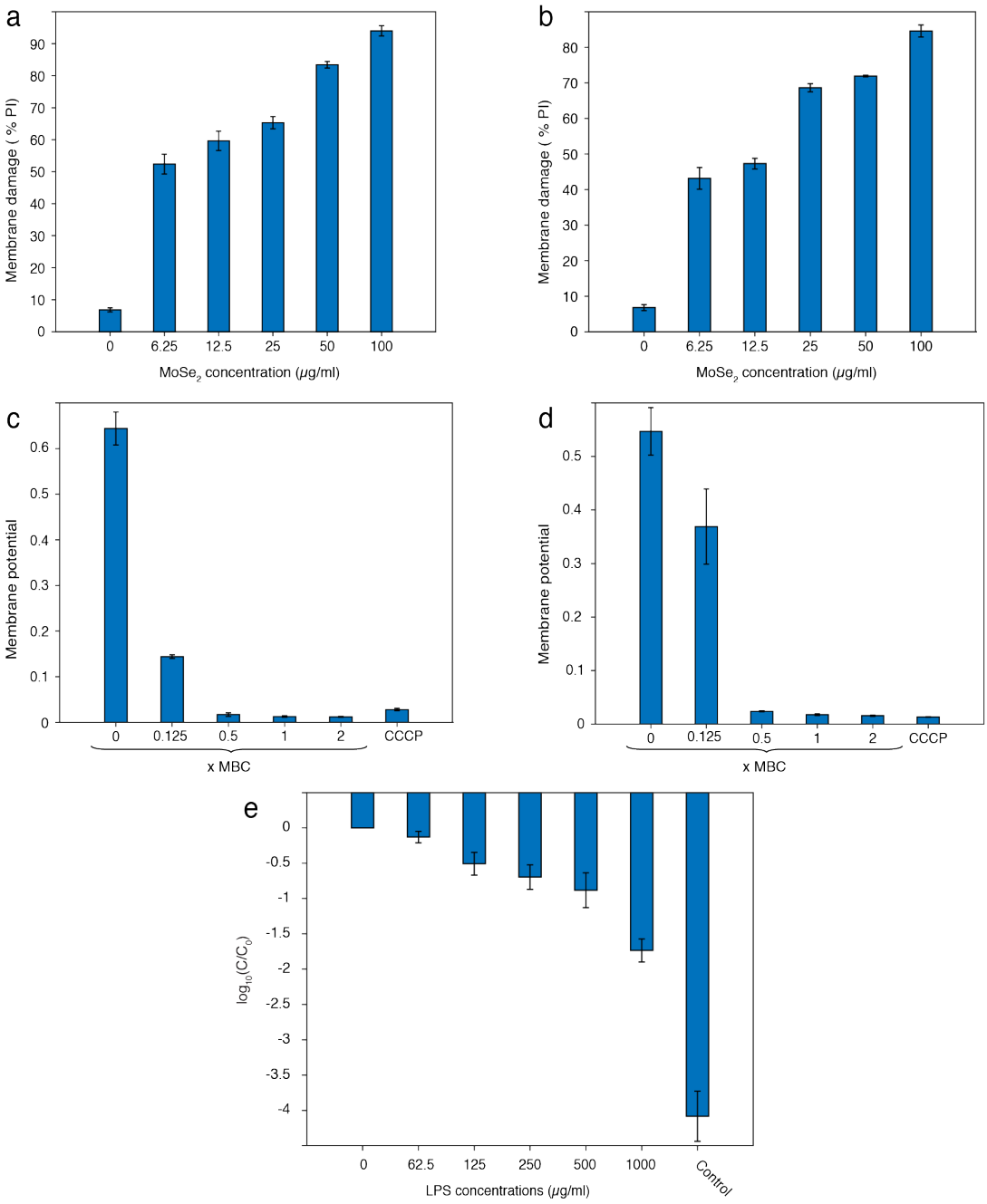

Figure 3.5: Mechanistic analysis of antibacterial action of Microscopic evaluation of antibacterial mechanism of $MoSe_2$/PL/F77 using microbiological assays (a,b) PI (%) cells demonstrating membrane damaged cells of gram-negative Acinetobacter baumannii and gram-positive S. aureus after interactions with MoSe2/PL/F77 (c,d) Change in membrane potential after interactions with MoSe2/PL/F77 for gram-negative Acinetobacter baumannii and gram-positive S. aureus (e) The change in bactericidal efficiency of MoSe2/PL/F77 towards E.coli MG1655 in the presence of bacterial lipopolysaccharides

4.2.6) Resistance development study of bacteria against $MoSe_2$/PLL/F77 and antibiotics

The prolonged exposure to particular antibiotics has generally led to the development of resistance, which in turn makes them ineffective for long term use. We thus performed longer term exposure studies to investigate the potential of bacteria to develop resistance to $MoSe_2$/PLL/F77, poly-L-lysine and clinically used antibiotics. We studied resistance development on two different well-known clinical strains, gram-positive *S. aureus* and gram-negative *P. aeruginosa*. In these experiments, bacteria were treated with antibiotics for 16 hours, MIC was determined and bacteria from sub-MIC concentrations was further harvested for next study. The study was carried out for 20 serial passages over a period of approximately three weeks. As shown in Figure 6 (a, b), no resistance development was observed for $MoSe_2$/PLL/F77 after 20 serial passages. In contrast, both strains of bacteria developed resistance to cationic polypeptide, poly-L-lysine. After 8 passages, a 4-log dosage increase was observed for both *S. aureus* and *P. aeruginosa.* Furthermore, we evaluated the development of bacterial resistance against clinically used antibiotics. For *P. aeruginosa*, we treated the bacteria with two clinically used last resort antibiotics, imipenem and gentamicin. The bacteria quickly developed resistance to both these antibiotics, with more than 4-log increase in dosage after the 10^{th} passage. Similarly, we tested the resistance development of *S. aureus* against clinically used antibiotic, rifampicin. The bacteria developed resistance to the rifampicin, with more than 4-log increase in dosage after the 8^{th} passage. Unlike traditional antibiotics, the presence of electrostatic interactions and ability to physically disrupt the cell membrane

of $MoSe_2$/PLL/F77 enables it to remain effective against evolving bacteria.

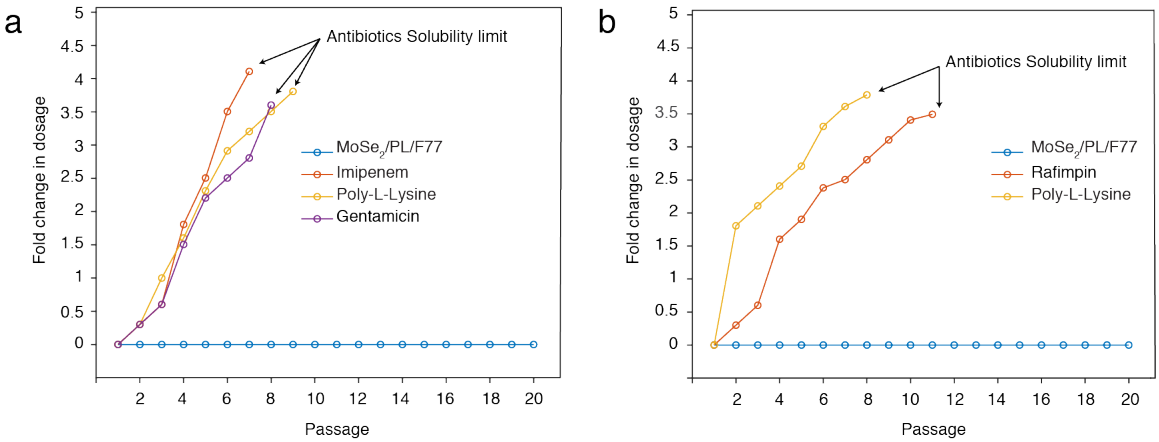

Figure 3. 6: Resistance study of $MoSe_2$/PL/F77 towards gram-positive and gram-negative *S. aureus* and *P. aeruginosa* (a) Development of resistance by *Pseudomonas aeruginosa* against multiple last-resort antibiotics (imipenem, gentamicin), the cationic polymer poly-L-lysine and $MoSe_2$/PL/F77 after treatment at sub-MIC concentrations. (b) Development of resistance by *Staphylococcus aureus* against the last-resort antibiotic rifampin, poly-L-lysine and $MoSe_2$/PL/F77 after treatment at sub-MIC concentrations.

4.2.7) Proposed antibacterial mechanism of $MoSe_2$/PLL/F77

Unlike cationic peptides (monomeric form), the cationic PLL-encapsulated $MoSe_2$ nanosheet, increases the local concentrations of positive charges, and the $MoSe_2$/PLL/F77 system imparts stronger electrostatic force of interaction compared to monomeric polypeptide systems. This study can further be correlated with previous studies, which showed integration of polypeptides in a fixed geometry increases the antibacterial efficiency[168,212]. $MoSe_2$/PLL/F77 first binds with LPS, imparts a strong electrostatic force of interactions, which in turn lead to destabilization of outer membrane and fragmentation of the bacterial membrane. The effect triggers polarization of the cell membrane potential, which in turn led to unregulated ion movement. Furthermore, at high concentrations of $MoSe_2$/PLL/F77, the force of interaction is so strong that it leads to direct cell lysis. This order of interactions is supported by electron microscopy

measurements and bioassays. The fragmentation of cytoplasmic membrane is a key factor which triggers cell death. Furthermore, presence of strong electrostatic forces in $MoSe_2$/PLL/F77 systems, aids in the breaking of the biofilm matrix and removal of bacteria from biofilms.

4.3) Conclusion

We successfully designed and fabricated a novel therapeutic antibacterial platform that can combat multidrug-resistant planktonic bacteria and biofilms using a multimodal antibacterial mechanism. The designed systems target the bacterial cell membrane using electrostatic interactions, which in turn led to deformation of cell membrane, polarization of the cell, cytoplasmic leakage and finally cell death. Furthermore, the designed system was successful in eliminating both biofilms and persisters. It specifically and efficiently eradicated biofilm and planktonic bacteria from a co-culture system of bacteria and mammalian cell. Unlike traditional antibiotics, no development of resistance was observed by bacteria after 20 serial passages.

4.4) Methods

4.4.1) Dispersion of $MoSe_2$ in Poly-L-Lysine (PLL) and Pluronic-F77

In a typical experiment, 0.2 mg of $MoSe_2$ (Sigma Aldrich) was added to a 5-ml aqueous solution containing 10 mg of PLL (Sigma Aldrich). $MoSe_2$ bulk powder was ultrasonicated with a 13-mm tip at a power level of 12 W for 2 hours (Branson Digital Sonifier 450D). After ultrasonication, the sample was centrifuged at 5000 g for 5 minutes followed by 21,000 g for 1 minute to remove the unexfoliated flakes. The supernatant of PLL-encapsulated $MoSe_2$ was then carefully decanted. The solution was further

ultrasonicated for 30 minutes with 0.5% Pluronic-F77 (BASF) for 30 minutes. The resulting solution was than dialyzed for 72 hours, using 100 kD molecular cut off cellulose ester membrane. The dialyzed solution was then used for further study.

4.4.2) TEM analysis of $MoSe_2$/PLL/F77

The sample was prepared using drop casting method. Briefly, 6 µl of dispersed solution was drop casted onto holey carbon copper grids and imaged using a Phillips CM-12 TEM.

4.4.3) Antibacterial studies

The antibacterial activity of $MoSe_2$/PLL/F77 was studied using the wild-type *E. coli* strain MG1655 (ATCC-700926), *Staphylococcus aureus* (ATCC-29213), *methicillin-resistant Staphylococcus aureus* (ATCC-BAA 1720), *Pseudomonas aeruginosa* (ATCC-BAA 2113), *Klebsiella pneumoniae* (ATCC- BAA 2342), *vancomycin-resistant Enterococcus faecium* (ATCC-51299), *Acinetobacter baumannii* (ATCC- BAA 1797) and *Enterobacter cloacae* (ATCC- BAA 2468). LB medium (Sigma Aldrich) and LB agar (Sigma Aldrich) were used to grow *E. coli* strain MG1655. TSB broth (Sigma Aldrich) and TSB agar (Sigma Aldrich) were used to grow *Staphylococcus aureus*, *Methicillin resistant Staphylococcus aureus*, *Pseudomonas aeruginosa* and *Acinetobacter baumannii* whereas *Vancomycin-resistant Enterococcus faecium* were grown in BHB broth (Sigma Aldrich) and BHB agar (Sigma Aldrich) in the presence of 4mcg/ml of vancomycin. MHB broth (Sigma Aldrich) and MHB agar (Sigma Aldrich) was used to grow *Klebsiella pneumoniae*. Single colonies were picked up from the agar plates and allowed to grow overnight in 5 ml of culture medium. Then, the sample was diluted 100

times in medium and allowed to grow until it reached 0.3 OD. Cultures were centrifuged at 2000 rpm for 10 minutes, and pellets were washed three times in phosphate buffer saline (PBS, Sigma Aldrich) to remove medium constituents. Finally, cell pellets were re dispersed in Minimal essential medium and diluted to a cell concentration of 10^7 CFU/ml. Bacteria at concentrations of 10^7 CFU/ml were incubated with different concentrations of nanomaterials (0.625-100 μg/ml) for 2 hours. After incubation, bacteria were plated in agar plates using serial dilution method and allowed to grow overnight.

4.4.4) Haemolysis assay

Citrate-stabilized fresh human red blood cells (RBCs) were purchased from VWR and processed as soon as received. Fresh RBCs were diluted in 1x PBS, centrifuged at 5000g for 5 minutes. The supernatant was collected, and pellet was redispersed in 1x PBS. This step was repeated 4 times to remove any haemoglobin from lysed cell. After washing, the cell was redispersed in 1x PBS and diluted to a final concentration of 2 x 10^7 cell/ml. The diluted cell was than incubated with varying concentrations of nanomaterials in a humidified atmosphere containing 5% CO_2 at 37 °C for 2 hours. After incubation, solution was centrifuged, and absorbance of supernatant was measured at 570 nm. RBC suspension in 1x PBS was used as a negative control whereas RBC lysed with 0.5% Triton X-100 was taken as a positive control.

4.4.5) Mammalian cell culture

Rat macrophage 264.7 cell and human embryonic kidney cells HEK 293 were purchased from ATCC. Both the cell line was cultivated in DMEM medium containing 10% FBS and 1% antibiotics. The cells were cultured in a humidified atmosphere

containing 5% CO_2 at 37 °C. The cells were passaged thrice a week before performing cell experiments.

4.4.6) Determination of TNF alpha expression study of RAW 264.7 macrophage cell

3 x 10^4 order of RAW macrophage 264.7 cell was seeded in 96-well plate in a humidified atmosphere in 5% CO_2 at 37 °C for 24 hours. The cells were treated with varying concentrations of nanomaterials for 4 hours. After 4 hours of treatment with nanomaterial, solution was removed and replaced with fresh medium. The cell was further incubated for 24 hours. After 24 hours, the culture media was collected, and TNF-α measurement was carried out using ELISA kit. 100 ng/ml of lipopolysaccharide was used as a positive control. The experiment was performed in quadruplicate.

4.4.7) Determination of cell viability of mammalian cell

Cell viability was determined on both RAW 264.7 and HEK 293 cells. Approximately 3 x 10^4 cell were pre-seeded in 96 well plate. The cell was grown in humidified atmosphere in 5% CO_2 at 37 °C for 24 hours. The cells were incubated with varying concentrations of nanomaterials for 24 hours. After incubations, supernatant was removed and replaced with 10% Alamer blue solution in DMEM. After 4 hours incubation with 10% alamer blue solution, the fluorescence was measured (excitation/emission: 560 nm/610nm). Cells without nanomaterials were considered as 100% viable. All experiments were performed in quadruplicate.

4.4.8) Biofilm formations and treatment

Single colonies of *Acinetobacter baumannii* (ATCC- BAA 1797) and *Staphylococcus aureus* (ATCC-BAA 1720) were inoculated in brain heart infusion broth and allowed to grow overnight at 37 °C. The overnight culture was diluted and allowed to grow, until it reaches an O.D of 0.3. The log-phase bacteria were 100-fold diluted in TSB medium, transferred to a 96-well propylene plate, incubated in humidified atmosphere for 24 hours without shaking. After 24 hours, each well was washed with 1x PBS to remove any planktonic bacteria. The washing step was carried out thrice. After washing, biofilm was treated with nanomaterial in MEM medium for 4 hours. After 4 hours of treatment, the well was again washed with 1x PBS. The 96-well plate was than bath sonicated for 10 minutes, serial diluted in 1x PBS and plated on TSB agar plates. The TSB agar plates was than incubated at 37 °C for 12 hours and colony was counted.

4.4.9) Determination of antibacterial activity against persisters

Persister cells were obtained from biofilms following the reported protocol [186]. The mid-logarithmic growth-phase culture of *Staphylococcus aureus* (ATCC-BAA 1720) and *Acinetobacter baumannii* (ATCC- BAA 1797) were further diluted in brain heart infusion broth and transferred in 96 well propylene plates. The 96 well propylene plates were incubated in humidified atmosphere for 24 hours without shaking. After 24 hours, each well was washed with 1x PBS to remove planktonic bacteria. Each well was further treated with 100 µl of brain heart infusion broth containing rifampicin (3.125 µg/ml) for 24 hours. After 24 hours treatment, each well was washed with 1x PBS to remove dead planktonic bacteria. The plate was bath sonicated to dislodge the persisters. The persisters

were than treated with varying concentrations of nanomaterials for 4 hours, serially diluted in 1x PBS and plated on TSB agar plates. The TSB agar plates was incubated for 12 hours at 37 °C and colony was counted.

4.4.10) Co-culture of bacteria with mammalian cells

Approximately 3 x 10^4 HEK 293 cells were pre-seeded in a 96-well plate. The cell was grown in a humidified atmosphere in 5% CO_2 at 37 °C for 24 hours. The mid-logarithmic growth-phase culture of *Staphylococcus aureus* (ATCC-BAA 1720) and *Acinetobacter baumannii* (ATCC- BAA 1797) were centrifuged and redispersed in DMEM. The medium was removed from the 96-well plate and substituted with bacteria suspended DMEM. The co-culture systems were than treated with varying concentrations of nanomaterial for 4 hours. After 4 hours of treatment, DMEM was removed, serial diluted in 1x PBS and plated on TSB agar plate to determine the bacterial viability. A 96-well plate containing mammalian cells was than washed with 1x PBS and cell viability determined using Alamer blue assay.

4.4.11) Co-culture of biofilm with mammalian cell

Approximately 3 x 10^4 HEK 293 cells were pre-seeded in a 96-well plate. The mammalian cells were grown in humidified atmosphere in 5% CO_2 at 37 °C for 24 hours. The mid-logarithmic growth-phase culture of *Pseudomonas aeruginosa* (ATCC- BAA 2113) was centrifuged, washed with 1x PBS and re-dispersed in DMEM. The bacteria suspended DMEM were then added to the mammalian cells in the 96-well plate, and the plate was grown in a humidified atmosphere in 5% CO_2 at 37 °C for 24 hours. After 24 hours, DMEM was removed and each well was washed with DPBS multiple times to

remove the planktonic bacteria and protein debris. After washing, varying concentrations of nanomaterial were added, and the plate was incubated for 6 hours at 37 °C. After incubation, supernatant was collected, and the plate was washed with DPBS. For bacterial viability determination, the 96-well plate was bath sonicated for 10 minutes, serial diluted in 1x PBS and plated on TSB agar plates. The TSB agar plates were incubated for 12 hours and colony was counted. For mammalian cell viability, the collected supernatant was analyzed using Pierce LDH assay kit (Thermo Scientific) following manufacturer's instruction.

4.4.12) SEM and TEM analysis of bacteria

For TEM, samples were initially fixed with 2.5% glutaraldehyde overnight at 4 °C and pelleted into 0.8% uranayl acetate to form dense cell aggregates. The cell pellet was treated for 2 hours with 1% Osmium tetraoxide in DPBS, followed by washing with deionized water and then block-stained overnight at 4 °C with aqueous 0.5% uranyl acetate. The cell pellet was dehydrated in series in a graded acetone series. The sample was sectioned and post stained using 2% uranyl acetate in 50% ethanol solution and Sato's lead citrate for 3-4 minutes. Images were acquired using Phillips CM-12 TEM operated at 80 kV using a Gatan model 791 side-mount CCD camera

For SEM, samples were initially fixed using 2.5% glutaraldehyde at 4 °C, followed by washing with DPBS. The samples were postfixed with 1% osmium tetraoxide in DPBS, followed by washing with deionized water and dehydration in graded ethanol series. The samples were critically dried, sputtered coated with gold-palladium and images was captured using JEOL JSM6300 SEM operated at 15 kV.

4.4.13) Propidium iodide staining assay for determination of bacterial damage

The mid-logarithmic growth-phase culture of *Staphylococcus aureus* (ATCC-BAA 1720) and *Acinetobacter baumannii* (ATCC- BAA 1797) was centrifuged, washed with 1x PBS and re-dispersed in MEM medium. The MEM culture of bacteria was treated with varying concentrations of nanomaterial for 2 hours. After incubation, bacteria were centrifuged and washed with 1x PBS. After washing, bacteria were stained with 1 µg/ml of propidium iodide (Sigma Aldrich) for 10 minutes on ice. The stained bacteria were than analyzed using Stratedigm S1300EXi cell analyzer equipped with A600 high-throughput autosampler.

4.4.14) Membrane potential assay

The membrane potential of bacteria was determined following the manufacturer's protocol, Baclight membrane potential kit (Invitrogen). Briefly, bacteria were grown to mid-log phase and diluted to ~10^6 CFU/ml in 1x PBS. The bacteria were treated with different concentrations of $MoSe_2$/PLL/F77 (1x MBC, 0.5x MBC, 0.25 x MBC and 0.125 x MBC) for 2 hours. A fully depolarized sample was prepared with addition of 5 mM the proton ionophore, carbonyl cyanide 3-chlorophenylhydrazone (CCCP). After treatment, samples were incubated with 30 mM $DiOC_2$ for 1 hour. Membrane potential was determined using a Stratedigm S1300EXi cell analyzer equipped with A600 high-throughput autosampler using the ratio of cells exhibiting red fluorescence to cells exhibiting green fluorescence. Cell populations were gated based on untreated (polarized) and CCCP treated (depolarized) one**.**

4.4.15) LPS incubation assay

$MoSe_2$/PLL/F77 was incubated with LPS of *E. coli* O111:B4 in MEM medium for 1 hours. The mid-logarithmic *E. coli* cells in MEM medium was than incubated with $MoSe_2$/PLL/F77-LPS mixture for 2 hours at 37 °C at 200 rpm. After incubation, bacteria were serial diluted in 1x PBS, plated on LB agar plates and plate was incubated for 12 hours at 37 °C. The colony was counted, and cell viability was determined.

4.4.16) Resistance study

Staphylococcus aureus (ATCC-BAA 1720) and *Acinetobacter baumannii* (ATCC- BAA 1797) was inoculated in TSB medium and cultured overnight at 37 °C at 200 rpm. The overnight culture was further diluted in TSB medium and incubated with $MoSe_2$/PLL/F77 or antibiotics solutions in TSB medium. The plates were sealed and incubated for 16 hours. The MIC was determined. The bacteria from 0.5x MIC concentration of $MoSe_2$/PLL/F77 or antibiotics were further diluted in TSB medium and treated with fresh solution of $MoSe_2$/PLL/F77 or antibiotics and incubated as above. This process was repeated for 20 passages.

Chapter 5

Summary and Future Outlook

5.1. Thesis Summary

In conclusion, this thesis demonstrates the development of two novel biocompatible, two-dimensional material-based inorganic hybrid systems for combating multidrug-resistant bacteria. We also demonstrated unique generalizable techniques for interfacing biological molecules with two-dimensional materials.

In Chapter 3, I demonstrated solution-phase processing of TMDCs in the presence of one of the most important building blocks of biology, single-stranded DNA. To my knowledge, this is the first report demonstrating dispersion of TMDCs using short single-stranded DNA. Furthermore, we screened the affinity of different DNA sequences with respect to TMDCs and identified T_{20} as the best sequence for dispersing the TMDCs. From our studies we concluded that $MoSe_2$ has strongest affinity for DNA, with a dispersion efficiency as high as 1 mg/ml. Further, computational studies showed proper stacking of T_{20} with hexagonal crystal structure of TMDCs as a key factor towards the high dispersion efficiency of T_{20} compared to other DNA sequences. Further microscopic analysis of DNA-encapsulated TMDCs, showed a thin nanosheet morphology, which further showed efficient exfoliation of TMDCs in the presence of single stranded DNA. After successful characterization of nanosheets, we further demonstrated the antibacterial activity of $MoSe_2/T_{20}$ towards multidrug-resistant bacteria and 'ESKAPE' strains. $MoSe_2/T_{20}$ successfully eliminated all the 'ESKAPE' strains at concentrations as low as 75 μg/ml. Mechanistic evaluations of the antibacterial action of $MoSe_2/T_{20}$ revealed a

three-step pathway: first, sharp edges of nanosheet pierce through the bacterial membrane like a ‘nanoknife’ causing breakdown of cellular membrane; second, he damage to cellular membrane in turn triggers depolarization of the membranes followed by generation of oxidative stress; and finally, programmed cell death.

In Chapter 4, I demonstrated a novel positively charged inorganic nanomaterial-based nanohybrid system. The nanohybrid systems contains three components: PLL, 2D $MoSe_2$ and Pluronic-F77. The PLL provides strong electrostatic force of attraction towards the negatively charged bacterial cell membrane, whereas Pluronic-F77 provides stabilization to the systems in buffer systems. Compared to PLL alone, the hybrid nanosystems exerts stronger electrostatic force of attraction and higher antibacterial efficiency. Furthermore, $MoSe_2$/PLL/F77 successfully eradicated all the strains of multidrug-resistant bacteria from the ‘ESKAPE’ family, at a concentration as low as 25 μg/ml. The non-specific antibacterial activity of $MoSe_2$/PLL/F77 eliminates the traditional problem of ‘one bug-one drug’ approach. Mechanistic evaluations of antibacterial action of $MoSe_2$/PLL/F77 demonstrated the electrostatic attraction between the PLL present on $MoSe_2$ nanosheets and the negatively charged bacterial cell membrane led to rupture of the membrane. LPS incubation assays provide further evidence of the strong electrostatic force of attraction as a key mechanism towards antibacterial activity. Furthermore, resistance development comparison of *S. aureus* and *P. aeruginosa* with respect to $MoSe_2$/PLL/F77, antibiotics and PLL, showed no resistance development of $MoSe_2$/PLL/F77 after 20 passages, whereas bacteria developed significant resistance to both antibiotics and PLL after 10 passages.

5.2. Future outlook

5.2.1 Towards antibacterial coating material for combating multidrug-resistant bacteria

Nosocomial or 'health care associated infections' are one of the most critical problems in healthcare. Immune-compromised patients admitted into hospitals, which includes intensive care units, burn units and those undergoing organ transplantation are highly susceptible to these nosocomial infections. Furthermore, bacteria colonize on abiotic surfaces such as medicals implants causing additional surgeries and imposing a serious burden to healthcare providers. Conventional approaches to treat these infections involve the administration of antibiotics, but these interventions are not always successful. Additionally, most of the antibiotics available on the market are ineffective against multidrug-resistant bacteria and biofilms.

Our two novel antibacterial materials systems, $MoSe_2$/ssDNA and $MoSe_2$/PL/F77 can eradicate multidrug-resistant bacteria, biofilms and persisters using alternative mechanisms. The $MoSe_2$/ssDNA materials can be incorporated inside biocompatible polymer coatings such as polyvinyl chloride and used for coating surgical instruments. The presence of negatively charged $MoSe_2$/ssDNA on these coatings will likely inhibit the growth of biofilms on these surfaces. Other applications will involve vertically aligned depositions of nanomaterials on medical surfaces, which will eliminate the bacteria using sharp edges and act as a bactericidal coating. The other potential applications of DNA-encapsulated TMDCs are related to biosensing. The TMDCs surface can be augmented using functional DNAs such as biotinylated DNA which can

be further used for detections of potential biomarkers using fluorescence or microscopic techniques.

The other antibacterial system, $MoSe_2$/PL/F77, systems holds great potential for its applications as a bactericidal material. The strong affinity of these materials towards negatively charged bacterial cell wall opens up a wide range of applications towards elimination of multidrug-resistant bacteria. The potential applications in this regard will involve coating of medical equipments such as catheters, which in turn will inhibit the growth of biofilms and put an end to infections caused by these drug-resistant bacteria. Other potential applications will be in the field of therapeutics. The $MoSe_2$/PL/F77 can be incorporated into base creams such as hypromellose and used it for the treatments of chronic infections caused by MRSA and *P. aeruginosa* for burn victims and those with other wounds. Furthermore, this material can be used for designing diverse 3D imprinted surgical implants when integrated with suitable printable materials.

REFERENCES

1 Lv, R. *et al.* Transition Metal Dichalcogenides and Beyond: Synthesis, Properties, and Applications of Single- and Few-Layer Nanosheets. *Accounts of Chemical Research* **48**, 56-64, doi:10.1021/ar5002846 (2015).

2 Jariwala, D., Sangwan, V. K., Lauhon, L. J., Marks, T. J. & Hersam, M. C. Emerging Device Applications for Semiconducting Two-Dimensional Transition Metal Dichalcogenides. *ACS Nano* **8**, 1102-1120, doi:10.1021/nn500064s (2014).

3 Wang, Q. H., Kalantar-Zadeh, K., Kis, A., Coleman, J. N. & Strano, M. S. Electronics and optoelectronics of two-dimensional transition metal dichalcogenides. *Nature Nanotechnology* **7**, 699, doi:10.1038/nnano.2012.193 (2012).

4 Chhowalla, M. *et al.* The chemistry of two-dimensional layered transition metal dichalcogenide nanosheets. *Nature Chemistry* **5**, 263, doi:10.1038/nchem.1589 (2013).

5 Fan, J., Li, Y., Nguyen, H. N., Yao, Y. & Rodrigues, D. F. Toxicity of exfoliated-MoS2 and annealed exfoliated-MoS2 towards planktonic cells, biofilms, and mammalian cells in the presence of electron donor. *Environmental Science: Nano* **2**, 370-379, doi:10.1039/C5EN00031A (2015).

6 Radisavljevic, B., Radenovic, A., Brivio, J., Giacometti, V. & Kis, A. Single-layer MoS2 transistors. *Nature Nanotechnology* **6**, 147, doi:10.1038/nnano.2010.279 (2011).

7 Cheng, L. *et al.* PEGylated WS2 Nanosheets as a Multifunctional Theranostic Agent for in vivo Dual-Modal CT/Photoacoustic Imaging Guided Photothermal Therapy. *Advanced Materials* **26**, 1886-1893, doi:10.1002/adma.201304497 (2014).

8 Liu, T. *et al.* Iron Oxide Decorated MoS2 Nanosheets with Double PEGylation for Chelator-Free Radiolabeling and Multimodal Imaging Guided Photothermal Therapy. *ACS Nano* **9**, 950-960, doi:10.1021/nn506757x (2015).

9 Wang, S. *et al.* Injectable 2D MoS2-Integrated Drug Delivering Implant for Highly Efficient NIR-Triggered Synergistic Tumor Hyperthermia. *Advanced Materials* **27**, 7117-7122, doi:10.1002/adma.201503869 (2015).

10 Yin, W. *et al.* High-Throughput Synthesis of Single-Layer MoS2 Nanosheets as a Near-Infrared Photothermal-Triggered Drug Delivery for Effective Cancer Therapy. *ACS Nano* **8**, 6922-6933, doi:10.1021/nn501647j (2014).

11 Lin, T. *et al.* Visual detection of blood glucose based on peroxidase-like activity of WS2 nanosheets. *Biosensors and Bioelectronics* **62**, 302-307, (2014).

12 Yang, Y. *et al.* MoS2-Based Nanoprobes for Detection of Silver Ions in Aqueous Solutions and Bacteria. *ACS Applied Materials & Interfaces* **7**, 7526-7533, doi:10.1021/acsami.5b01222 (2015).

13 Feng, J. *et al.* Identification of single nucleotides in MoS2 nanopores. *Nature Nanotechnology* **10**, 1070, doi:10.1038/nnano.2015.219 (2015).

14 Liu, K., Feng, J., Kis, A. & Radenovic, A. Atomically Thin Molybdenum Disulfide Nanopores with High Sensitivity for DNA Translocation. *ACS Nano* **8**, 2504-2511, doi:10.1021/nn406102h (2014).

15 Loo, A. H., Bonanni, A., Ambrosi, A. & Pumera, M. Molybdenum disulfide (MoS2) nanoflakes as inherently electroactive labels for DNA hybridization detection. *Nanoscale* **6**, 11971-11975, doi:10.1039/C4NR03795B (2014).

16 Pumera, M. & Loo, A. H. Layered transition-metal dichalcogenides (MoS2 and WS2) for sensing and biosensing. *TrAC Trends in Analytical Chemistry* **61**, 49-53, (2014).

17 Najmaei, S., Yuan, J., Zhang, J., Ajayan, P. & Lou, J. Synthesis and Defect Investigation of Two-Dimensional Molybdenum Disulfide Atomic Layers. *Accounts of Chemical Research* **48**, 31-40, doi:10.1021/ar500291j (2015).

18 Chou, S. S. *et al.* Ligand Conjugation of Chemically Exfoliated MoS2. *Journal of the American Chemical Society* **135**, 4584-4587, doi:10.1021/ja310929s (2013).

19 Guan, G. *et al.* Protein Induces Layer-by-Layer Exfoliation of Transition Metal Dichalcogenides. *Journal of the American Chemical Society* **137**, 6152-6155, doi:10.1021/jacs.5b02780 (2015).

20 Bang, G. S. *et al.* DNA-Assisted Exfoliation of Tungsten Dichalcogenides and Their Antibacterial Effect. *ACS Applied Materials & Interfaces* **8**, 1943-1950, doi:10.1021/acsami.5b10136 (2016).

21 Kalantar-zadeh, K. *et al.* Two-Dimensional Transition Metal Dichalcogenides in Biosystems. *Advanced Functional Materials* **25**, 5086-5099, doi:10.1002/adfm.201500891 (2015).

22 Meyer, J. C. *et al.* The structure of suspended graphene sheets. *Nature* **446**, 60, doi:10.1038/nature05545 (2007).

23 Geim, A. K. & Novoselov, K. S. The rise of graphene. *Nature Materials* **6**, 183, doi:10.1038/nmat1849 (2007).

24 Huang, X. *et al.* Graphene-Based Materials: Synthesis, Characterization, Properties, and Applications. *Small* **7**, 1876-1902, doi:10.1002/smll.201002009 (2011).

25 Novoselov, K. S. *et al.* Electric Field Effect in Atomically Thin Carbon Films. *Science* **306**, 666, doi:10.1126/science.1102896 (2004).

26 Novoselov, K. S. *et al.* Two-dimensional gas of massless Dirac fermions in graphene. *Nature* **438**, 197-200, doi:10.1038/nature04233 (2005).

27 Zhang, Y., Tan, Y.-W., Stormer, H. L. & Kim, P. Experimental observation of the quantum Hall effect and Berry's phase in graphene. *Nature* **438**, 201-204, doi:10.1038/nature04235 (2005).

28 Balandin, A. A. *et al.* Superior Thermal Conductivity of Single-Layer Graphene. *Nano Letters* **8**, 902-907, doi:10.1021/nl0731872 (2008).

29 Mayorov, A. S. *et al.* Micrometer-Scale Ballistic Transport in Encapsulated Graphene at Room Temperature. *Nano Letters* **11**, 2396-2399, doi:10.1021/nl200758b (2011).

30 Lee, C., Wei, X., Kysar, J. W. & Hone, J. Measurement of the Elastic Properties and Intrinsic Strength of Monolayer Graphene. *Science* **321**, 385, doi:10.1126/science.1157996 (2008).

31 Balandin, A. A. Thermal properties of graphene and nanostructured carbon materials. *Nature Materials* **10**, 569, doi:10.1038/nmat3064 (2011).

32 Lee, C., Wei, X., Kysar, J. W. & Hone, J. Measurement of the Elastic Properties and Intrinsic Strength of Monolayer Graphene. *Science* **321**, 385-388 (2008).

33 Fuhrer, M. S. & Hone, J. Measurement of mobility in dual-gated MoS2 transistors. *Nature Nanotechnology* **8**, 146, doi:10.1038/nnano.2013.30 (2013).

34 Mao, S. *et al.* Two-dimensional nanomaterial-based field-effect transistors for chemical and biological sensing. *Chemical Society Reviews* **46**, 6872-6904, doi:10.1039/C6CS00827E (2017).

35 Meric, I. *et al.* Current saturation in zero-bandgap, top-gated graphene field-effect transistors. *Nature Nanotechnology* **3**, 654, doi:10.1038/nnano.2008.268 (2008).

36 Chen, Y. *et al.* Towards flexible all-carbon electronics: Flexible organic field-effect transistors and inverter circuits using solution-processed all-graphene source/drain/gate electrodes. *Nano Research* **3**, 714-721, doi:10.1007/s12274-010-0035-3 (2010).

37 Cao, Y. *et al.* High-Performance Photoresponsive Organic Nanotransistors with Single-Layer Graphenes as Two-Dimensional Electrodes. *Advanced Functional Materials* **19**, 2743-2748, doi:10.1002/adfm.200900408 (2009).

38 Xia, J. L., Chen, F., Wiktor, P., Ferry, D. K. & Tao, N. J. Effect of Top Dielectric Medium on Gate Capacitance of Graphene Field Effect Transistors: Implications in Mobility Measurements and Sensor Applications. *Nano Letters* **10**, 5060-5064, doi:10.1021/nl103306a (2010).

39 Pince, E. & Kocabas, C. Investigation of high frequency performance limit of graphene field effect transistors. *Applied Physics Letters* **97**, 173106, doi:10.1063/1.3506506 (2010).

40 Zheng, Y. *et al.* Graphene Field-Effect Transistors with Ferroelectric Gating. *Physical Review Letters* **105**, 166602, doi:10.1103/PhysRevLett.105.166602 (2010).

41 Gomez De Arco, L. *et al.* Continuous, Highly Flexible, and Transparent Graphene Films by Chemical Vapor Deposition for Organic Photovoltaics. *ACS Nano* **4**, 2865-2873, doi:10.1021/nn901587x (2010).

42 Yin, Z. *et al.* Electrochemical Deposition of ZnO Nanorods on Transparent Reduced Graphene Oxide Electrodes for Hybrid Solar Cells. *Small* **6**, 307-312, doi:10.1002/smll.200901968 (2010).

43 Yan, X., Cui, X., Li, B. & Li, L.-s. Large, Solution-Processable Graphene Quantum Dots as Light Absorbers for Photovoltaics. *Nano Letters* **10**, 1869-1873, doi:10.1021/nl101060h (2010).

44 Wang, X., Zhi, L. & Müllen, K. Transparent, Conductive Graphene Electrodes for Dye-Sensitized Solar Cells. *Nano Letters* **8**, 323-327, doi:10.1021/nl072838r (2008).

45 Liu, Q. *et al.* Polymer Photovoltaic Cells Based on Solution-Processable Graphene and P3HT. *Advanced Functional Materials* **19**, 894-904, doi:10.1002/adfm.200800954 (2009).

46 Liu, Z. *et al.* Organic Photovoltaic Devices Based on a Novel Acceptor Material: Graphene. *Advanced Materials* **20**, 3924-3930, doi:10.1002/adma.200800366 (2008).

47 Guo, C. X. *et al.* Layered Graphene/Quantum Dots for Photovoltaic Devices. *Angewandte Chemie International Edition* **49**, 3014-3017, doi:10.1002/anie.200906291 (2010).

48 El-Kady, M. F., Strong, V., Dubin, S. & Kaner, R. B. Laser Scribing of High-Performance and Flexible Graphene-Based Electrochemical Capacitors. *Science* **335**, 1326, doi:10.1126/science.1216744 (2012).

49 Yang, X. *et al.* Graphene uniformly decorated with gold nanodots: in situ synthesis, enhanced dispersibility and applications. *Journal of Materials Chemistry* **21**, 8096-8103, doi:10.1039/C1JM10697J (2011).

50 Deng, M. *et al.* Electrochemical deposition of polypyrrole/graphene oxide composite on microelectrodes towards tuning the electrochemical properties of neural probes. *Sensors and Actuators B: Chemical* **158**, 176-184, (2011).

51 Xu, M., Fujita, D. & Hanagata, N. Perspectives and Challenges of Emerging Single-Molecule DNA Sequencing Technologies. *Small* **5**, 2638-2649, doi:10.1002/smll.200900976 (2009).

52 Garaj, S. *et al.* Graphene as a subnanometre trans-electrode membrane. *Nature* **467**, 190, doi:10.1038/nature09379 (2010).

53 Xu, M., Gao, Y., Yang, X. & Chen, H. Unique synthesis of graphene-based materials for clean energy and biological sensing applications. *Chinese Science Bulletin* **57**, 3000-3009, doi:10.1007/s11434-012-5128-9 (2012).

54 Nayak, T. R. *et al.* Graphene for Controlled and Accelerated Osteogenic Differentiation of Human Mesenchymal Stem Cells. *ACS Nano* **5**, 4670-4678, doi:10.1021/nn200500h (2011).

55 Leuschner, F. *et al.* Therapeutic siRNA silencing in inflammatory monocytes in mice. *Nature Biotechnology* **29**, 1005, doi:10.1038/nbt.1989 (2011).

56 Zhang, Y. *et al.* Cytotoxicity Effects of Graphene and Single-Wall Carbon Nanotubes in Neural Phaeochromocytoma-Derived PC12 Cells. *ACS Nano* **4**, 3181-3186, doi:10.1021/nn1007176 (2010).

57 Wojtoniszak, M. *et al.* Synthesis, dispersion, and cytocompatibility of graphene oxide and reduced graphene oxide. *Colloids and Surfaces B: Biointerfaces* **89**, 79-85, (2012).

58 Lu, C.-H. *et al.* Using graphene to protect DNA from cleavage during cellular delivery. *Chemical Communications* **46**, 3116-3118, doi:10.1039/B926893F (2010).

59 Liao, K.-H., Lin, Y.-S., Macosko, C. W. & Haynes, C. L. Cytotoxicity of Graphene Oxide and Graphene in Human Erythrocytes and Skin Fibroblasts. *ACS Applied Materials & Interfaces* **3**, 2607-2615, doi:10.1021/am200428v (2011).

60 Chang, Y. *et al.* In vitro toxicity evaluation of graphene oxide on A549 cells. *Toxicology Letters* **200**, 201-210, (2011).

61 Yuan, J. *et al.* Cytotoxicity Evaluation of Oxidized Single-Walled Carbon Nanotubes and Graphene Oxide on Human Hepatoma HepG2 cells: An iTRAQ-Coupled 2D LC-MS/MS Proteome Analysis. *Toxicological Sciences* **126**, 149-161, doi:10.1093/toxsci/kfr332 (2011).

62 Lee, Y. *et al.* Wafer-Scale Synthesis and Transfer of Graphene Films. *Nano Letters* **10**, 490-493, doi:10.1021/nl903272n (2010).

63 Chen, G. Y., Pang, D. W. P., Hwang, S. M., Tuan, H. Y. & Hu, Y. C. A graphene-based platform for induced pluripotent stem cells culture and differentiation. *Biomaterials* **33**, 418-427, (2012).

64 Park, S. Y. *et al.* Enhanced Differentiation of Human Neural Stem Cells into Neurons on Graphene. *Advanced Materials* **23**, H263-H267, doi:10.1002/adma.201101503 (2011).

65 Li, N. *et al.* The promotion of neurite sprouting and outgrowth of mouse hippocampal cells in culture by graphene substrates. *Biomaterials* **32**, 9374-9382, (2011).

66 Peng, C., Hu, W., Zhou, Y., Fan, C. & Huang, Q. Intracellular Imaging with a Graphene-Based Fluorescent Probe. *Small* **6**, 1686-1692, doi:10.1002/smll.201000560 (2010).

67 Gollavelli, G. & Ling, Y.-C. Multi-functional graphene as an in vitro and in vivo imaging probe. *Biomaterials* **33**, 2532-2545, (2012).

68 Sun, X. *et al.* Nano-Graphene Oxide for Cellular Imaging and Drug Delivery. *Nano research* **1**, 203-212, doi:10.1007/s12274-008-8021-8 (2008).

69 Liu, Z., Robinson, J. T., Sun, X. & Dai, H. PEGylated Nanographene Oxide for Delivery of Water-Insoluble Cancer Drugs. *Journal of the American Chemical Society* **130**, 10876-10877, doi:10.1021/ja803688x (2008).

70 McCormick, F. Cancer gene therapy: fringe or cutting edge? *Nature Reviews Cancer* **1**, 130, doi:10.1038/35101008 (2001).

71 Zhang, L. *et al.* Enhanced Chemotherapy Efficacy by Sequential Delivery of siRNA and Anticancer Drugs Using PEI-Grafted Graphene Oxide. *Small* **7**, 460-464, doi:10.1002/smll.201001522 (2011).

72 Zhou, X. *et al.* Strong Second-Harmonic Generation in Atomic Layered GaSe. *Journal of the American Chemical Society* **137**, 7994-7997, doi:10.1021/jacs.5b04305 (2015).

73 Keum, D. H. *et al.* Bandgap opening in few-layered monoclinic MoTe2. *Nature Physics* **11**, 482, doi:10.1038/nphys3314 (2015).

74 Ali, M. N. *et al.* Large, non-saturating magnetoresistance in WTe2. *Nature* **514**, 205, doi:10.1038/nature13763 (2014).

75 Pozo-Zamudio, O. D. *et al.* Photoluminescence of two-dimensional GaTe and GaSe films. *2D Materials* **2**, 035010, doi:10.1088/2053-1583/2/3/035010 (2015).

76 Tongay, S. *et al.* Monolayer behaviour in bulk ReS2 due to electronic and vibrational decoupling. *Nature Communications* **5**, 3252, doi:10.1038/ncomms4252 (2014).

77 Ataca, C., Şahin, H. & Ciraci, S. Stable, Single-Layer MX2 Transition-Metal Oxides and Dichalcogenides in a Honeycomb-Like Structure. *The Journal of Physical Chemistry C* **116**, 8983-8999, doi:10.1021/jp212558p (2012).

78 Kappera, R. *et al.* Metallic 1T phase source/drain electrodes for field effect transistors from chemical vapor deposited MoS2. *APL Materials* **2**, 092516, doi:10.1063/1.4896077 (2014).

79 Duerloo, K.-A. N., Li, Y. & Reed, E. J. Structural phase transitions in two-dimensional Mo- and W-dichalcogenide monolayers. *Nature Communications* **5**, 4214, doi:10.1038/ncomms5214 (2014).

80 Castellanos-Gomez, A. *et al.* Elastic Properties of Freely Suspended MoS2 Nanosheets. *Advanced Materials* **24**, 772-775, doi:10.1002/adma.201103965 (2012).

81 Suk, J. W., Piner, R. D., An, J. & Ruoff, R. S. Mechanical Properties of Monolayer Graphene Oxide. *ACS Nano* **4**, 6557-6564, doi:10.1021/nn101781v (2010).

82 Kalantar-zadeh, K. & Ou, J. Z. Biosensors Based on Two-Dimensional MoS2. *ACS Sensors* **1**, 5-16, doi:10.1021/acssensors.5b00142 (2016).

83 Chen, Y., Tan, C., Zhang, H. & Wang, L. Two-dimensional graphene analogues for biomedical applications. *Chemical Society Reviews* **44**, 2681-2701, doi:10.1039/C4CS00300D (2015).

84 Yang, G., Zhu, C., Du, D., Zhu, J. & Lin, Y. Graphene-like two-dimensional layered nanomaterials: applications in biosensors and nanomedicine. *Nanoscale* **7**, 14217-14231, doi:10.1039/C5NR03398E (2015).

85 Wang, N. *et al.* Synthesis of Strongly Fluorescent Molybdenum Disulfide Nanosheets for Cell-Targeted Labeling. *ACS Applied Materials & Interfaces* **6**, 19888-19894, doi:10.1021/am505305g (2014).

86 Chou, S. S. *et al.* Chemically Exfoliated MoS2 as Near-Infrared Photothermal Agents. *Angewandte Chemie International Edition* **52**, 4160-4164, doi:10.1002/anie.201209229 (2013).

87 Ji, Q., Zhang, Y., Zhang, Y. & Liu, Z. Chemical vapour deposition of group-VIB metal dichalcogenide monolayers: engineered substrates from amorphous to single crystalline. *Chemical Society Reviews* **44**, 2587-2602, doi:10.1039/C4CS00258J (2015).

88 Shi, Y., Li, H. & Li, L.-J. Recent advances in controlled synthesis of two-dimensional transition metal dichalcogenides via vapour deposition techniques. *Chemical Society Reviews* **44**, 2744-2756, doi:10.1039/C4CS00256C (2015).

89 Huang, X., Zeng, Z. & Zhang, H. Metal dichalcogenide nanosheets: preparation, properties and applications. *Chemical Society Reviews* **42**, 1934-1946, doi:10.1039/C2CS35387C (2013).

90 Liu, K.-K. *et al.* Growth of Large-Area and Highly Crystalline MoS2 Thin Layers on Insulating Substrates. *Nano Letters* **12**, 1538-1544, doi:10.1021/nl2043612 (2012).

91 Novoselov, K. S. & Castro Neto, A. H. Two-dimensional crystals-based heterostructures: materials with tailored properties. *Physica Scripta* **T146**, 014006, doi:10.1088/0031-8949/2012/t146/014006 (2012).

92 Mishra, A. K., Lakshmi, K. V. & Huang, L. Eco-friendly synthesis of metal dichalcogenides nanosheets and their environmental remediation potential driven by visible light. *Scientific Reports* **5**, 15718, doi:10.1038/srep15718 (2015).

93 Liu, T. *et al.* Drug Delivery with PEGylated MoS2 Nano-sheets for Combined Photothermal and Chemotherapy of Cancer. *Advanced Materials* **26**, 3433-3440, doi:10.1002/adma.201305256 (2014).

94 Benavente, E., Santa Ana, M. A., Mendizábal, F. & González, G. Intercalation chemistry of molybdenum disulfide. *Coordination Chemistry Reviews* **224**, 87-109, (2002).

95 Voiry, D. *et al.* Covalent functionalization of monolayered transition metal dichalcogenides by phase engineering. *Nature Chemistry* **7**, 45, doi:10.1038/nchem.2108

96 Jeong, S. *et al.* Tandem intercalation strategy for single-layer nanosheets as an effective alternative to conventional exfoliation processes. *Nature Communications* **6**, 5763, doi:10.1038/ncomms6763 (2015).

97 Pumera, M. Nanotoxicology: The Molecular Science Point of View. *Chemistry – An Asian Journal* **6**, 340-348, doi:10.1002/asia.201000398 (2011).

98 Teo, W. Z., Chng, E. L. K., Sofer, Z. & Pumera, M. Cytotoxicity of Exfoliated Transition-Metal Dichalcogenides (MoS2, WS2, and WSe2) is Lower Than That of Graphene and its Analogues. *Chemistry – A European Journal* **20**, 9627-9632, doi:10.1002/chem.201402680 (2014).

99 Qian, X., Shen, S., Liu, T., Cheng, L. & Liu, Z. Two-dimensional TiS2 nanosheets for in vivo photoacoustic imaging and photothermal cancer therapy. *Nanoscale* **7**, 6380-6387, doi:10.1039/C5NR00893J (2015).

100 Tian, B., Wang, C., Zhang, S., Feng, L. & Liu, Z. Photothermally Enhanced Photodynamic Therapy Delivered by Nano-Graphene Oxide. *ACS Nano* **5**, 7000-7009, doi:10.1021/nn201560b (2011).

101 Yong, Y. *et al.* WS2 nanosheet as a new photosensitizer carrier for combined photodynamic and photothermal therapy of cancer cells. *Nanoscale* **6**, 10394-10403, doi:10.1039/C4NR02453B (2014).

102 Lalwani, G. *et al.* Two-Dimensional Nanostructure-Reinforced Biodegradable Polymeric Nanocomposites for Bone Tissue Engineering. *Biomacromolecules* **14**, 900-909, doi:10.1021/bm301995s (2013).

103 Ajayan, P. M. & Tour, J. M. Nanotube composites. *Nature* **447**, 1066, doi:10.1038/4471066a (2007).

104 Wu, S. *et al.* Electrochemically Reduced Single-Layer MoS2 Nanosheets: Characterization, Properties, and Sensing Applications. *Small* **8**, 2264-2270, doi:10.1002/smll.201200044 (2012).

105 Hegab, H. M. *et al.* The controversial antibacterial activity of graphene-based materials. *Carbon* **105**, 362-376, (2016).

106 Henriques, P. C., Borges, I., Pinto, A. M., Magalhães, F. D. & Gonçalves, I. C. Fabrication and antimicrobial performance of surfaces integrating graphene-based materials. *Carbon* **132**, 709-732, (2018).

107 Karahan, H. E. *et al.* Graphene Materials in Antimicrobial Nanomedicine: Current Status and Future Perspectives. *Advanced Healthcare Materials* **7**, 1701406, doi:10.1002/adhm.201701406 (2018).

108 Zheng, H. *et al.* Antibacterial applications of graphene oxides: structure-activity relationships, molecular initiating events and biosafety. *Science Bulletin* **63**, 133-142, (2018).

109 Hu, W. *et al.* Graphene-Based Antibacterial Paper. *ACS Nano* **4**, 4317-4323, doi:10.1021/nn101097v (2010).

110 Akhavan, O. & Ghaderi, E. Toxicity of Graphene and Graphene Oxide Nanowalls Against Bacteria. *ACS Nano* **4**, 5731-5736, doi:10.1021/nn101390x (2010).

111 Mangadlao, J. D. *et al.* On the antibacterial mechanism of graphene oxide (GO) Langmuir–Blodgett films. *Chemical Communications* **51**, 2886-2889, doi:10.1039/C4CC07836E (2015).

112 Hui, L. *et al.* Availability of the Basal Planes of Graphene Oxide Determines Whether It Is Antibacterial. *ACS Applied Materials & Interfaces* **6**, 13183-13190, doi:10.1021/am503070z (2014).

113 Liu, S. *et al.* Lateral Dimension-Dependent Antibacterial Activity of Graphene Oxide Sheets. *Langmuir* **28**, 12364-12372, doi:10.1021/la3023908 (2012).

114 Tu, Y. *et al.* Destructive extraction of phospholipids from Escherichia coli membranes by graphene nanosheets. *Nature Nanotechnology* **8**, 594, doi:10.1038/nnano.2013.125 (2013).

115 Dallavalle, M., Calvaresi, M., Bottoni, A., Melle-Franco, M. & Zerbetto, F. Graphene Can Wreak Havoc with Cell Membranes. *ACS Applied Materials & Interfaces* **7**, 4406-4414, doi:10.1021/am508938u (2015).

116 Perreault, F., de Faria, A. F., Nejati, S. & Elimelech, M. Antimicrobial Properties of Graphene Oxide Nanosheets: Why Size Matters. *ACS Nano* **9**, 7226-7236, doi:10.1021/acsnano.5b02067 (2015).

117 Krishnamoorthy, K. N, Umasuthan, R. Mohan, J. Lee, and SJ Kim. *Sci. Adv. Mater* **4**, 1111 (2012).

118 Gurunathan, S., Han, J. W., Dayem, A. A., Eppakayala, V. & Kim, J.-H. Oxidative stress-mediated antibacterial activity of graphene oxide and reduced graphene oxide in Pseudomonas aeruginosa. *International journal of nanomedicine* **7**, 5901-5914, doi:10.2147/IJN.S37397 (2012).

119 Gurunathan, S. *et al.* Antibacterial activity of dithiothreitol reduced graphene oxide. *Journal of Industrial and Engineering Chemistry* **19**, 1280-1288, (2013).

120 Liu, S. *et al.* Antibacterial Activity of Graphite, Graphite Oxide, Graphene Oxide, and Reduced Graphene Oxide: Membrane and Oxidative Stress. *ACS Nano* **5**, 6971-6980, doi:10.1021/nn202451x (2011).

121 Panda, S., Rout, T. K., Prusty, A. D., Ajayan, P. M. & Nayak, S. Electron Transfer Directed Antibacterial Properties of Graphene Oxide on Metals. *Advanced Materials* **30**, 1702149, doi:10.1002/adma.201702149 (2018).

122 Shahnawaz Khan, M., Abdelhamid, H. N. & Wu, H.-F. Near infrared (NIR) laser mediated surface activation of graphene oxide nanoflakes for efficient antibacterial, antifungal and wound healing treatment. *Colloids and Surfaces B: Biointerfaces* **127**, 281-291, (2015).

123 Wang, Y.-W. *et al.* Targeted photothermal ablation of pathogenic bacterium, Staphylococcus aureus, with nanoscale reduced graphene oxide. *Journal of Materials Chemistry B* **1**, 2496-2501, doi:10.1039/C3TB20144A (2013).

124 Qian, W. *et al.* pH-triggered charge-reversible of glycol chitosan conjugated carboxyl graphene for enhancing photothermal ablation of focal infection. *Acta Biomaterialia* **69**, 256-264, (2018)

125 Zou, X., Zhang, L., Wang, Z. & Luo, Y. Mechanisms of the Antimicrobial Activities of Graphene Materials. *Journal of the American Chemical Society* **138**, 2064-2077, doi:10.1021/jacs.5b11411 (2016).

126 Yang, X. *et al.* Antibacterial activity of two-dimensional MoS2 sheets. *Nanoscale* **6**, 10126-10133, doi:10.1039/C4NR01965B (2014).

127 Wu, N. *et al.* Investigating the Influence of MoS2 Nanosheets on E. coli from Metabolomics Level. *PLOS ONE* **11**, e0167245, doi:10.1371/journal.pone.0167245 (2016).

128 Tang, K. *et al.* Molybdenum disulfide (MoS2) nanosheets vertically coated on titanium for disinfection in the dark. *Arabian Journal of Chemistry*, (2017).

129 Kim, T. I. *et al.* Antibacterial Activities of Graphene Oxide–Molybdenum Disulfide Nanocomposite Films. *ACS Applied Materials & Interfaces* **9**, 7908-7917, doi:10.1021/acsami.6b12464 (2017).

130 Pal, A. *et al.* MoS2-TiO2 Nanocomposite with Excellent Adsorption Performance and High Antibacterial Activity. *ChemistrySelect* **3**, 81-90, doi:10.1002/slct.201702618 (2018).

131 Pandit, S., Karunakaran, S., Boda, S. K., Basu, B. & De, M. High Antibacterial Activity of Functionalized Chemically Exfoliated MoS2. *ACS Applied Materials & Interfaces* **8**, 31567-31573, doi:10.1021/acsami.6b10916 (2016).

132 Cao, F. *et al.* An Efficient and Benign Antimicrobial Depot Based on Silver-Infused MoS2. *ACS Nano* **11**, 4651-4659, doi:10.1021/acsnano.7b00343 (2017).

133 Zhang, X. *et al.* Antibiotic-loaded MoS2nanosheets to combat bacterial resistance via biofilm inhibition. *Nanotechnology* **28**, 225101, doi:10.1088/1361-6528/aa6c9b (2017).

134 Liu, C. *et al.* Rapid water disinfection using vertically aligned MoS2 nanofilms and visible light. *Nature Nanotechnology* **11**, 1098, doi:10.1038/nnano.2016.138 (2016).

135 Yin, W. *et al.* Functionalized Nano-MoS2 with Peroxidase Catalytic and Near-Infrared Photothermal Activities for Safe and Synergetic Wound Antibacterial Applications. *ACS Nano* **10**, 11000-11011, doi:10.1021/acsnano.6b05810 (2016).

136 Huang, X.-W. *et al.* Silk fibroin-assisted exfoliation and functionalization of transition metal dichalcogenide nanosheets for antibacterial wound dressings. *Nanoscale* **9**, 17193-17198, doi:10.1039/C7NR06807G (2017).

137 Navale, G. R. *et al.* Oxidative and membrane stress-mediated antibacterial activity of WS2 and rGO-WS2 nanosheets. *RSC Advances* **5**, 74726-74733, doi:10.1039/C5RA15652A (2015).

138 Zhang, W. *et al.* Versatile molybdenum disulfide based antibacterial composites for in vitro enhanced sterilization and in vivo focal infection therapy. *Nanoscale* **8**, 11642-11648, doi:10.1039/C6NR01243D (2016).

139 Rasool, K. *et al.* Antibacterial Activity of Ti3C2Tx MXene. *ACS Nano* **10**, 3674-3684, doi:10.1021/acsnano.6b00181 (2016).

140 Rasool, K. *et al.* Efficient Antibacterial Membrane based on Two-Dimensional Ti3C2Tx (MXene) Nanosheets. *Scientific Reports* **7**, 1598, doi:10.1038/s41598-017-01714-3 (2017).

141 Pandey, R. P. *et al.* Ultrahigh-flux and fouling-resistant membranes based on layered silver/MXene (Ti3C2Tx) nanosheets. *Journal of Materials Chemistry A* **6**, 3522-3533, doi:10.1039/C7TA10888E (2018).

142 Centers for Disease, C. & Prevention. CDC Grand Rounds: the growing threat of multidrug-resistant gonorrhea. *MMWR Morb Mortal Wkly Rep* **62**, 103-106 (2013).

143 Hu, W. *et al.* Graphene-based antibacterial paper. *ACS Nano* **4**, 4317-4323, doi:10.1021/nn101097v (2010).

144 Ristic, B. Z. *et al.* Photodynamic antibacterial effect of graphene quantum dots. *Biomaterials* **35**, 4428-4435, doi:10.1016/j.biomaterials.2014.02.014 (2014).

145 Kurapati, R. *et al.* Enzymatic Biodegradability of Pristine and Functionalized Transition Metal Dichalcogenide MoS2 Nanosheets. *Advanced Functional Materials* **27**, doi:ARTN 1605176(2017).

146 Yang, X. *et al.* Antibacterial activity of two-dimensional MoS2 sheets. *Nanoscale* **6**, 10126-10133, doi:10.1039/c4nr01965b (2014).

147 Bang, G. S. *et al.* DNA-Assisted Exfoliation of Tungsten Dichalcogenides and Their Antibacterial Effect. *Acs Applied Materials & Interfaces* **8**, 1943-1950, doi:10.1021/acsami.5b10136 (2016).

148 Liu, C. *et al.* Rapid water disinfection using vertically aligned MoS2 nanofilms and visible light. *Nature Nanotechnology* **11**, 1098-1104, doi:10.1038/Nnano.2016.138 (2016).

149 Becker, M. L. *et al.* Length-dependent uptake of DNA-wrapped single-walled carbon nanotubes. *Advanced Materials* **19**, 939-+, doi:10.1002/adma.200602667 (2007).

150 D'yachkov, E. P., Dolin, S. P. & D'yachkov, P. N. Interaction of single-stranded DNA with carbon nanotubes according to the molecular docking method. *Doklady Physical Chemistry* **423**, 297-301, doi:10.1134/S0012501608110031 (2008).

151 Dovbeshko, G. I., Repnytska, O. P., Obraztsova, E. D. & Shtogun, Y. V. DNA interaction with single-walled carbon nanotubes: a SEIRA study. *Chemical Physics Letters* **372**, 432-437, doi:10.1016/S0009-2614(03)00429-9 (2003).

152 Gladchenko, G. O. *et al.* Interaction of fragmented double-stranded DNA with carbon nanotubes in aqueous solution. *Molecular Physics* **104**, 3193-3201, doi:10.1080/00268970601061220 (2006).

153 Iliafar, S., Mittal, J., Vezenov, D. & Jagota, A. Interaction of Single-Stranded DNA with Curved Carbon Nanotube Is Much Stronger Than with Flat Graphite. *Journal of the American Chemical Society* **136**, 12947-12957, doi:10.1021/ja5055498 (2014).

154 Lu, G., Maragakis, P. & Kaxiras, E. Carbon nanotube interaction with DNA. *Nano Letters* **5**, 897-900, doi:10.1021/nl050354u (2005).

155 Meng, S., Maragakis, P., Papaloukas, C. & Kaxiras, E. DNA nucleoside interaction and identification with carbon nanotubes. *Nano Letters* **7**, 45-50, doi:10.1021/nl0619403 (2007).

156 Staii, C. & Johnson, A. T. DNA-decorated carbon nanotubes for chemical sensing. *Nano Letters* **5**, 1774-1778, doi:10.1021/nl051261f (2005).

157 Zheng, M. *et al.* DNA-assisted dispersion and separation of carbon nanotubes. *Nature Materials* **2**, 338-342, doi:10.1038/nmat877 (2003).

158 Hu, W. B. *et al.* Graphene-Based Antibacterial Paper. *Acs Nano* **4**, 4317-4323, doi:10.1021/nn101097v (2010).

159 Li, J. H. *et al.* Antibacterial activity of large-area monolayer graphene film manipulated by charge transfer. *Scientific Reports* **4**, doi:ARTN 4359 10.1038/srep04359 (2014).

160 Liu, S. B. *et al.* Antibacterial Activity of Graphite, Graphite Oxide, Graphene Oxide, and Reduced Graphene Oxide: Membrane and Oxidative Stress. *Acs Nano* **5**, 6971-6980, doi:10.1021/nn202451x (2011).

161 Rasool, K. *et al.* Efficient Antibacterial Membrane based on Two-Dimensional Ti3C2Tx (MXene) Nanosheets. *Scientific Reports* **7**, doi:ARTN 1598 10.1038/s41598-017-01714-3 (2017).

162 Mansukhani, N. D. *et al.* High-Concentration Aqueous Dispersions of Nanoscale 2D Materials Using Nonionic, Biocompatible Block Copolymers. *Small* **12**, 294-300, doi:10.1002/smll.201503082 (2016).

163 Zhang, L., Xu, B. & Wang, X. Cholesterol Extraction from Cell Membrane by Graphene Nanosheets: A Computational Study. *J Phys Chem B* **120**, 957-964, doi:10.1021/acs.jpcb.5b10330 (2016).

164 Tu, Y. *et al.* Destructive extraction of phospholipids from Escherichia coli membranes by graphene nanosheets. *Nat Nanotechnol* **8**, 594-601, doi:10.1038/nnano.2013.125 (2013).

165 Tanouchi, Y., Lee, A. J., Meredith, H. & You, L. Programmed cell death in bacteria and implications for antibiotic therapy. *Trends in microbiology* **21**, 265-270, doi:10.1016/j.tim.2013.04.001 (2013).

166 Žgur-Bertok, D. DNA Damage Repair and Bacterial Pathogens. *PLOS Pathogens* **9**, e1003711, doi:10.1371/journal.ppat.1003711 (2013).

167 Kleanthous, C. & Armitage, J. P. The bacterial cell envelope. *Philos Trans R Soc Lond B Biol Sci* **370**, doi:10.1098/rstb.2015.0019 (2015).

168 Lam, S. J. *et al.* Combating multidrug-resistant Gram-negative bacteria with structurally nanoengineered antimicrobial peptide polymers. *Nature Microbiology* **1**, 16162, doi:10.1038/nmicrobiol.2016.162 (2016).

169 Rice, Louis B. Federal Funding for the Study of Antimicrobial Resistance in Nosocomial Pathogens: No ESKAPE. *The journal of infectious diseases.* **197**, 1079-1081, doi:10.1086/533452 (2008).

170 Rice, L. B. Progress and Challenges in Implementing the Research on ESKAPE Pathogens. *Infection control and hospital epidemiology.* **31**, S7-S10, doi:10.1086/655995 (2010).

171 Gross, M. Antibiotics in crisis. *Current Biology* **23**, R1063-R1065, (2013).

172 Giske, C. G., Monnet, D. L., Cars, O. & Carmeli, Y. Clinical and Economic Impact of Common Multidrug-Resistant Gram-Negative Bacilli. *Antimicrobial Agents and Chemotherapy* **52**, 813, doi:10.1128/AAC.01169-07 (2008).

173 van Duin, D. & Paterson, D. L. Multidrug-Resistant Bacteria in the Community: Trends and Lessons Learned. *Infectious disease clinics of North America* **30**, 377-390, doi:10.1016/j.idc.2016.02.004 (2016).

174 Friedman, N. D., Temkin, E. & Carmeli, Y. The negative impact of antibiotic resistance. *Clinical Microbiology and Infection* **22**, 416-422, (2016).

175 Ventola, C. L. The antibiotic resistance crisis: part 1: causes and threats. *P & T : a peer-reviewed journal for formulary management* **40**, 277-283 (2015).

176 Taubes, G. The bacteria fight back. *Science.* **321**, 356-361, doi:10.1126/science.321.5887.356 (2008).

177 Lee, J. H., Jeong, S. H., Cha, S.-S. & Lee, S. H. A lack of drugs for antibiotic-resistant Gram-negative bacteria. *Nature reviews.* **6**, 938-938, doi:10.1038/nrd2201-c1 (2007).

178 Xu, Z.-Q., Flavin, M. T. & Flavin, J. Combating multidrug-resistant Gram-negative bacterial infections. *Expert Opinion on Investigational Drugs* **23**, 163-182, doi:10.1517/13543784.2014.848853 (2014).

179 Fair, R. J. & Tor, Y. Antibiotics and bacterial resistance in the 21st century. *Perspectives in medicinal chemistry* **6**, 25-64, doi:10.4137/PMC.S14459 (2014).

180 Kohanski, M. A., Dwyer, D. J. & Collins, J. J. How antibiotics kill bacteria: from targets to networks. *Nature reviews.* **8**, 423-435, doi:10.1038/nrmicro2333 (2010).

181 Taylor, P. W., Stapleton, P. D. & Paul Luzio, J. New ways to treat bacterial infections. *Drug Discovery Today* **7**, 1086-1091, (2002).

182 Brogden, K. A. Antimicrobial peptides: pore formers or metabolic inhibitors in bacteria? *Nature reviews.* **3**, 238-250, doi:10.1038/nrmicro1098 (2005).

183 Gupta, A. *et al.* Engineered Polymer Nanoparticles with Unprecedented Antimicrobial Efficacy and Therapeutic Indices against Multidrug-Resistant Bacteria and Biofilms. *Journal of the American Chemical Society* **140**, 12137-12143, doi:10.1021/jacs.8b06961 (2018).

184 Gupta, A., Mumtaz, S., Li, C.-H., Hussain, I. & Rotello, V. M. Combatting antibiotic-resistant bacteria using nanomaterials. *Chemical Society Reviews* **48**, 415-427, doi:10.1039/C7CS00748E (2019).

185 Zasloff, M. Antimicrobial peptides of multicellular organisms. *Nature.* **415**, 389-395, doi:10.1038/415389a (2002).

186 de Breij, A. *et al.* The antimicrobial peptide SAAP-148 combats drug-resistant bacteria and biofilms. *Science Translational Medicine* **10**, eaan4044, doi:10.1126/scitranslmed.aan4044 (2018).

187 Palermo, E. F. & Kuroda, K. Structural determinants of antimicrobial activity in polymers which mimic host defense peptides. *Applied Microbiology and Biotechnology* **87**, 1605-1615, doi:10.1007/s00253-010-2687-z (2010).

188 Kuroda, K. & DeGrado, W. F. Amphiphilic Polymethacrylate Derivatives as Antimicrobial Agents. *Journal of the American Chemical Society* **127**, 4128-4129, doi:10.1021/ja044205+ (2005).

189 Kang, S.-J., Park, S. J., Mishig-Ochir, T. & Lee, B.-J. Antimicrobial peptides: therapeutic potentials. *Expert Review of Anti-infective Therapy* **12**, 1477-1486, doi:10.1586/14787210.2014.976613 (2014).

190 Huh, A. J. & Kwon, Y. J. "Nanoantibiotics": A new paradigm for treating infectious diseases using nanomaterials in the antibiotics resistant era. *Journal of controlled release* **156**, 128-145, doi:10.1016/j.jconrel.2011.07.002 (2011).

191 Li, Q. *et al.* Antimicrobial nanomaterials for water disinfection and microbial control: Potential applications and implications. *Water Research* **42**, 4591-4602, (2008).

192 Weir, E., Lawlor, A., Whelan, A. & Regan, F. The use of nanoparticles in anti-microbial materials and their characterization. *Analyst* **133**, 835-845, doi:10.1039/B715532H (2008).

193 Huang, Z. *et al.* Toxicological Effect of ZnO Nanoparticles Based on Bacteria. *Langmuir* **24**, 4140-4144, doi:10.1021/la7035949 (2008).

194 Maness, P. C. *et al.* Bactericidal activity of photocatalytic TiO(2) reaction: toward an understanding of its killing mechanism. *Applied and environmental microbiology.* **65**, 4094-4098 (1999).

195 Kim, J. S. *et al.* Antimicrobial effects of silver nanoparticles. *Nanomedicine: Nanotechnology, Biology and Medicine* **3**, 95-101, (2007).

196 Ding, X., Duan, S., Ding, X., Liu, R. & Xu, F.-J. Versatile Antibacterial Materials: An Emerging Arsenal for Combatting Bacterial Pathogens. *Advanced Functional Materials* **28**, 1802140, doi:10.1002/adfm.201802140 (2018).

197 Hale, J. D. F. & Hancock, R. E. W. Alternative mechanisms of action of cationic antimicrobial peptides on bacteria. *Expert Review of Anti-infective Therapy* **5**, 951-959, doi:10.1586/14787210.5.6.951 (2007).

198 Findlay, B., Zhanel, G. G. & Schweizer, F. Cationic Amphiphiles, a New Generation of Antimicrobials Inspired by the Natural Antimicrobial Peptide Scaffold. *Antimicrobial Agents and Chemotherapy* **54**, 4049, doi:10.1128/AAC.00530-10 (2010).

199 Powers, J.-P. S. & Hancock, R. E. W. The relationship between peptide structure and antibacterial activity. *Peptides* **24**, 1681-1691, (2003).

200 Martens, E. & Demain, A. L. The antibiotic resistance crisis, with a focus on the United States. *The Journal Of Antibiotics* **70**, 520, doi:10.1038/ja.2017.30 (2017).

201 Boucher, Helen W. *et al.* Bad Bugs, No Drugs: No ESKAPE! An Update from the Infectious Diseases Society of America. *Clinical infectious diseases.* **48**, 1-12, doi:10.1086/595011 (2009).

202 Campos, M. A. *et al.* Capsule Polysaccharide Mediates Bacterial Resistance to Antimicrobial Peptides. *Infection and Immunity* **72**, 7107, doi:10.1128/IAI.72.12.7107-7114.2004 (2004).

203 Llobet, E., Tomas, J. M. & Bengoechea, J. A. Capsule polysaccharide is a bacterial decoy for antimicrobial peptides. *Microbiology.* **154**, 3877-3886, doi:10.1099/mic.0.2008/022301-0 (2008).

204 Bonnier, F. *et al.* Cell viability assessment using the Alamar blue assay: A comparison of 2D and 3D cell culture models. *Toxicology in Vitro* **29**, 124-131, (2015).

205 Parameswaran, N. & Patial, S. Tumor necrosis factor-α signaling in macrophages. *Critical reviews in eukaryotic gene expression* **20**, 87-103 (2010).

206 Flemming, H.-C. & Wingender, J. The biofilm matrix. *Nature reviews.* **8**, 623-633, doi:10.1038/nrmicro2415 (2010).

207 Stewart, P. S. Mechanisms of antibiotic resistance in bacterial biofilms. *International journal of medical microbiology : IJMM* **292**, 107-113, doi:10.1078/1438-4221-00196 (2002).

208 Olsen, I. Biofilm-specific antibiotic tolerance and resistance. *European Journal of Clinical Microbiology & Infectious Diseases* **34**, 877-886, doi:10.1007/s10096-015-2323-z (2015).

209 Gerdes, K. & Semsey, S. Pumping persisters. *Nature.* **534**, 41-42, doi:10.1038/nature18442 (2016).

210 Landis, R. F. *et al.* Biodegradable Nanocomposite Antimicrobials for the Eradication of Multidrug-Resistant Bacterial Biofilms without Accumulated Resistance. *Journal of the American Chemical Society* **140**, 6176-6182, doi:10.1021/jacs.8b03575 (2018).

211 Novo, D., Perlmutter, N. G., Hunt, R. H. & Shapiro, H. M. Accurate flow cytometric membrane potential measurement in bacteria using diethyloxacarbocyanine and a ratiometric technique. *Cytometry* **35**, 55-63, doi:10.1002/(SICI)1097-0320(19990101)35:1<55::AID-CYTO8>3.0.CO;2-2 (1999).

212 Liu, L. *et al.* Self-assembled cationic peptide nanoparticles as an efficient antimicrobial agent. *Nature Nanotechnology* **4**, 457, doi:10.1038/nnano.2009.153 (2009).

APPENDIX A

SUPPORTING INFORMATION

Supplementary Information

Chapter 3

Elimination of Multidrug Resistant Bacteria by Transition Metal Dichalcogenides Encapsulated by Synthetic Single-Stranded DNA

Cell viability of $MoSe_2/T_{20}$

Figure A1 shows the biocompatibility of $MoSe_2/T_{20}$ tested on human carcinoma cells, *HeLa cells* and determined using MTT assays. The cellular viability studies showed 100% cell viability at all the tested concentrations, with a concentration as high as 250 µg/ml.

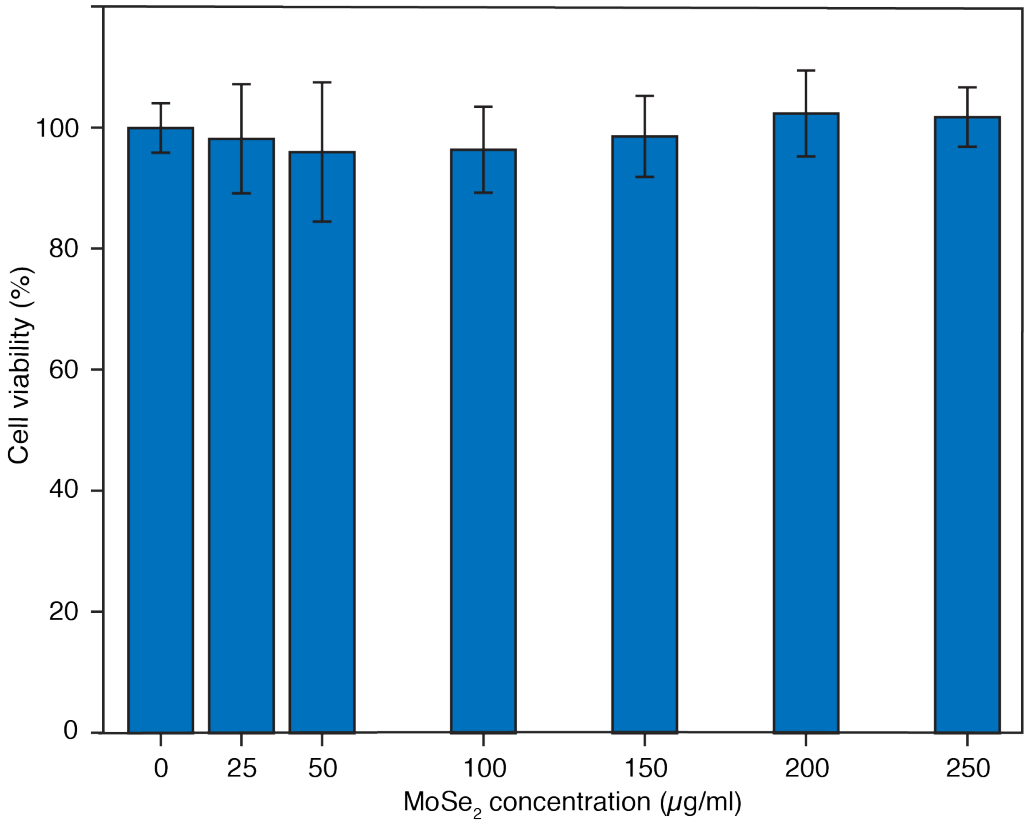

Figure A 1: Biocompatibility study of $MoSe_2/T_{20}$ tested on human carcinoma cells, *HeLa* at a concentration ranging from 0 to 250 µg/ml.

Bacterial viability in different medium

Figure A 2 shows, *E. coli* K12 MG1655 viability determined in four different media, minimal essential medium (MEM), 1x PBS, M9 medium and water. The overnight bacterial culture was centrifuged, and re-dispersed in four different medium and bacterial viability was determined using colony counting method. The bacterial viability shows no significant effect of medium on cellular viability after 4 hours incubations.

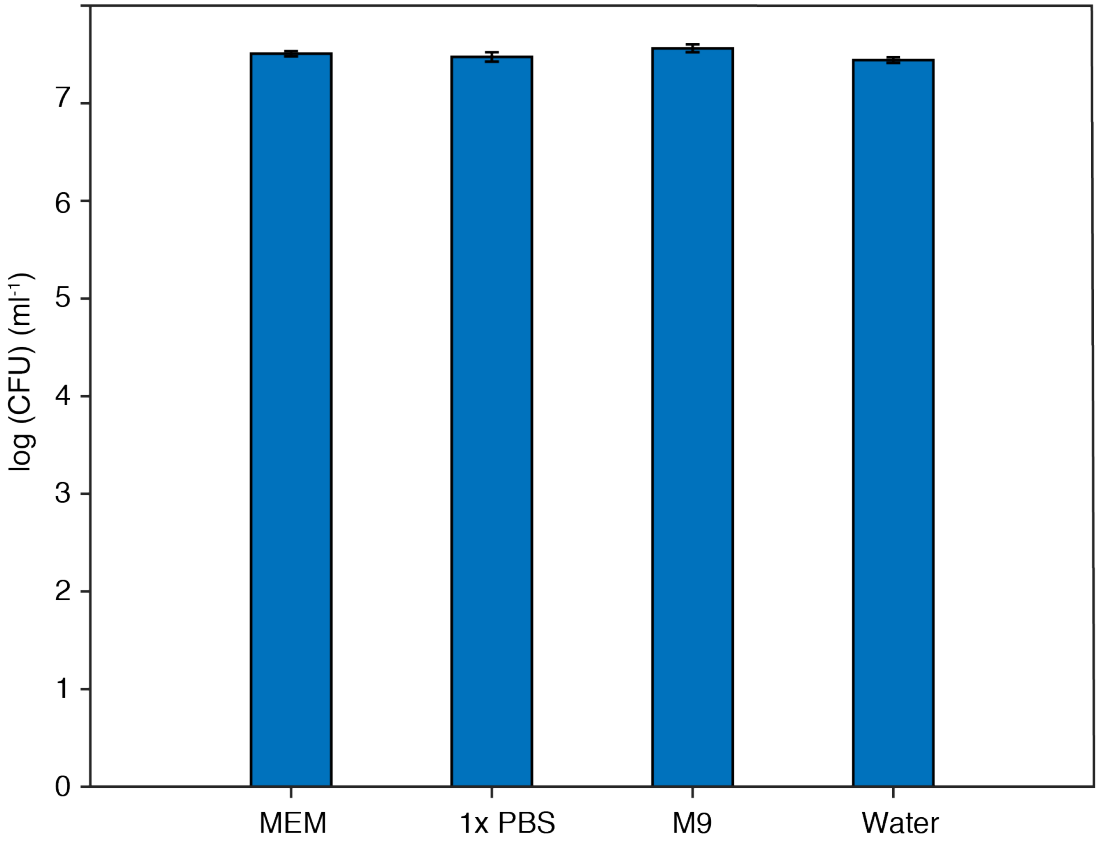

Figure A 2: Bacterial viability of DH5α after incubations at four different medium, water, 1x PBS, 1x MEM and 1x M9.

Zeta potential of four different TMDCs dispersed in single-stranded T_{20}

Figure A 3 shows, the stability of TMDCs dispersed in T_{20}, determined using zeta potential. The zeta potential of $MoSe_2/T_{20,}$ WSe_2/ T_{20}, MoS_2/ T_{20} and WS_2/ T_{20} was -42.1 mV, -39.8 mV, -21.3 mV and -19.8 mV. Based on zeta potential, $MoSe_2/T_{20,}$ WSe_2/ T_{20} was most stable whereas MoS_2/ T_{20} and WS_2/ T_{20} was least stable.

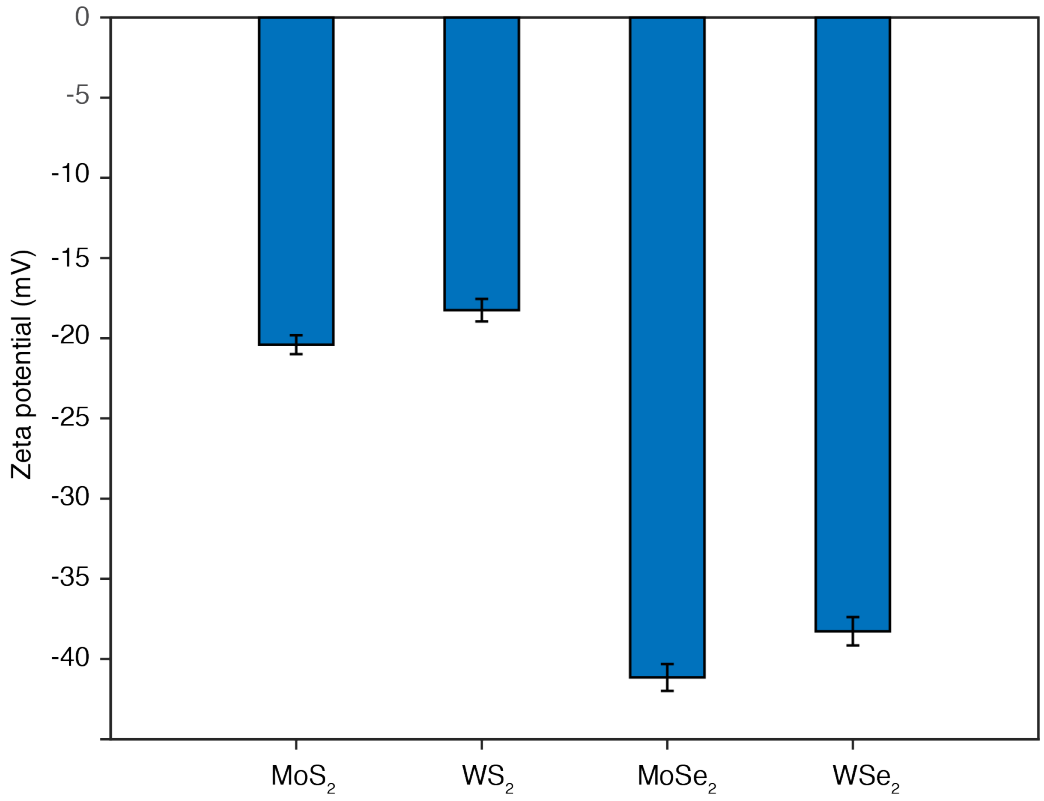

Figure A 3: Zeta potential of TMDCs dispersed in synthetic single-stranded synthetic DNA sequence T_{20}

Thermogravimetric analysis (TGA) of $MoSe_2$ dispersed in T_{20}

Figure A 4 shows the amount of DNA present on the surface of $MoSe_2$, which was analyzed using TGA. The TGA analysis of $MoSe_2/T_{20}$ showed presence of 8% DNA on the surface of $MoSe_2$.

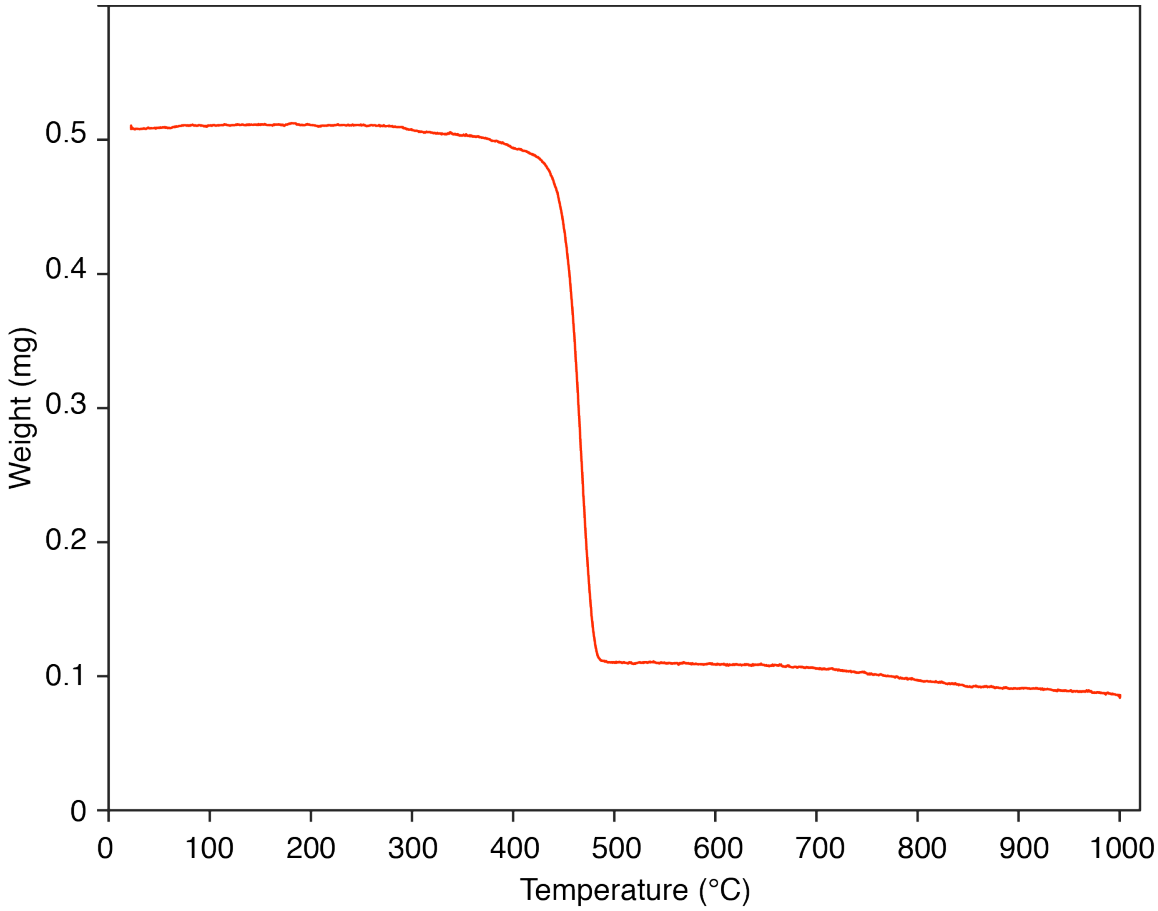

Figure A 4: Thermogravimetric analysis of $MoSe_2$ dispersed in single-stranded T_{20}.The TGA curve shows the change in weight with respect to temperature, showing degradation at 500 °C.

Microscopic evaluation of antibacterial activity of $MoSe_2/(GT)_{10}$

Figure A 5 shows, the change in morphology *E. coli*, K12 MG1655 of $MoSe_2/(GT)_{10}$, after interactions with nanosheets. SEM images of bacteria demonstrates change in bacterial morphology after interaction with $MoSe_2/(GT)_{10}$ nanosheets. The SEM images shows formation of small blob like structure on cell membrane after interaction with 0.5x MBC of $MoSe_2/(GT)_{10}$ nanosheets and it shows broken cell membrane at 1x MBC. The TEM images of bacteria shows no change in cytoplasm for control samples, whereas it shows change in cytoplasm at 0.5x MBC and 1x MBC

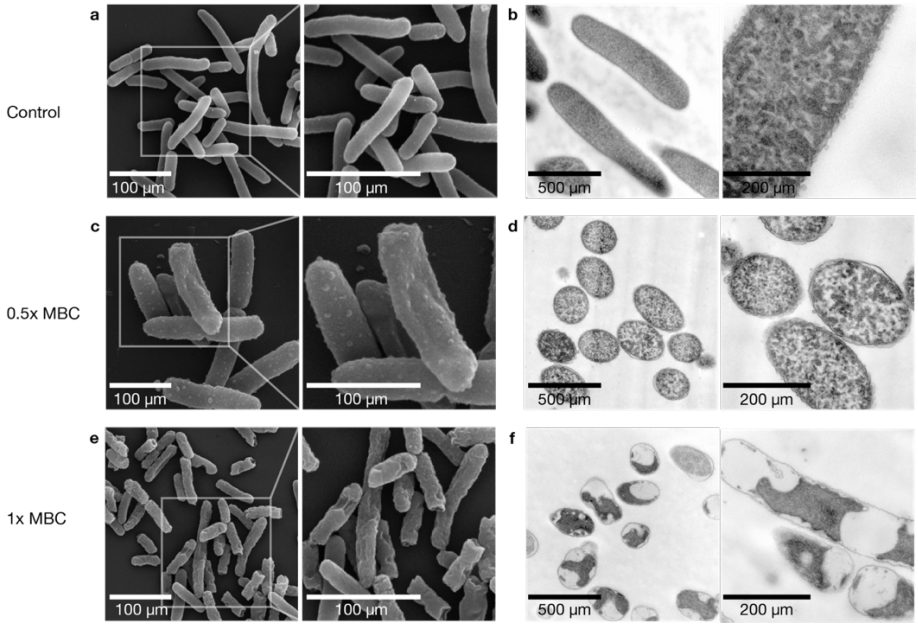

Figure A 5: Microscopic evaluation of *E. coli* (a, c, e) SEM images of *E. coli* after interactions with $MoSe_2/(GT)_{10}$ nanosheets (b, d, e) TEM images of *E. coli* after interactions with $MoSe_2/(GT)_{10}$ nanosheets.

APPENDIX B

SUPPORTING INFORMATION

Supplementary information

Chapter 4

Eradication of multidrug-resistant bacteria using two-dimensional material based nanohybrid structures

Zeta potential of $MoSe_2$/PL and $MoSe_2$/PLL/Pluronic-F77

Figure B 1 shows, the change in zeta potential from $MoSe_2$/PL to $MoSe_2$/PL/F77 structure. The zeta potential changes from +41.4 mV to +21.4 mV, which clearly shows a formation of hybrid structure of $MoSe_2$, PLL and Pluronic F77

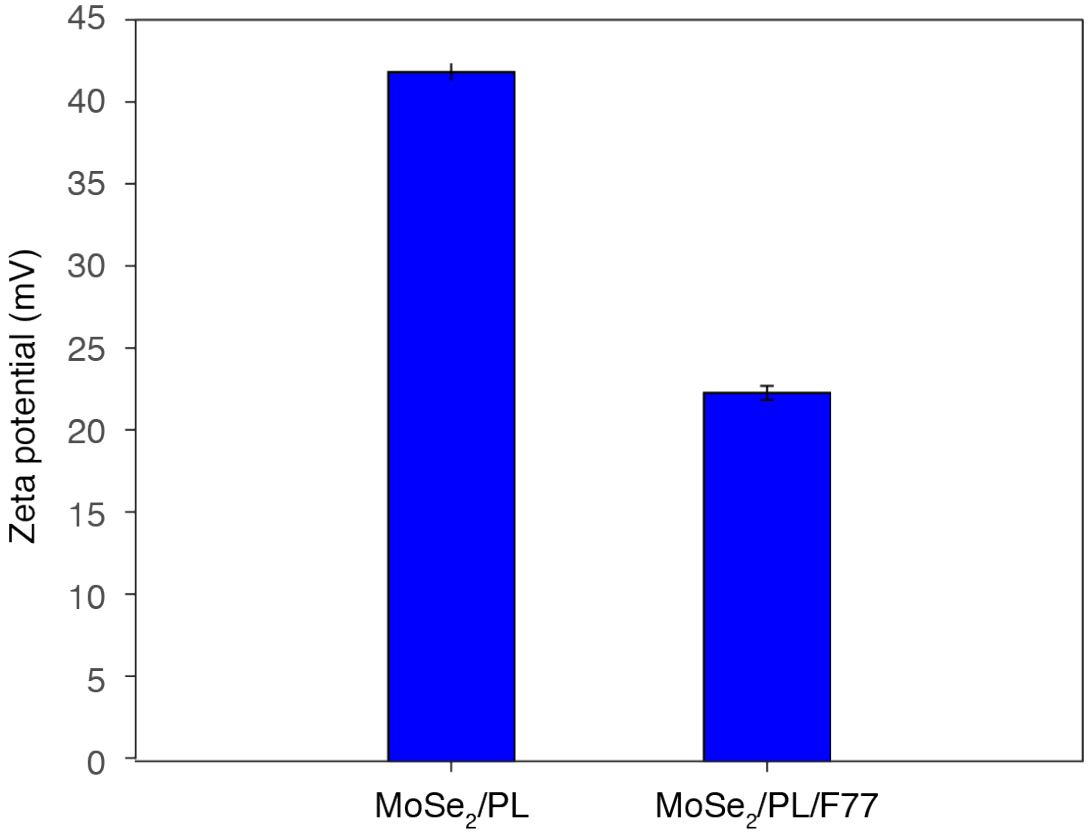

Figure B 1: The zeta potential measurement of $MoSe_2$/PL and $MoSe_2$/PL/F77. The change in zeta potential clearly shows the replacement of PLL with Pluronic-F77

Thermogravimetric analysis of MoSe2/PLL/Pluronic-F77

Figure B 2 shows, the thermogravimetric analysis of $MoSe_2$/PL/F77 systems to determine the content of polymer with respect to $MoSe_2$. The TGA analysis demonstrates 22% polymer on the surface of $MoSe_2$.

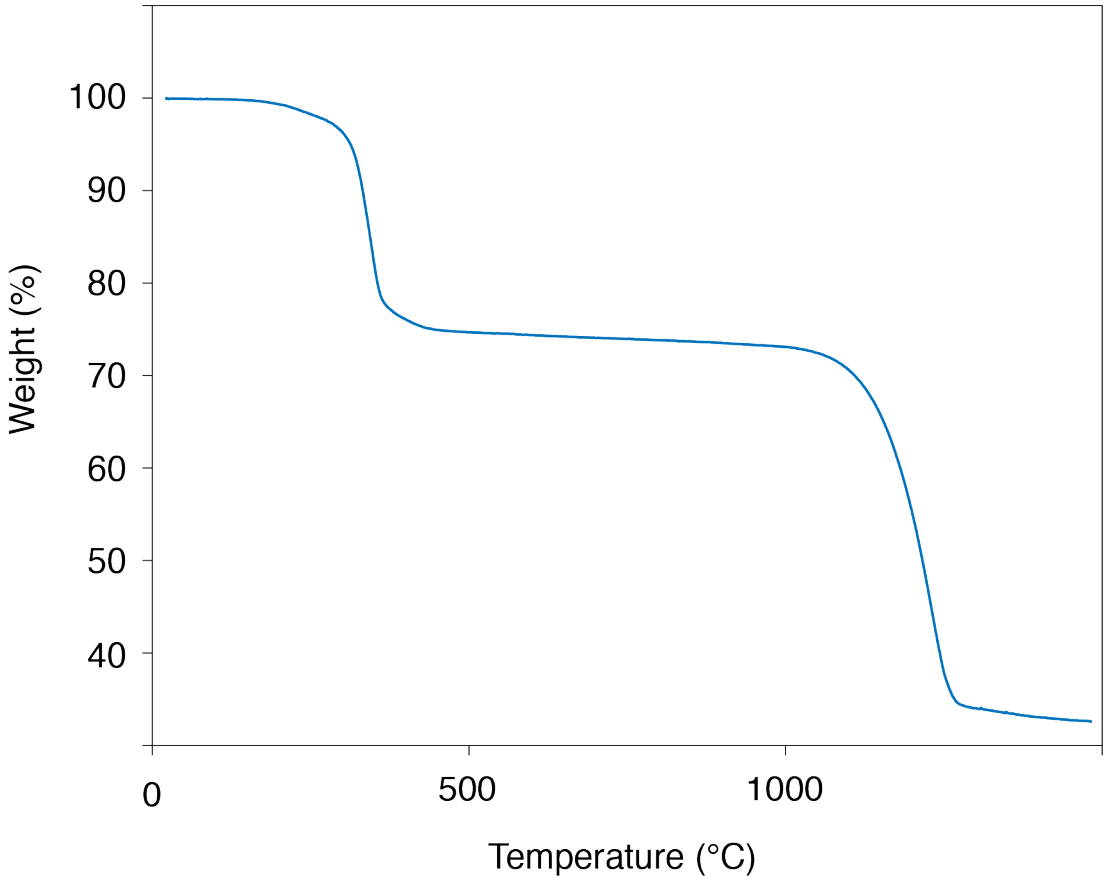

Figure B 2: Thermogravimetric analysis of $MoSe_2$/PLL/F77 systems. The TGA curves shows degradation at 300 °C.

Antibacterial activity of $MoSe_2$/PLL.F77 against model systems

Figure B 3 shows, the antibacterial activity of $MoSe_2$/PL/F77 determined against two model systems, gram-negative *E. coli* K12 MG1655 and gram-positive *S. aureus*. The $MoSe_2$/PL/F77 eliminated both strains of bacteria at 50 µg/ml.

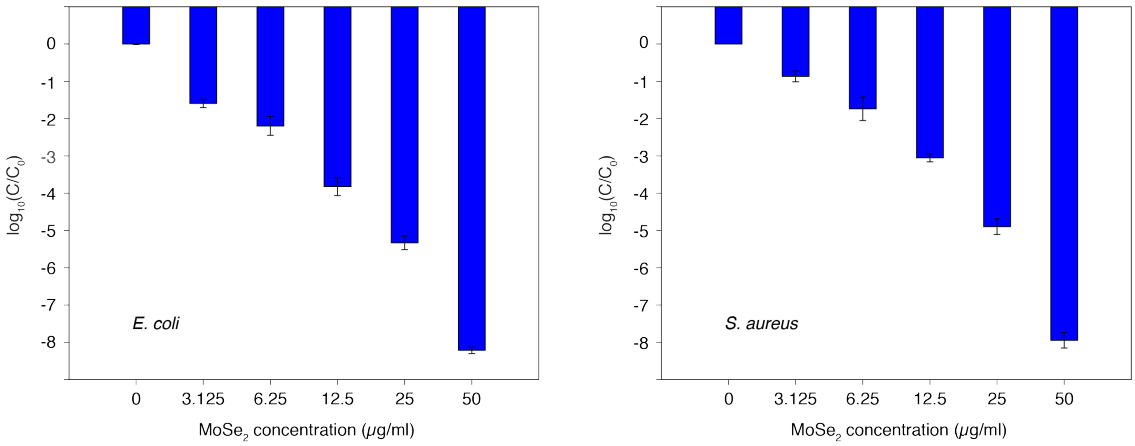

Figure B 3: The antibacterial activity of $MoSe_2$/PL/F77 determined against two model systems, gram-negative *E. coli* and gram-positive *S. aureus*.

AFM characterization of $MoSe_2$/PL/F77

Figure B 4 shows, the thickness of $MoSe_2$/PL/F77 system, characterized using AFM. The thickness of the flake was ~ 8 nm.

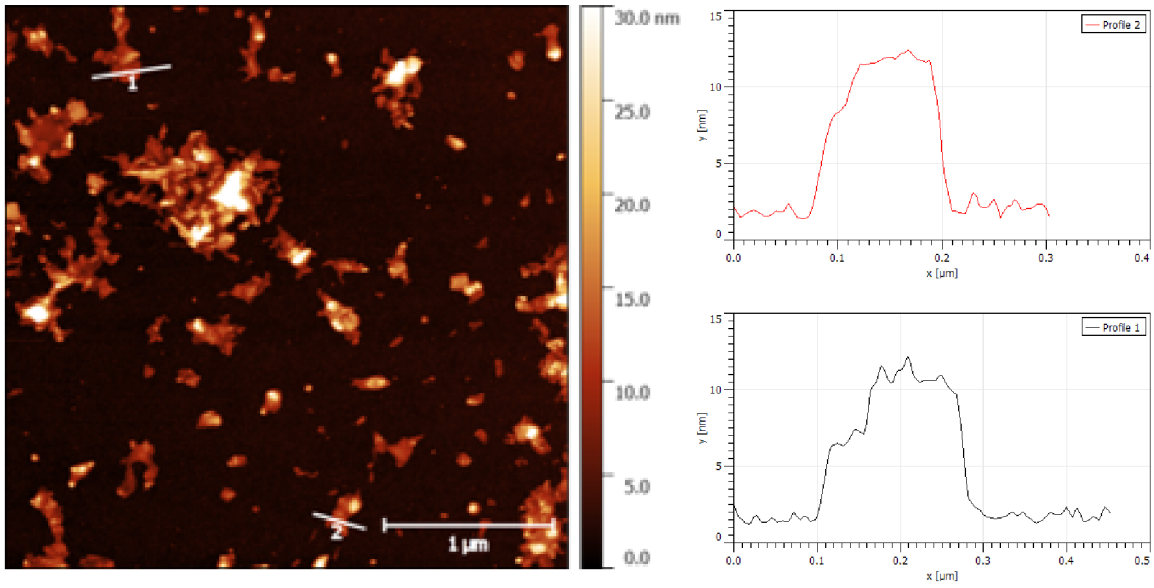

Figure B 4: The AFM image of $MoSe_2$ /PLL/F77, which shows thickness around 8 nm.

SEM image of PLL resistant *S. aureus*

Figure B 5 shows the change in morphology of *S. aureus* after 10 passages with PLL. The SEM images shows formations of flagellar like structure on the surface of *S. aureus* membranes, which inhibit the interactions with PLL.

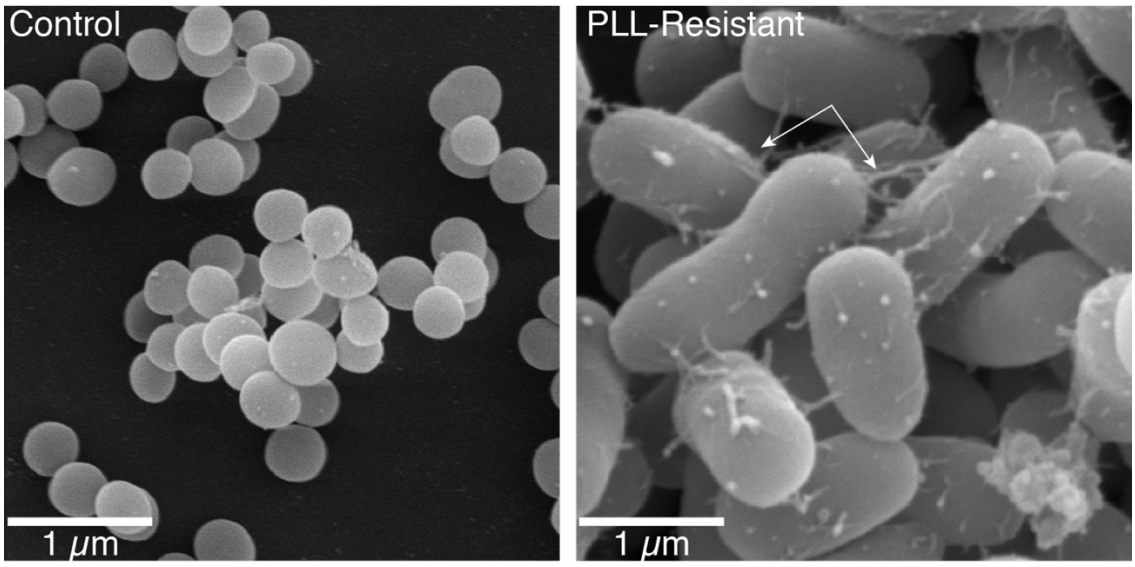

Figure B 5: SEM images of *S. aureus* before treatment and after 10 passages of treatment with PLL.

TEM imaging of TSB medium before and after treatments with PLL

Figure B 6 shows, the secretion of small vesicles in the medium, which provide resistance to *S. aureus* from PLL.

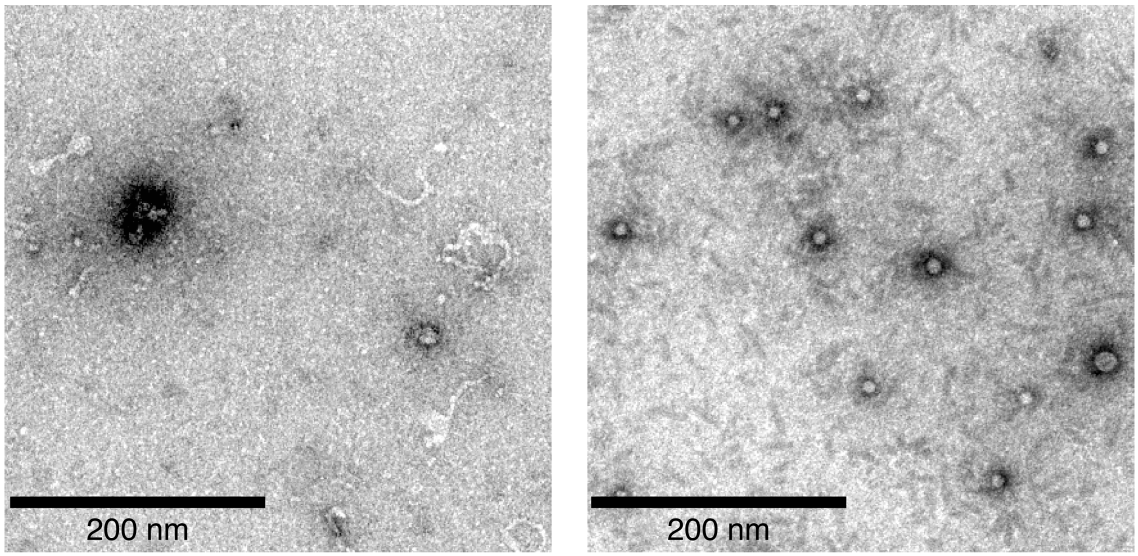

Figure B 6: TEM image of bacteria cultured medium for *S. aureus* showing the secretion of small vesicle like structure in medium, as a part of resistance mechanism of PLL-resistant bacteria.